

**Imaging of the atria and cardiac conduction
system – from experiment to computer
modelling**

A thesis submitted to the University of Manchester for the degree of
Doctor of Philosophy
in the Faculty of Medical and Human Sciences

2012

Guoliang Hao

School of Medicine

Content

Content	1
Figures	4
Tables	7
Abbreviations	8
Abstract	11
Declaration	12
Copyright statement	13
Acknowledgments	15
Chapter 1 General introduction	16
1.1 Cardiac conduction system (CCS)	16
1.1.1 Definition of CCS	16
1.1.2 Sinoatrial node (SAN)	16
1.1.3 Atrioventricular node (AVN)	17
1.1.4 His-Purkinje system	17
1.1.5 Less well-known components of the CCS - Atrioventricular ring tissues (AV rings)	18
1.2 Experimental mapping of the electrical activation in the heart... ..	20
1.2.1 About mapping	20
1.2.2 Optical mapping	20
1.2.3 Multi-electrode mapping	25
1.3 Computer simulation of the electrical activation of the heart	26
1.4 Aims of thesis	27
Chapter 2 General methods	29
2.1 Electrophysiological tools	29
2.1.1 Langendorff heart perfusion system	29
2.1.2 Tissue bath system	32
2.2 Masson's trichrome staining	32
2.3 Immunohistochemistry	33
2.3.1 The principle of immunohistochemistry	33
2.3.2 Solutions and chemicals used	34
2.3.3 Immunolabelling protocol for tissue sections	34
2.3.4 Confocal laser scanning microscopy	38
2.4 Animals	40
Chapter 3 Detailed three-dimensional anatomical model of the rabbit heart	41
3.1 Introduction	41
3.1.1 About anatomical model of rabbit heart	41
3.1.2 Former work – a detailed 3D anatomical model of the rabbit right atrium	41
3.1.3 Aim	42
3.2 Materials and methods	46
3.2.1 Animals	46

3.2.2	High-resolution magnetic resonance imaging (MRI)	46
3.2.3	Image processing platform - MATLAB.....	46
3.2.4	Semi-automatic segmentation in MATLAB	47
3.2.5	Smoothing of the 3D model.....	48
3.2.6	3D reconstruction of coronary vessels of the rabbit heart	48
3.3	Results	53
3.4	Discussion	64
Chapter 4	Multi-electrode mapping system	65
4.1	Introduction	65
4.1.1	The multi-electrode mapping system needed in this study.....	65
4.1.2	The hardware in the optical mapping system could be adapted	65
4.1.3	Aim	70
4.2	Materials and methods.....	71
4.2.1	Construction of the connector extensions for the data acquisition cards	71
4.2.2	Construction of the multi-electrode arrays	71
4.2.3	Software development environment - LabVIEW	72
4.3	Results	73
4.3.1	Connector extensions for the data acquisition cards.....	73
4.3.2	Multi-electrode arrays.....	73
4.3.3	Recording software.....	76
4.3.4	Analysis software.....	84
4.4	Discussion	87
Chapter 5	Experimental mapping and computer simulation of the electrical activation sequence of the rabbit atria	90
5.1	Introduction	90
5.1.1	Interatrial conduction routes	90
5.1.2	About experimental mapping in the rabbit atria	91
5.1.3	About computer simulation of the whole rabbit atria.....	92
5.1.4	Aims.....	95
5.2	Materials and methods.....	95
5.2.1	Animals and preparations	95
5.2.2	Optical mapping.....	96
5.2.3	Multi-electrode mapping	97
5.2.4	Anatomical model employed in the computer simulation.....	98
5.2.5	Cellular automaton model.....	98
5.3	Results	99
5.3.1	Optical mapping.....	99
5.3.2	Multi-electrode mapping	102
5.3.3	Computer simulation	114
5.4	Discussion	117
5.4.1	About the mapping techniques employed in this chapter.....	117
5.4.2	About the electrical activation sequence of rabbit atria.....	120
5.4.3	About the computer simulation of rabbit atria.....	122
Chapter 6	Anatomical and functional investigation of the cardiac conduction system and arrhythmogenic atrioventricular ring tissues in the rat heart.....	126
6.1	Introduction	126

6.1.1	About atrioventricular ring tissues (AV rings).....	126
6.1.2	Aims.....	127
6.2	Materials and methods.....	127
6.2.1	Animals.....	127
6.2.2	MR imaging.....	127
6.2.3	Histological and immunohistochemical staining for 3D reconstruction.....	128
6.2.4	3D reconstruction procedure.....	129
6.2.5	Preparations for electrophysiological study.....	130
6.2.6	Multi-electrode mapping experiments on the AV rings.....	132
6.2.7	Data analysis.....	135
6.3	Results.....	135
6.3.1	3D reconstruction.....	135
6.3.2	Electrophysiological study.....	137
6.4	Discussion.....	144
6.4.1	3D anatomical model of the AV rings.....	144
6.4.2	Spontaneous activity in the AV rings.....	151
Chapter 7	General summary and future directions.....	152
7.1	About 3D anatomical models.....	152
7.1.1	Summary of the 3D anatomical models.....	152
7.1.2	Future directions for the reconstruction of 3D anatomical models.....	153
7.2	About multi-electrode mapping system.....	154
7.2.1	Summary of the multi-electrode mapping system.....	154
7.2.2	Future directions for the improvement of the multi-electrode mapping system.....	154
7.3	About experimental mapping and computer simulation of the electrical activation of the rabbit atria.....	156
7.3.1	Summary of the experimental mapping and computer simulation of the electrical activation of the rabbit atria.....	156
7.3.2	Future directions for the experimental mapping and computer simulation of the electrical activation of the rabbit atria.....	157
7.4	About electrophysiological study on AV rings.....	158
7.4.1	Summary of electrophysiological study on AV rings.....	158
7.4.2	Future directions for the electrophysiological study on AV rings.....	158
References	160
Publications	167
Appendix I: Three dimensional anatomical model of the human atrioventricular node	169
Appendix II: Functional, anatomical and molecular investigation of the cardiac conduction system and arrhythmogenic atrioventricular ring tissues in the rat heart	177
Appendix III: Mitogen-activated protein kinase kinase 4 deficiency in cardiomyocytes causes connexin 43 reduction and couples hypertrophic signals to ventricular arrhythmogenesis	178

Word count: 40,532

Figures

Figure 1.1 Schematic drawing of the 256 channel photodiode array optical mapping system used in this study	22
Figure 2.1 Langendorff heart perfusion system and tissue bath perfusion system used in this study	30
Figure 3.1 3D visualisations of the anatomical model of the rabbit right atrium – former work carried out by Dr. Jue Li	44
Figure 3.2 Principle of removing noise in a 2D image with median filtering..	49
Figure 3.3 An example of segmentation and removal of noise	51
Figure 3.4 Flow diagram for smoothing the 3D model	52
Figure 3.5 Flow diagram for reconstruction of the coronary veins	54
Figure 3.6 2D images from the ‘MRI array’ and the ‘model array’ in MATLAB	55
Figure 3.7 3D visualisation of the anatomical model of the rabbit heart with whole atria and part of the ventricles	58
Figure 3.8 A front view of the 3D anatomical model of the rabbit atria	60
Figure 3.9 A dorsal view of the 3D anatomical model of the rabbit atria	62
Figure 4.1 Overview of the data acquisition card system in the optical mapping system	67
Figure 4.2 Pinout of the data acquisition card (NI PXI-6031E).....	68
Figure 4.3 Diagram of the pinout of the connector extensions for the data acquisition card.....	74
Figure 4.4 Diagram of the smaller size 64 channel electrode array	77
Figure 4.5 Diagram of the larger 64 channel electrode array	78
Figure 4.6 Initialisation interface of the recording software	79
Figure 4.7 Experiment interface of the recording software.....	82

Figure 4.8 Analysis software of the multi-electrode mapping system	85
Figure 4.9 An example of a mapping experiment carried out on rabbit Bachmann's bundle	88
Figure 5.1 Epicardial activation maps of the Langendorff-perfused rabbit heart mapped with an optical mapping system	93
Figure 5.2 Setting of the cellular automaton model of action potential conduction	100
Figure 5.3 An example of a result obtained using the 256-channel optical mapping system.....	103
Figure 5.4 Mapping result obtained using the twelve bipolar electrodes (preparation I).....	106
Figure 5.5 Mapping result obtained using the twelve bipolar electrodes (preparation II)	108
Figure 5.6 Representative epicardial activation map (dorsal view) of the Langendorff-perfused rabbit atria mapped with multi-electrode mapping system.....	110
Figure 5.7 Representative epicardial activation map (top view) of the Langendorff-perfused rabbit atria mapped with multi-electrode mapping system.....	112
Figure 5.8 Isotropic computer simulation result obtained using the 3D rabbit atria model (together with the cellular automaton model of action potential conduction).....	115
Figure 5.9 Anisotropic computer simulation result obtained using the 3D rabbit atria model (together with the cellular automaton model of action potential conduction).....	118
Figure 5.10 Comparison of the computer simulation results and the experimental mapping results.....	123
Figure 6.1 Flow diagram showing 3D reconstruction procedure	133
Figure 6.2 Complete transparent views of the 3D rat heart model with the CCS and the AV rings	138
Figure 6.3 Two views of the CCS and the AV rings with myocardium removed.	140

Figure 6.4 Two views showing the relationship between the atrioventricular conduction axis and the AV rings	142
Figure 6.5 Pacemaker activities in right AV ring tissue	145
Figure 6.6 Pacemaker activities in left AV ring tissue.....	147
Figure AI.1 An exempling showing delineation of the inferior nodal extension on one histological section	172
Figure AI.2 3D visualisations of the anatomical model of the human AVN	175

Tables

Table 2.1: Summary of primary antibodies used.....	35
Table 2.2: Summary of secondary antibodies used	36
Table 2.3 Summary of excitation and emission spectra for the common fluorochromes	38
Table 3.1 Components of the 3D anatomical model of the rabbit right atrium	43
Table 3.2 Components of the 3D anatomical model of the rabbit heart.....	57

Abbreviations

2D	two-dimensional
3D	three-dimensional
AF	atrial fibrillation
AO	aorta
AS	atrial septum
AV	atrioventricular
AVN	atrioventricular node
AV ring	atrioventricular ring tissue
BB	Bachmann's bundle
BDM	2,3-butanedione monoxime
BSA	bovine serum albumin
BZ	block zone
Cav3	caveolin-3
CMOS	complementary metal-oxide semiconductor
CCD	charge-coupled device
CCS	cardiac conduction system
CS	coronary sinus
CT	computed tomography
CT	crista terminalis

Cx40	connexin40
Cx43	connexin43
DIFF	differential
GUI	graphical user interface
I_f	hyperpolarization-activated funny current
ISO	isoproterenol
IVC	inferior vena cava
LAA	left atrial appendage
LED	light emitting diode
LR	left ring tissue
LSPV	left superior pulmonary vein
LSVC	left superior vena cava
MB	main branch
MEA	multi-electrode array
MRI	magnetic resonance imaging
MV	mitral valve
PA	pulmonary artery
PCB	printed circuit board
PBS	phosphate buffered saline
PDA	photodiode array
Pfs	Purkinje fibres
PV	pulmonary vein
RAA	right atrial appendage

RAN	retroaortic node
RB	roof bundle
RBB	right His bundle branch
RR	right ring tissue
RSE	single-ended ground referenced
RSPV	right superior pulmonary vein
RSVC	right superior vena cava
RV	right ventricle
SAN	sinoatrial node
SEM	standard error of mean
SVC	superior vena cava
Tbx3	T-box transcription factor
TV	tricuspid valve

Abstract

Imaging of the atria and cardiac conduction system – from experiment to computer modelling

The University of Manchester

Guoliang Hao

Submission for the degree of Doctor of Philosophy

December 2012

Background: Experimental mapping and computer modelling provide important platforms to study the fundamental mechanisms underlying normal and abnormal activation of the heart. However, accurate computer modelling requires detailed anatomical models and needs support and validation from experimental data. **Aims:** 1) Construction of detailed anatomical heart models with the cardiac conduction system (CCS). 2) Mapping of the electrical activation sequence in rabbit atria to support and validate computer simulation. 3) Mapping of the spontaneous activity in the atrioventricular ring tissues (AV rings), which consist of nodal-like myocytes and can be a source of atrial tachycardia. **Methods:** High-resolution magnetic resonance imaging (MRI) and computed tomography (CT) were used to provide two-dimensional (2D) images for the construction of the detailed anatomical heart models. Immunohistochemistry and Masson's trichrome staining were used to distinguish the CCS in the heart. LabVIEW was used in the development of a multi-electrode mapping system. The multi-electrode mapping technique was employed to map the electrical activation sequence of the rabbit atria. The cellular automaton model was used to simulate electrical activation of the rabbit atria. **Results:** 1) Three detailed anatomical models were constructed, including a detailed three dimensional (3D) anatomical model of the rabbit heart (whole of the atria and part of the ventricles), a 3D anatomical model of the rat heart with the CCS and AV rings, and a 3D anatomical model of the human atrioventricular node. 2) A multi-electrode mapping system was developed. 3) The electrical activation sequence of the rabbit atria was mapped in detail using the multi-electrode mapping system. The conduction velocity in the rabbit atria was measured. The mapping data showed the coronary sinus and the left superior vena cava do not provide an interatrial conduction route during sinus rhythm in the rabbit heart. 4) Electrical activation of the rabbit atria was simulated with the support of the 3D anatomical model of the rabbit atria and the experimental mapping data. 5) The spontaneous activity in the rat AV rings was mapped using the multi-electrode mapping system. **Conclusions:** The detailed anatomical models developed in this study can be used to support accurate computer simulation and can also be used in anatomical teaching and research. The experimental mapping data from the rabbit atria can be used to support and validate computer simulation. The computer simulation study demonstrated the importance of anatomical structure and electrophysiological heterogeneity. This study also demonstrated that the AV rings could potentially act as ectopic pacemakers.

Declaration

No portion of the work referred to in the thesis has been submitted in support of an application for another degree or qualification of this or any other university or institute of learning.

Copyright statement

The author of this thesis (including any appendices and/or schedules to this thesis) owns certain copyright or related rights in it (the “Copyright”) and s/he has given The University of Manchester certain rights to use such Copyright, including for administrative purposes.

Copies of this thesis, either in full or in extracts and whether in hard or electronic copy, may be made only in accordance with the Copyright, Designs and Patents Act 1988 (as amended) and regulations issued under it or, where appropriate, in accordance with licensing agreements which the University has from time to time. This page must form part of any such copies made.

The ownership of certain Copyright, patents, designs, trade marks and other intellectual property (the “Intellectual Property”) and any reproductions of copyright works in the thesis, for example graphs and tables (“Reproductions”), which may be described in this thesis, may not be owned by the author and may be owned by third parties. Such Intellectual Property and Reproductions cannot and must not be made available for use without the prior written permission of the owner(s) of the relevant Intellectual Property and/or Reproductions.

Further information on the conditions under which disclosure, publication and commercialization of this thesis, the Copyright and any Intellectual Property

and/or Reproductions described in it may take place is available in the University IP Policy (see <http://documents.manchester.ac.uk/DocuInfo.aspx?DocID=487>), in any relevant Thesis restriction declarations deposited in the University Library, The University Library's regulations (see <http://www.manchester.ac.uk/library/aboutus/regulations>) and in The University's policy on Presentation of Theses.

Acknowledgments

First and foremost I want to thank my supervisors, Professor Mark Boyett and Dr. Halina Dobryzinski who has supported me throughout my Ph.D study with their patience, understanding and expertise advice whilst allowing me the room to work in my own way.

I also would like to take this opportunity to thank my advisor Dr. Ming Lei for his help and advice throughout my PhD study. I am most grateful to Dr. Jue Li for showing me how to do the 3D reconstruction in MATLAB and for her encouragement and understanding during my study.

I gratefully acknowledge all of my colleagues. In particular Dr. Xue Cai, Dr. Joseph Yanni, Dr. Oliver Monfredi, Dr. Olga Fedorenko and Mr Andrew Atkinson for their suggestions and assistances during my histological and electrophysiological work. I also would like to thank my Chinese friends in our lab, Yatong, Yifen, Junhong, Yuanlong, Jianyun, Jiawei, Wendy, Terry and Vicky for making my time in Manchester an enjoyable experience. I sincerely thank the School of Biomedicine and the Overseas Research Students Awards Scheme for founding my studies.

Finally, I take this opportunity to express my gratitude to family for their support and understanding.

Chapter 1 General introduction

1.1 Cardiac conduction system (CCS)

1.1.1 Definition of CCS

The cardiac conduction system (CCS) is a specialised tissue and consists of the sinoatrial node (SAN), the atrioventricular node (AVN), and the His-Purkinje system. The CCS is responsible for the initiation and propagation of the action potential leading to a coordinated heart beat (Anderson et al., 2009).

1.1.2 Sinoatrial node (SAN)

The SAN is the pacemaker tissue located in the right atrium of the heart, near the entrance of the superior vena cava. The cells in the SAN are modified cardiac myocytes. They are responsible for generating sinus rhythm, but they do not contract strongly. The SAN was first described in 1907 by Arthur Keith and Martin Flack, but the understanding of its location and anatomy has been modified in the last decade (Boyett, 2009; Boyett and Dobrzynski, 2007). Based on histology and immunolabelling of marker proteins, detailed three-dimensional (3D) anatomical models of rabbit SAN and human SAN have been developed (Chandler et al., 2011; Dobrzynski et al., 2005). These models show the SAN is an extensive structure which extends from the superior vena cava towards the inferior vena cava.

Most cells in the CCS depolarize spontaneously, which enables these cells to function as cardiac pacemakers, but the SAN cells have a faster rate than that of other cardiac pacemakers, so the SAN is the dominant pacemaker (Boyett and Dobrzynski, 2007).

1.1.3 Atrioventricular node (AVN)

The impulse generated by SAN travels rapidly throughout the cells of the atria causing them to contract and then it activates the AVN.

The AVN, discovered by Sunao Tawara in 1906 (Akiyama, 2010), is normally the only electrical connection between the atria and the ventricles. It delays the electrical impulse before conducting it to stimulate the ventricles. This slight delay not only provides adequate time for the filling of the ventricles for optimal cardiac output, but also can protect the ventricles from atrial fibrillation by limiting the number of action potentials conducted to the ventricles. The AVN also performs as a backup pacemaker in patients with SAN dysfunction (De Mello, 1977).

1.1.4 His-Purkinje system

The action potential travels from the AVN to the right and left ventricles through a specialised conduction system which is called the His-Purkinje system. The His-Purkinje system consists of the His bundle and Purkinje fibres. The Purkinje fibres were discovered by Jan Purkinje in 1839 and the His bundle was discovered by Wilhelm His in 1893. The His-Purkinje system

provides a relatively high-speed pathway for the action potential to propagate to the whole ventricles and then cause the ventricular muscle to contract and forcefully eject the blood contained within.

1.1.5 Less well-known components of the CCS - Atrioventricular ring tissues (AV rings)

Further areas of histologically specialised tissue distinct from the CCS within the muscular atrioventricular (AV) junction have been shown to exist, initially by Kent (1893), who speculated that they provided multiple pathways crossing the AV junction. It was subsequently established, however, that the AVN provides the only pathway for conduction across the AV junctions in structurally normal hearts, and that the nodes identified by Kent were part of the so-called atrioventricular ring tissues (AV rings) (Lewis, 1920).

The AV rings consist of nodal-like myocytes which surround mitral (MV) and tricuspid (TV) valves at the insertions with the atrial myocardium and unite in the retroaortic node (RAN) (Anderson and Taylor, 1972). The AV rings are also anatomically continuous with the CCS (Yanni et al., 2009), although they are not thought to contribute to the normal functioning of the heart. Their location suggests that they could be a source of atrial tachycardia (Kistler et al., 2006).

For most of the preceding 100 years, the components of the CCS have been identified on the basis of the histological criteria established by Aschoff (1910) and Monckeberg (1910). However, with advancing techniques it is now possible to identify transcription factors involved in the development of the

CCS which can be used to identify the conduction tissues. Tbx3 has been shown to repress cardiac chamber specific genes therefore allowing the conducting system phenotype to be expressed (Christoffels et al., 2010; Hoogaars et al., 2007). Work by Hoogaars showed Tbx3 expression in the entire CCS (Hoogaars et al., 2004) and also in components of the extended conduction system including the AV rings identified by Anderson (Anderson, 1972). Most recently Aanhaanen et al. have demonstrated that the AV rings are formed from the embryonic atrioventricular canal musculature, which also contributes to the compact AVN, nodal extension and retroaortic node (RAN) (Aanhaanen et al., 2010). The linking developmentally of the AV rings with the atrioventricular conduction pathway has increased the desire to study the extent of the rings and how they interact with conduction pathway. The anatomy of the AV ring system has been extensively studied using immunohistochemical techniques in many species including human (Anderson and Taylor, 1972), mouse, rat, guinea-pig and rabbit (Yanni et al., 2009), and a similar morphology was found in them all. The fact that the AV rings share common development origins with the AVN suggests that they may have similar gene expression profiles and possess some subsidiary pacemaker functionality. HCN4, the principal ion channel that underlies the funny current (I_f), an important pacemaker current in the SAN and AVN, has been demonstrated to be expressed in the AV rings (Yanni et al., 2009). The AV rings also have high Cx45 and low Cx43 expression (Yamamoto et al., 2006) further supporting the fact that they are specialised conduction tissues compared to the working myocardium. Electrophysiological investigations have shown nodal-type action

potentials in the vestibule of the tricuspid valve in pig and dog hearts (McGuire et al., 1996; McGuire et al., 1994).

1.2 Experimental mapping of the electrical activation in the heart

1.2.1 About mapping

Experimental mapping techniques have been widely used to study the electrophysiological properties in intact animals, isolated whole hearts and different cardiac tissues (Durrer et al., 1970; Fedorov et al., 2007; Kumagai et al., 2000; Schuessler et al., 1993). From the mapping results, we can study electrophysiological properties such as the conduction velocity of the action potential, pacemaker location and activation pattern in cardiac tissues. Mapping techniques provide an important platform to study cardiac electrophysiology.

Experimental mapping techniques can be classified into optical mapping and multi-electrode mapping techniques. Different mapping techniques have different advantages and limitations.

1.2.2 Optical mapping

Optical mapping is a novel technique which can be used to map the electrical activation in the cardiac tissues using voltage-sensitive dyes. The fluorescence characteristics of the voltage-sensitive dyes in the myocardium are related to the transmembrane action potentials of the myocytes (Efimov et al., 2004).

Lasers or broadband light are typically used to illuminate the voltage-sensitive dyes and the fluoresced light is acquired with different imaging devices such as charge-coupled device (CCD) cameras or photodiode arrays (PDA). Figure 1.1 shows a typical optical mapping system which uses a PDA as the optical signal detector. This system consists of a light emitting diode (LED) array system, a camera, a 256-channel PDA, a 256-channel current-to-voltage converter and amplifier system, a 256-channel data acquisition system and a computer. The camera and the PDA have the same focus, so the visible light camera can be used to monitor if the tissue is on the focus of the mapping system or not. The excitation light provided by the LED arrays focuses on the cardiac tissue. The PDA transfers the intensity changes of the fluorescence light emitted from the voltage-sensitive dye into electrical signals, and then outputs from the PDA are fed into the 256-channel current-to-voltage converter. The signals recorded by the 256-channel data recording system are fed to the computer. The wavelength of the excitation light is chosen dependent on the excitation spectrum of the voltage-sensitive dye loaded in the cardiac tissue. The excitation light can be focussed on the perfused tissue from above or below the tissue. However, if the tissue is too thick for the excitation light to penetrate, the excitation light must be set above the tissue.

Some other optical mapping systems replace the PDA and the multi-channel data recording systems with CCD cameras to detect the light signals. Because a CCD sensor has a large number of pixels, optical mapping systems with a CCD have an important advantage of higher spatial resolution. However, data acquisition sampling rates of CCD mapping systems are generally lower than

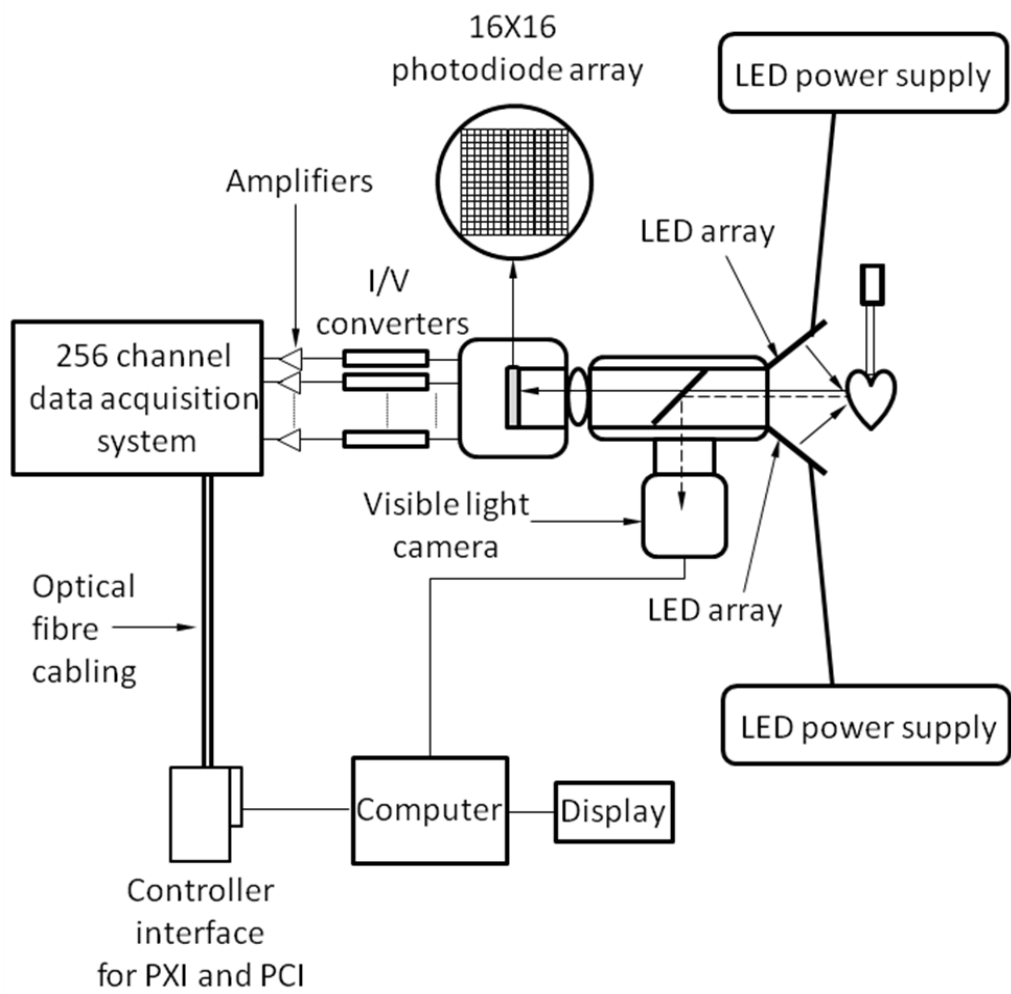


Figure 1.1 Schematic drawing of the 256 channel photodiode array optical mapping system used in this study

The excitation light provided by the LED arrays focuses on the heart. The 16 x 16 PDA transfers the intensity changes of the fluorescence light emitted from the voltage-sensitive dye into electrical signals. Outputs from the PDA are fed into a 256-channel current-to-voltage converter (I/V converter). Then the signals recorded by the 256-channel data acquisition system are fed to the computer. A visible light camera is also used to monitor if the cardiac tissue is in focus. The dashed line with arrow shows the route of the visible light.

of PDA systems.

Complementary metal-oxide semiconductor (CMOS) cameras are a newly used tool in optical mapping systems. With the development of CMOS camera technology, CMOS cameras can provide high-speed image acquisition. During a test on a Langendorff-perfused guinea-pig heart, a CMOS camera from SciMedia reached 10000 frames per second (10 kHz) at a high spatial resolution of 100 by 100 pixels (Malkin et al., 2005). Owing to this obvious advantage, CMOS cameras in optical mapping systems are becoming more competitive.

In addition to mapping the electrical propagation in cardiac tissues, optical mapping signals can provide the repolarisation information about the cardiac tissues. This is a significant advantage of the optical mapping technique, especially in studying arrhythmias. In addition, optical mapping systems can also be used to measure the concentration of intracellular Ca^{2+} with various kinds of Ca^{2+} sensitive dyes (Entcheva and Bien, 2006; Lan et al., 2007; Morad et al., 1986).

In optical mapping, the contraction of the cardiac muscle is the main source of artefacts because it may lead to changes of optical density, light scattering and reflection. At present, there are four main methods to deal with this problem. The first method is to mechanically reduce the contractile movement by pressing the tissue against a glass plate with proper pressure or stretching the tissue with appropriate force (Fedorov et al., 2007; Kanai and Salama, 1995; Komuro et al., 1986; Sakai et al., 1997). The second method is to use low- Ca^{+}

solution to perfuse the tissue or the whole heart to reduce the contraction (Komuro et al., 1986). The third way is to make use of an excitation-contraction uncoupler such as blebbistatin or 2,3-butanedione monoxime (BDM) etc., which are chemicals that suppress muscle contraction without obvious change in membrane excitability (Fedorov et al., 2007; Li et al., 1985; Lou et al., 2011). However, the mechanism of action of excitation-contraction uncouplers is not so clear and the action potential is slightly affected (Sellin and McArdle, 1994). The fourth method is to use a single or a bundle of optical fibres to obtain the optical signals from the surface of the preparation directly (Ausma et al., 2000; Mejia-Alvarez et al., 2003; Witkowski et al., 1994).

1.2.3 Multi-electrode mapping

A multi-electrode mapping system consists of several electrodes or multi-electrode arrays, which contain many electrodes, and a multi-channel data acquisition system. The electrodes or multi-electrode arrays directly touch the cardiac tissue and record extracellular potentials from different sites simultaneously. Then the signals are fed to a multi-channel data acquisition system and activation sequence maps can be drawn based on the data.

This technique has been used for at least 70 years. As early as 1941, Harris mapped the electrical activation sequence of the ventricular epicardium of different species using several silver electrodes (Harris, 1941).

Multi-electrode mapping systems can not only map the tissue in a

two-dimensional plane, but also can map the tissue in a 3D plane (eg. the whole heart). As early as in 1970, Durrer and his co-workers studied the propagation of excitation in human heart using a multi-electrode mapping system (Durrer et al., 1970). The array they used contained 870 electrodes and the 3D electrical activity was recorded by a tape recorder and played back at a slower speed by the ECG writer. This system can give a time resolution better than 1 ms.

During the last several decades, this technique has been developed with the improvement in electronic components and computer technology. Current highly capable electrical mapping systems have more than 1000 channels of simultaneous data acquisition with sampling rates ranging from 1000 to 8000 samples per second (Smith, 2003).

1.3 Computer simulation of the electrical activation of the heart

Optical mapping and multi-electrode mapping techniques have yielded a wealth of knowledge about the electrical activation of the heart. However, both of them have their own complications and limitations. In addition to these experimental mapping techniques, computer simulation provides an important platform to study the electrical activation in the heart (Abed et al., 2010). However, accurate computer simulation requires detailed anatomical models and needs support and validation from experimental data (Boyett et al., 2005).

Based on different techniques, several anatomical models of the whole heart, atria (Abed et al., 2010; Blanc et al., 2001; Seemann et al., 2006), ventricles

(Bishop et al., 2010) and some components of the CCS (Chandler et al., 2011; Dobrzynski et al., 2005; Li et al., 2008) have been developed and used in computer simulation. However, detailed 3D anatomical models of the heart including the CCS are still lacking.

1.4 Aims of thesis

As described in section 1.3, accurate computer simulation requires detailed anatomical models and needs support and validation from experimental data.

The first aim of this study was to reconstruct detailed anatomical models including a detailed 3D anatomical model of the rabbit heart (whole atria and part of ventricles), a 3D anatomical model of the rat heart with the CCS and AV rings, and a 3D anatomical model of the human FAVN. These anatomical models can be used in computer simulation and anatomical teaching.

The second aim of this study was to develop a multi-electrode mapping system.

The third aim of this study was to map the electrical activation sequence in the Langendorff-perfused rabbit atria. This data can be used to support and validate computer simulation.

The fourth aim of this study was to use the cellular automaton model to simulate the electrical activity of the rabbit atria based on the detailed anatomical model and the experimental data above.

As described in section 1.1.5, the AV rings consist of nodal-like myocytes and can be a source of atrial tachycardia. The fifth aim was to investigate the

electrical activation of the AV rings using experimental mapping techniques.

Chapter 2 General methods

2.1 Electrophysiological tools

2.1.1 Langendorff heart perfusion system

The first Langendorff heart perfusion system was established in 1895 by Oscar Langendorff (Langendorff, 1895). This technique has been widely used for the study of heart physiology for more than 100 years. With this technique, we can study heart physiology without hormonal or neuronal influences seen in the living animals.

Although the Langendorff perfusion technique was modified in many ways in the last century, its general principle is still the same today. Perfusate was continuously delivered into the heart through a cannula inserted in the aorta. The increased pressure in the ascending aorta shuts the leaflets of the aortic valve. Therefore, the perfusate is forced to flow through the coronary arteries, the capillary system and then the coronary veins, and finally, the perfusate flows back to the right atrium via the coronary sinus. The flow rate of the perfusate differs depending on species and ranges from 7~9 ml/min for adult rat to 20 ml/min for adult rabbit (Doring, 1990).

As shown in Figure 2.1, if connector C is connected with connector C1 (cannula), the system could be used as a Langendorff heart perfusion system.

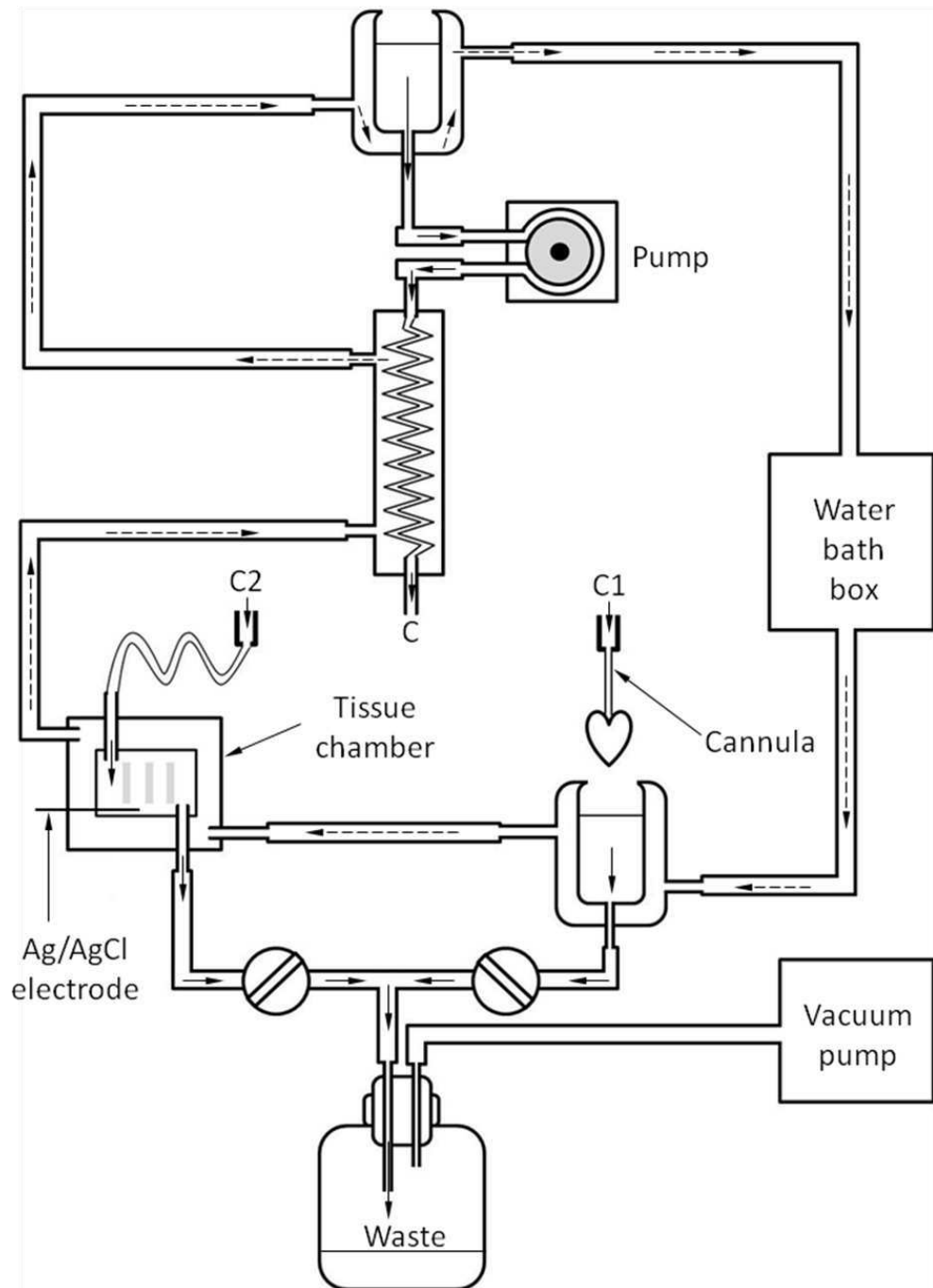


Figure 2.1 Langendorff heart perfusion system and tissue bath perfusion system used in this study

Flow direction of the water in the heating circuit is indicated by the dashed arrows. The temperature of the water was set at 37 °C and could be adjusted. Warmed perfusate was pumped to connector C by a peristaltic pump (Gilson Minipuls 3, Anachem). If connector C was connected to connector C1, the perfusate was pumped to the cannula, so the system could be used as a Langendorff heart perfusion system; if connector C was connected to connector C2, the perfusate was pumped to the tissue chamber, so the system could be used as a tissue bath perfusion system. Waste perfusate was collected in a bottle connected to a vacuum pump.

In the study of this thesis, the flow rate of the perfusate was set at 9 ml/min for rat and 20 ml/min for rabbit; the temperature of the perfusate was controlled to 37°C.

2.1.2 Tissue bath system

As shown in Figure 2.1, if connector C is connected with connector C2, the perfusate is pumped to the tissue bath (length, 3 cm; width, 3 cm; depth, 1.5 cm). A silver (Ag)/silver-chloride (AgCl) electrode was fixed on the bottom of the tissue chamber which was used as an indifferent electrode in the electrophysiological experiments.

In the study of this thesis, the flow rate of the perfusate in the tissue bath chamber was set as 20 ml/min; the temperature of the perfusate was controlled to 37°C and monitored using a glass-encapsulated miniature thermistor (RS Components).

2.2 Masson's trichrome staining

Tissue sections were cut and mounted on Superfrost Plus glass slides (BDH) and then stored at -80°C. Frozen sections were fixed at room temperature in Bouin's fluid at least overnight (in fume cupboard), and then washed in 70 % ethanol three times (each wash 10 min). Then the sections were immersed in Celestine Blue for 5 min and rinsed thoroughly in distilled water until no blue stain was visible in the slide container. Further staining was performed using Cole's alum haematoxylin for 10 min and then the sections were washed thoroughly in tap water for 30 min. The sections were checked for nuclear

staining by low power light microscopy. If too light, the sections were re-stained in celestine blue-alum haematoxylin; if too dark, the section were washed in tap water and checked again. Then sections were stained in acid fuchsin for 4 min, and rinsed in distilled water for 20~30 min. Then sections were stained with phosphomolybdic acid for 5 min, and then drained and stained in methyl blue for 5 min. Finally, the slides were rinsed thoroughly in distilled water for 20~30 min and treated with 1 % acetic acid for 2 min.

After staining, sections were dehydrated through graded ethanols (70 % ethanol 1 min, 90 % ethanol 1 min, 100 % ethanol 4 min), cleared in HistoClear (National Diagnostics) for 10 min and mounted in DPX mounting medium (BDH) for permanent mounting.

With the Masson's trichrome technique, nuclei are stained dark blue, myocytes are stained purple and connective tissue is stained blue. The stained sections were kept at room temperature for subsequent viewing with a Leica Materials Workstation (Leica Microsystems, Wetzlar, Germany) or a Zeiss Axio Imager.Z1 microscope fitted with an AxioCam HRc camera and Axiovision software (Carl Zeiss, Germany).

2.3 Immunohistochemistry

2.3.1 The principle of immunohistochemistry

The principle of immunohistochemistry is to detect the location of proteins of interest in tissue sections. The primary antibodies react with the protein's epitopes. Then specific secondary antibodies were used to detect the primary

antibodies. The secondary antibodies are conjugated to fluorochromes, which can emit light at a specific wave length on excitation by a specific wave length light. Therefore, the secondary antibodies can be visualised by microscopy.

2.3.2 Solutions and chemicals used

2.3.2.1 Solutions

0.01 M phosphate buffer solution (PBS, pH 7.4, Sigma) was used to bathe the tissue and 0.1 % Triton-X100 (Sigma) was used to permeabilise the tissue.

2.3.2.2 Fixatives

10 % neutral buffered formalin (pH 7.4, Sigma) was used to fix the tissue.

2.3.2.3 Primary antibodies used

The primary antibodies used are summarised in Table 2.1.

2.3.2.4 Secondary antibodies used

The secondary antibodies used are summarised in Table 2.2.

2.3.3 Immunolabelling protocol for tissue sections

2.3.3.1 Fixation

The tissue sections were fixed by immersing the tissue sections in 10 % buffered formalin for 30 min in a fume cupboard. The function of formalin is to preserve cellular components such as proteins by reacting primarily with basic

amino acids to form cross-linking ‘methyl bridges’.

To remove excess fixative, tissue sections were washed with 0.01 M PBS three times (10 min each time).

2.3.3.2 Permeabilisation of the cell membrane

The tissue sections were treated with 0.1% Triton X-100 in PBS for 30 min at room temperature to permeabilise the cell membrane. This allows the antibodies and other reagents to penetrate the cell membrane and reach the epitopes located on the cytoplasmic side of the cell membrane.

2.3.3.3 Blocking of non-specific sites

After treatment with Triton X-100, tissue sections were washed in PBS three times (10 min each time). To block non-specific sites, the tissue sections were incubated with 1% bovine serum albumin (BSA, Sigma).

2.3.3.4 Labelling with primary antibodies

Primary antibodies were diluted in 1% BSA in PBS. Table 2.1 summarises the dilution of antibodies used in this study. Tissue sections were incubated with the primary antibodies in a humid box at -4 °C overnight.

2.3.3.5 Labelling with secondary antibodies

Secondary antibodies were diluted in 1% BSA in PBS. Table 2.2 summarises the dilution of antibodies used in this study. After application of primary antibodies, sections were washed with PBS three times (10 min each time).

Table 2.1: Summary of primary antibodies used

Primary antibody	Host	Supplier	Dilution	Incubation period
Cx40	Goat	Santa Cruz Biotechnology	1:50	overnight
Cx43	Rabbit	Millipore	1:50	overnight
Caveolin-3	Mouse	BD Biosciences	1:100	overnight
HCN4	Rabbit	Alomone Labs	1:20	overnight
Cx43	Mouse	Millipore	1:50	overnight

Table 2.2: Summary of secondary antibodies used

Secondary antibody	Host	Supplier	Dilution	Incubation period
Anti-rabbit FITC conjugated	Donkey	Millipore	1:100	1 hour
Anti-mouse Cy3 conjugated	Rabbit	Chemicon	1:100	1 hour
Anti-goat FITC conjugated	Donkey	Millipore	1:100	1 hour
Anti-mouse Cy3 conjugated	Donkey	Millipore	1:100	1 hour

Tissue sections were then incubated with secondary antibodies for 1 hour in a dark humid box at room temperature.

2.3.3.6 Mounting of tissue sections

After application of secondary antibodies, tissue sections were washed with PBS three times (10 min each time). Then the tissue sections were mounted with the anti-fade reagent, Vectashield (H-1000, Vector Laboratories) and covered with coverslips. Then the edges of the coverslips were sealed with nail varnish to prevent drying of tissue.

2.3.3.7 Control experiments

Two types of control experiments were used in this study. In the first control experiment, the primary antibodies were omitted. This experiment was used to confirm the secondary antibodies do not cross-react between species. In the second control experiment, the secondary antibodies were omitted but the primary antibodies were still applied, and this experiment was used to confirm that labelling obtained was not the result of non-specific binding of the primary antibodies.

2.3.4 Confocal laser scanning microscopy

The immunolabelled tissue sections were scanned using confocal laser scanning microscopy (LSM 5 Pascal, Carl Zeiss, NY, USA). The excitation wavelength was chosen according to the type of fluorochrome conjugated to the secondary antibodies. Table 2.3 summarises the excitation and emission

Table 2.3 Summary of excitation and emission spectra for the common fluorochromes

Fluorochromes	Excitation wavelength (nm)	Emission wavelength (nm)	Laser
FITC	496	518	Argon
Cy3	556	574	Krypton
Alexa	488	518	Argon

wave lengths used in the confocal scanning of the tissue sections.

2.4 Animals

All the animals used in this study were sacrificed according to the United Kingdom Animals (Scientific Procedures) Act, 1986.

Chapter 3 Detailed three-dimensional anatomical model of the rabbit heart

3.1 Introduction

3.1.1 About anatomical model of rabbit heart

As described in Section 1.3, computer simulation provides an important platform to study the electrical activation of the heart and accurate computer simulation requires detailed anatomical models. There are several previous anatomical models of the rabbit ventricles based on different techniques (Bishop et al., 2010; Bordas et al., 2011). However, there is no detailed anatomical model of rabbit atria available for computer simulation.

3.1.2 Former work – a detailed 3D anatomical model of the rabbit right atrium

Based on MRI data combined with the analysis of histological and immunolabelled serial sections, a 3D anatomical model of the rabbit right atrium had been constructed by my colleague, Dr. Jue Li (University of Manchester) in 2005 (Li, 2005). To construct the 3D anatomical model of the rabbit right atrium, 1540 two-dimensional (2D) MRI images of the rabbit heart were imported into the workspace of MATLAB (version 7; The Math Works,

Inc., Matick, MA, USA) to produce a 3D mathematical array. The elements in the 3D array were anisotropic with a voxel size of $26.4 \mu\text{m} \times 26.4 \mu\text{m} \times 24.4 \mu\text{m}$. The anisotropic 3D array was then converted to an isotropic 3D array ($30 \mu\text{m} \times 30 \mu\text{m} \times 30 \mu\text{m}$) using cubic interpolation. Then the left atrium, left ventricle and part of the right ventricle were 'cut' off from the 3D array. Hence, the 3D array only consisted of the information of the right atrium and part of the right ventricle. The 3D array was named as 'right atrium MRI array' and saved in MATLAB. Then a new 3D array with the same size was built in the workspace of MATLAB. This new 3D array was named 'right atrium model array', and was used to save the model data. In the 'right atrium model array', different objects (such as sino-atrial node, atrioventricular node etc.) were segmented (i.e., identified and classified as different objects) from the 'right atrium MRI array'. Different objects were indexed with different integrated numbers in the 'right atrium model array'.

The anatomical model of the rabbit right atrium consists of 17 different objects. Table 3.1 lists the names of the objects and the indexed numbers in the 'right atrium model array'. Figure 3.1 shows 3D visualisations of the anatomical model of the rabbit right atrium.

3.1.3 Aim

Accurate computer simulation requires detailed anatomical models. The main aim of this chapter was to continue the work on the anatomical model of the rabbit right atrium to construct a detailed 3D anatomical model of the rabbit

Table 3.1: Components of the 3D anatomical model of the rabbit right atrium

Index	Object name	Index	Object name
1	Connective tissue	10	Central fibrous body
2	Aorta	11	Sinoatrial node
3	Coronary sinus	12	Crista terminalis
4	Right atrium	13	Roof bundle
5	Tricuspid valve	14	Main branch
6	Foramen ovale	15	Inferior node extension
7	Superior vena cava	16	Block zone
8	Inferior vena cava	17	Ventricular tissue
9	Atrioventricular node		

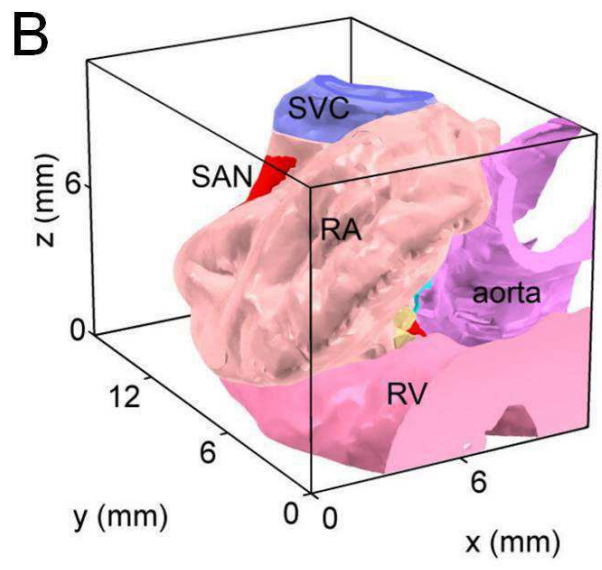
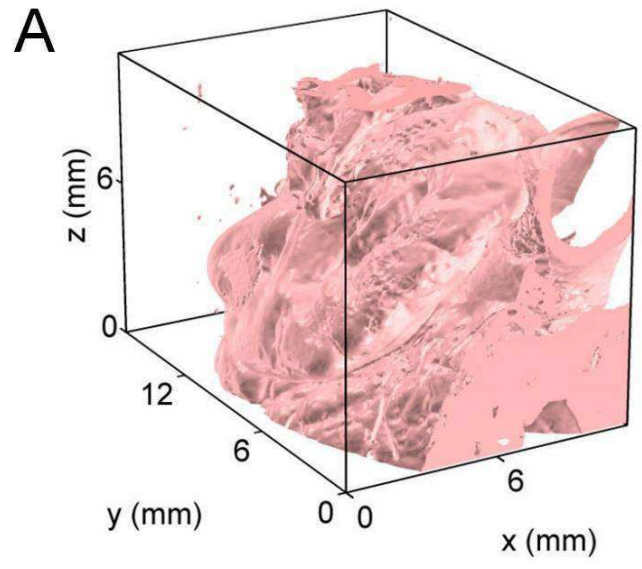


Figure 3.1 3D visualisations of the anatomical model of the rabbit right atrium – former work carried out by Dr. Jue Li

A, 3D visualisation of the anatomical model before segmentation. B, 3D visualisation of the model after segmentation. Different objects are shown with different colours. RA, right atrium; RV, right ventricle; SAN, sinoatrial node; SVC, superior vena cava. Adapted and modified from Li et al. (2005).

heart with intact atria and part of the ventricles. The work was to be carried out based on the 1540 high resolution MRI images.

3.2 Materials and methods

3.2.1 Animals

New Zealand White rabbits (male; 1.5 to 2 kg; provided by University of Manchester) were used in this study.

3.2.2 High-resolution magnetic resonance imaging (MRI)

A 2.5 kg New Zealand White rabbit (provided by University of Manchester, UK) was sacrificed. After the heart was excised, extraneous tissue and the bottom of ventricles was carefully removed from the heart. Then the preparation was fixed in 10% neutral buffered formalin. High-resolution MRI was performed at 4°C using an 11.7 Tesla, vertical bore (89-mm) Bruker AMX500 micro-imaging system (Bruker Medical, Ettlingen, Germany). 1540 images of the rabbit heart including both atria and part of ventricles were obtained. The voxel size of the MRI data after reconstruction was $26.4 \mu\text{m} \times 26.4 \mu\text{m} \times 24.4 \mu\text{m}$.

3.2.3 Image processing platform - MATLAB

MATLAB (matrix laboratory) is a numerical computing environment and high-level programming language developed by MathWorks, Inc., USA. It is widely

used in academic and research institutions as well as industrial enterprises. For the study in this thesis, several software applications developed in MATLAB were employed to view and analyse the MRI images and the micro-CT images. All the 3D reconstruction and visualisation work were carried out using the software applications developed in MATLAB.

3.2.4 Semi-automatic segmentation in MATLAB

The procedure of the construction of the 3D anatomical model used in this chapter was similar to that used in the former work (Li, 2005). 1540 2D MRI images of the rabbit heart were imported into the workspace of MATLAB (version 7; The Math Works, Inc., Natick, MA, USA) to generate a 3D mathematical array. The 3D array was named 'MRI array' and saved in MATLAB. Then a new 3D array with same size was built in the workspace of MATLAB. This new 3D array was named 'model array', and was used to save the model data. In order to use the former work described in Section 3.1.3, after the construction of the 3D mathematic arrays in MATLAB, the 3D arrays of the right rabbit atrium including the 'right atrium MRI array' and the 'right atrium model array' were import into 'MRI array' and 'model array' separately. Then the remaining part of the 'MRI array' was semi-automatically segmented using two graphical user interface (GUI) applications. The two GUI applications were developed in MATLAB by Dr. Jue Li (University of Manchester) and improved by the author. One GUI application was used to observe the 3D arrays in three directions (along the x, y and z axes) to choose the best direction to carry out segmentation. Another GUI application was used to

semi-automatically segment different objects (such as Bachmann's bundle, pulmonary veins etc.) from the 'MRI array' and then save in the 'model array'.

3.2.5 Smoothing of the 3D model

Boundaries of some objects could not be clearly distinguished in the MRI images. As shown in Figure 3.3.A, for example, the boundary of the root of aorta was not very clear. In this situation, some noise would be generated in the 3D model in the process of semi-automatic segmentation. Figure 3.3.B shows an example of the noise. It was necessary to remove the noise in the 3D model. The median filtering technique, a simple and effective way to remove this kind of noise (impulse noise and speckle noise), was used after the segmentation. The principle of removing the noise in a 2D image with median filtering is shown in Figure 3.2. Figure 3.3 shows an example of how the noise was removed in a 2D image using median filtering and Figure 3.4 shows the flow diagram of the programme developed in MATLAB to remove the noise in the 3D model.

3.2.6 3D reconstruction of coronary vessels of the rabbit heart

The coronary vessels in the MRI images had clear boundaries and, therefore, it was feasible to automatically segment them. A programme was developed in

Figure 3.2 Principle of removing noise in a 2D image with median filtering

A, '1' in the array stands for information. Impulse noise and speckle noise are shown in the ellipses and circle, respectively. B, array A after median filtering to remove the vertical impulse noise. The template in the filtering method was designed as [1,3], which means that each element in the array will be replaced by the median value among the three elements in the horizontal direction (two horizontal neighbouring elements and itself). In this way, the speckle noise shown in the circle and the impulse noise in the vertical direction shown in the blue ellipses were removed. C, array B after median filtering to remove the horizontal impulse noise. The template in this filtering was designed as [3,1], which means that each element in the array will be replaced by the median value among the three elements in the vertical direction (two vertical neighbouring elements and itself). In this way, the impulse noise in the horizontal direction shown in green ellipses was removed.

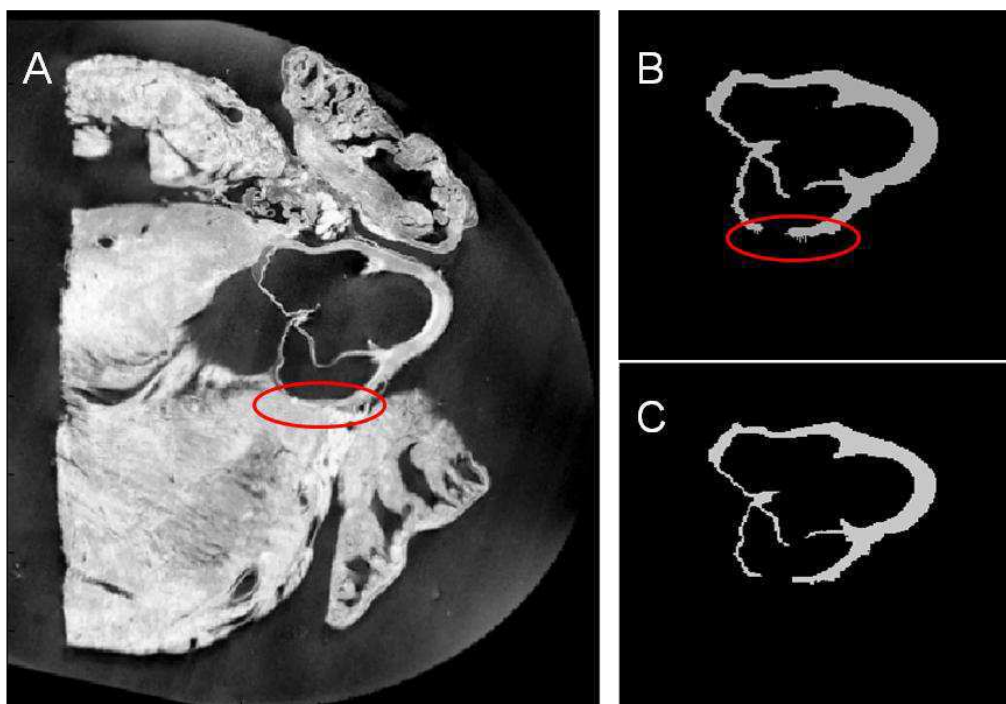


Figure 3.3 An example of segmentation and removal of noise

A, an example of a 2D MRI image. B, object 'aorta' after segmentation in the 2D image. The noise which was generated during the segmentation is shown in the ellipse. C, object 'aorta' after smoothing by median filtering. Impulse noise and speckle noise was removed.

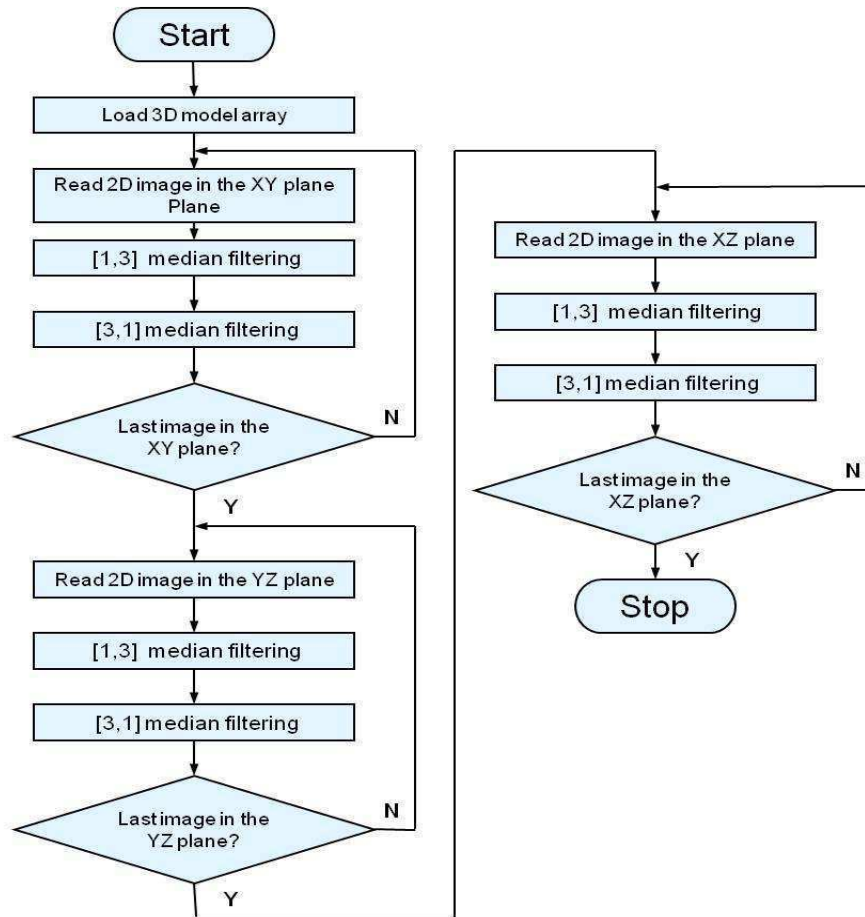


Figure 3.4 Flow diagram for smoothing the 3D model

All the 2D images in the XY, YZ, XZ planes in the 3D model array were subject to median filtering to remove impulse noise and speckle noise. In each 2D image, [1,3] and [3,1] templates were used in the median filter to remove impulse noise in horizontal and vertical directions. The programme was coded and run in MATLAB.

MATLAB for the 3D reconstruction of the coronary vessels based on the MRI data. Figure 3.5 shows the flow diagram of the programme used to automatically reconstruct the coronary vessels.

3.3 Results

Based on the former work (the 3D anatomical model of the rabbit right atrium) 1540 2D MRI images of the rabbit heart were segmented. Figure 3.6 shows one example of a 2D images. Figure 3.6A shows one original MRI image, which was saved in the ‘MRI array’ in MATLAB. Figure 3.6B shows the corresponding images after segmentation, which was saved in the ‘model array’ in MATLAB. Because the different objects of the rabbit heart were indexed with different numbers in the ‘model array’, the objects can be displayed with different colours. Therefore, different objects can also be given different electrophysiological properties in computer simulations. The former work (the 3D anatomical model of the rabbit right atrium) included 17 different objects. Four objects in the former work, including the aorta, atrium and ventricle, were extended in this study. Another 13 objects were segmented in this study. The names of the objects and their indexed numbers in the ‘model array’ are listed in Table 3.2. Figure 3.7 shows 3D visualisations of the anatomical model with the whole atria and part of ventricles before and after segmentation. High resolution 3D visualisations of the model without the ventricles are shown in Figures 3.8 and 3.9.

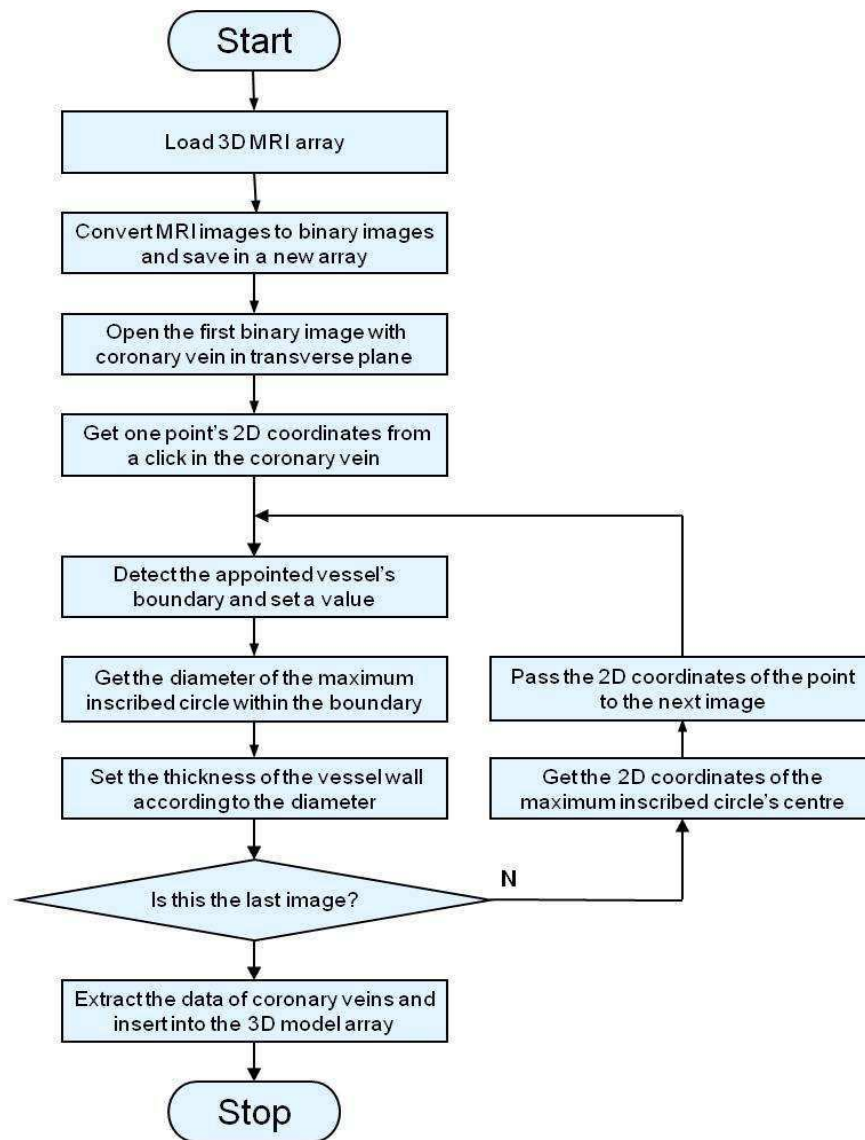


Figure 3.5 Flow diagram for reconstruction of the coronary veins

The programme was coded and run in MATLAB.

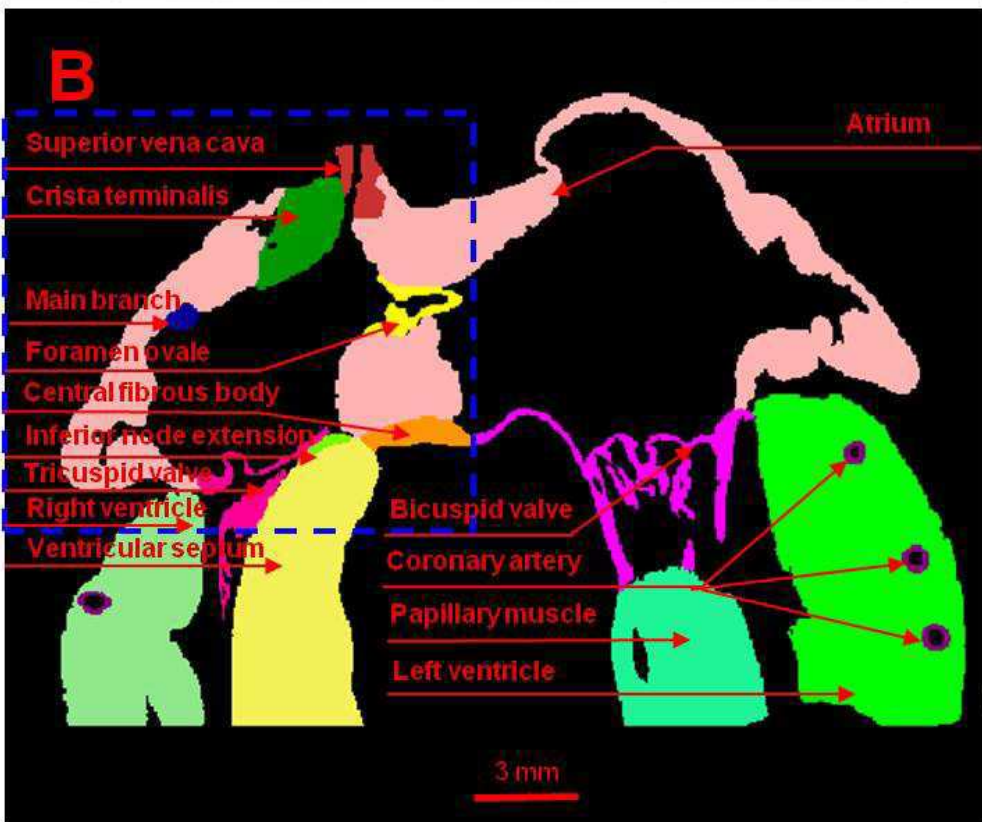
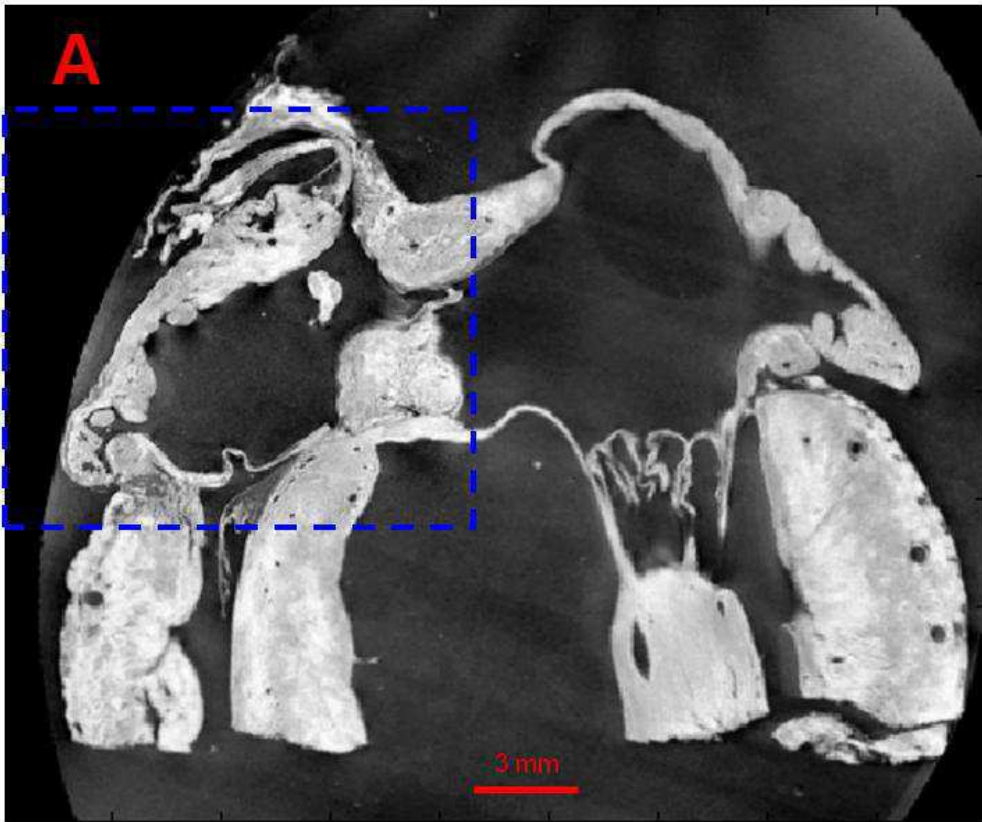


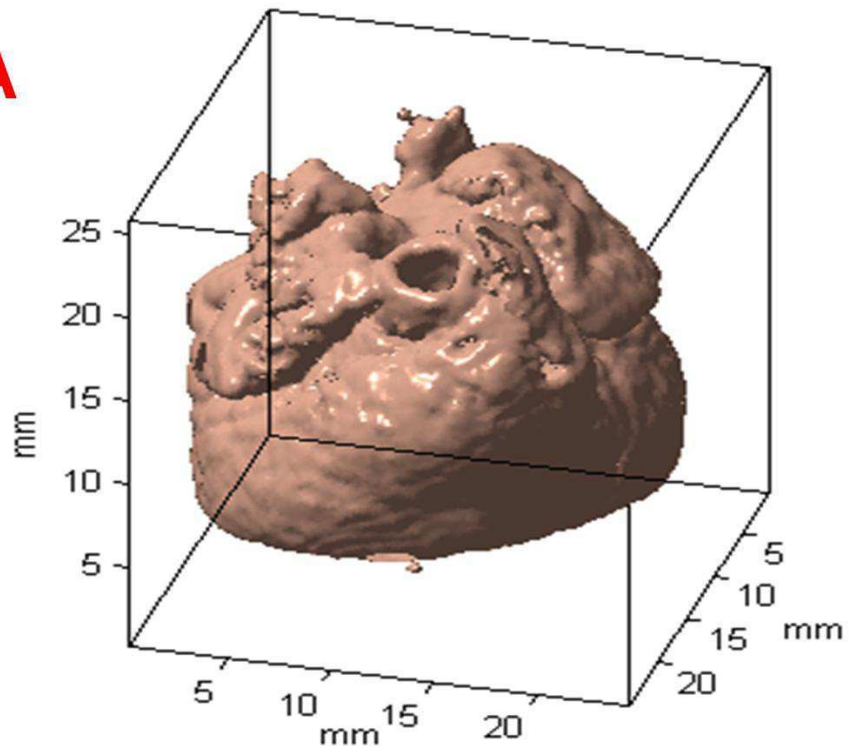
Figure 3.6 2D images from the ‘MRI array’ and the ‘model array’ in MATLAB

A, one MRI image before segmentation saved in the ‘MRI array’. B, corresponding image after segmentation saved in the ‘model array’. Different objects are displayed with different colours. The blue dashed square shows the region of the former work.

Table 3.2: Components of the 3D anatomical model of the rabbit heart

Index	Object name	Index	Object name
1	Connective tissue	16	Block zone
2	Aorta	17	Bachmann's bundle
3	Coronary sinus	18	Pulmonary artery
4	Atrium	19	Bicuspid valve
5	Tricuspid valve	20	Coronary artery
6	Foramen ovale	21	Coronary vein
7	Superior vena cava	22	Left ventricular tissue
8	Inferior vena cava	23	Right ventricular tissue
9	Atrioventricular node	24	Ventricular septum tissue
10	Central fibrous body	25	Papillary muscle
11	Sinoatrial node	26	Left superior pulmonary vein
12	Crista terminalis	27	Right superior pulmonary vein
13	Roof bundle	28	Left inferior pulmonary vein
14	Main branch	29	Right inferior pulmonary vein
15	Inferior node extension	30	Left superior vena cava

A



B

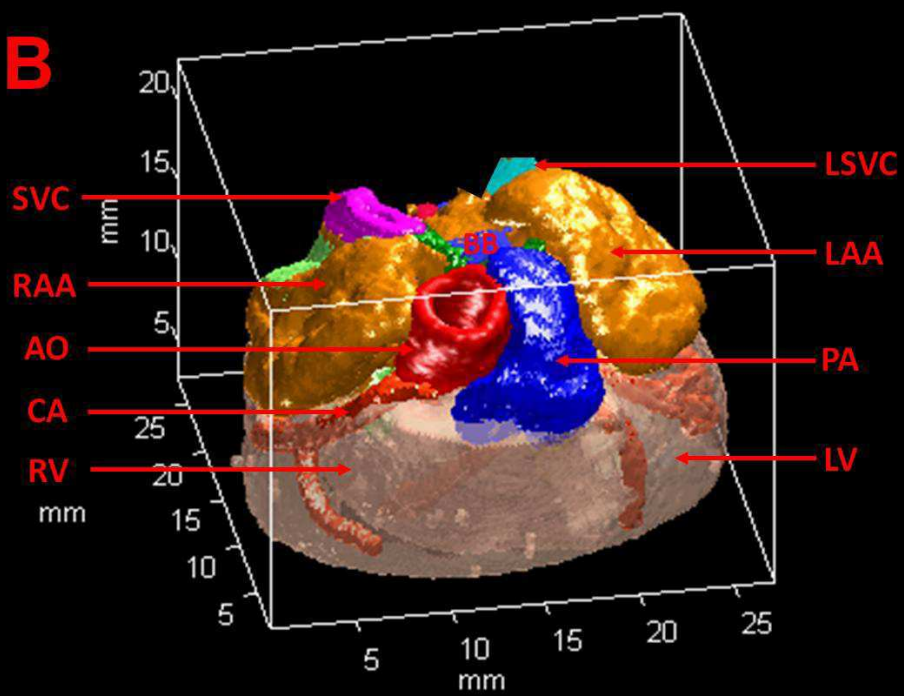


Figure 3.7 3D visualisation of the anatomical model of the rabbit heart with whole atria and part of the ventricles

A, 3D visualisation of the anatomical model before segmentation. B, 3D visualisation of the model after segmentation. Different objects are shown with different colours. AO, aorta; BB, Bachmann's bundle; LAA, left atrial appendage; LSVC, left superior vena cava; MB, main branch; PA, pulmonary artery; RAA, right atrial appendage; RB, roof bundle; SVC, superior vena cava.

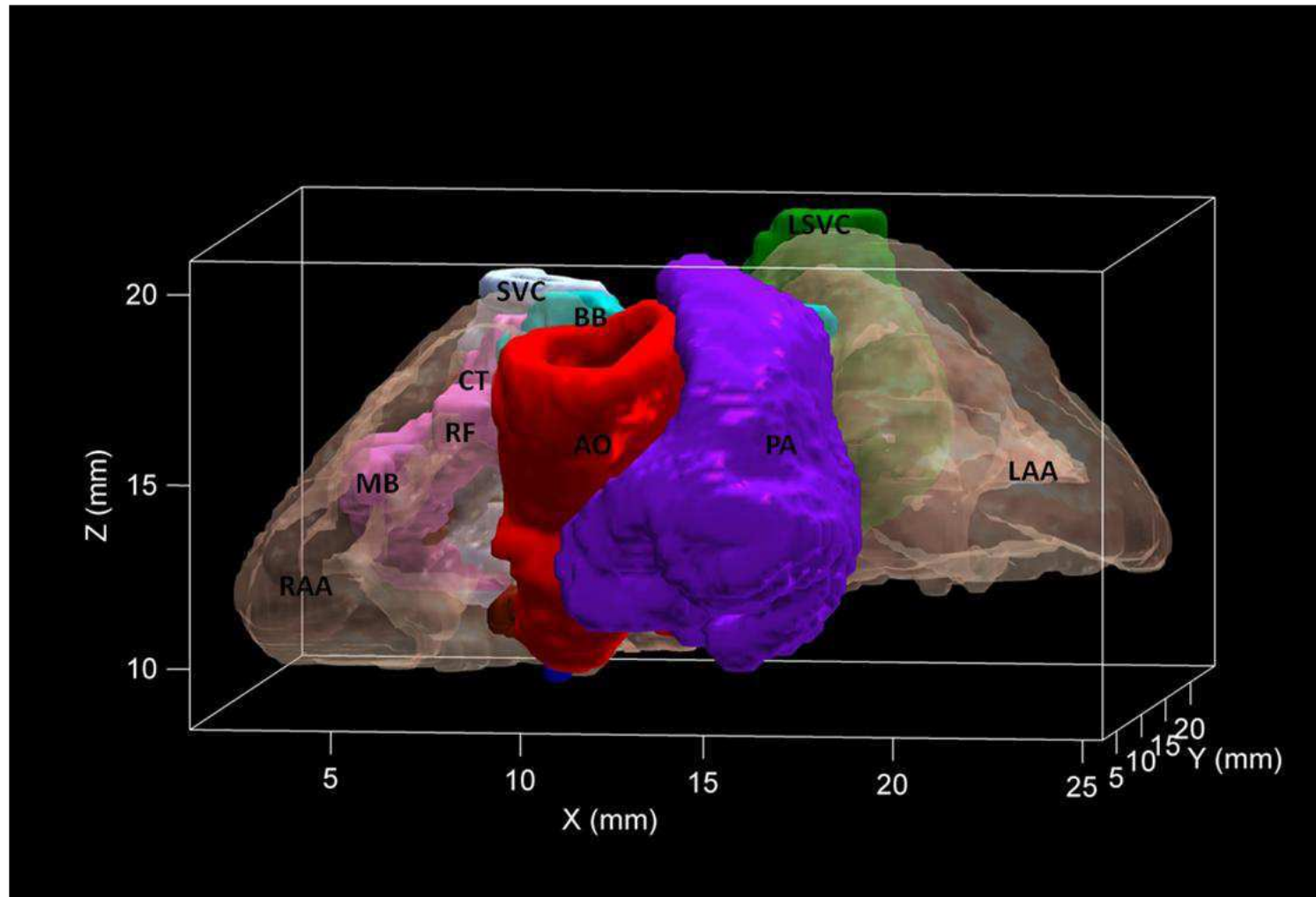


Figure 3.8 A front view of the 3D anatomical model of the rabbit atria

Different objects are displayed by different colours and are labelled. AO, aorta; BB, Bachmann's bundle; CT, crista terminalis; LAA, left atrial appendage; LSVC, left superior vena cava; MB, main branch; PA, pulmonary artery; RAA, right atrial appendage; RB, roof bundle; RSVC, right superior vena cava.

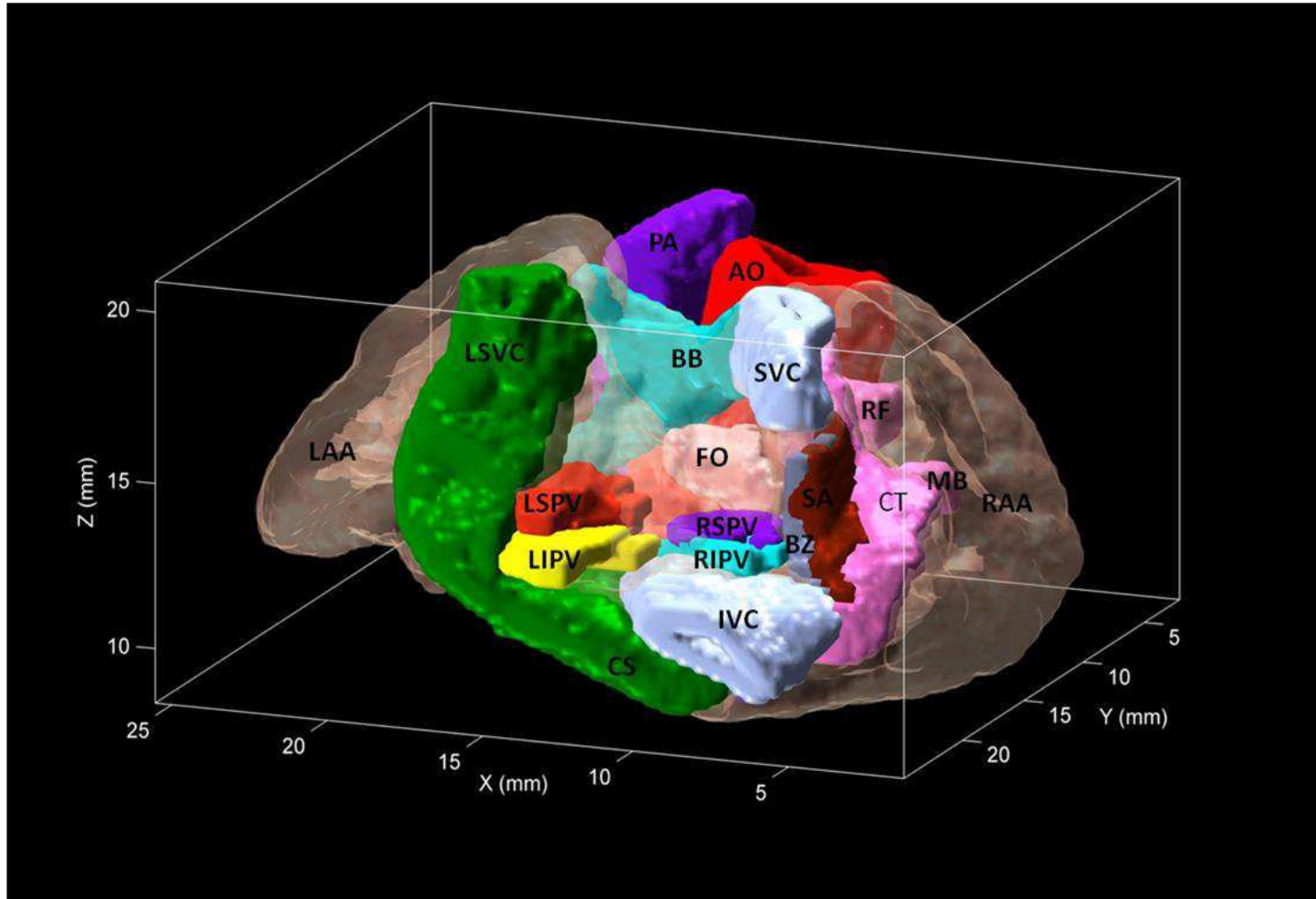


Figure 3.9 A dorsal view of the 3D anatomical model of the rabbit atria

Different objects are displayed by different colours and are labelled. AO, aorta; BB, Bachmann's bundle; CS, coronary sinus; CT, crista terminalis; IVC, inferior vena cava; LAA, left atrial appendage; LIPV, left inferior pulmonary vein; LSPV, left superior pulmonary vein; LSVC, left superior vena cava; MB, main branch; PA, pulmonary artery; RAA, right atrial appendage; RB, roof bundle; RSPV, right superior pulmonary vein; RSVC, right superior vena cava; SA, sinus node.

3.4 Discussion

Based on the former work (the 3D model of the rabbit right atrium) a 3D anatomical model of the rabbit heart with whole atria and parts of the ventricles were constructed in this study. This 3D anatomical model included not only the SAN and AVN, which are parts of the CCS, but also the major muscle bundles of the atria, such as the crista terminalis, Bachmann's bundle and the roof bundle. Therefore, this model made it is possible to construct an electrophysiological detailed and anatomically accurate 3D computer model of the rabbit atria which could be used to simulate the propagation of electrical activity. The 3D anatomical model of the atria will be used in Chapter 5 to simulate the electrical activation sequence of the rabbit atria during sinus rhythm with the cellular automaton model. In the future, this anatomical model will also be used to simulate the electrical activation of the rabbit atria under normal and abnormal conditions with detailed action potential models.

Chapter 4 Multi-electrode mapping system

4.1 Introduction

4.1.1 The multi-electrode mapping system needed in this study

Mapping the electrical activation sequence of the rabbit atria was one of the aims in this study. A 256 channel optical mapping system was utilised in our lab for assessing electrical activation. However, due to a limited focal plane, optical mapping of the electrical activation sequence of rabbit atria was not ideal (see Results and Discussion in Chapter 5). A multi-electrode mapping system might be a better tool to map the electrical activation sequence of the rabbit atria. This would facilitate mapping of a three-dimensional tissue.

4.1.2 The hardware in the optical mapping system could be adapted

The data acquisition system for optical mapping system in our lab consists of four data acquisition cards (PXI-6031E, National Instruments), a PXI box (PXI-1042, National Instruments), a PXI-PCI interface kit (PXI-PCI 8335, National Instruments) and a personal computer (DELL) and the possibility was that it could be adapted for a multi-electrode mapping system. Figure 4.1 shows an overview of the system. The four data acquisition cards were the

major components of the data acquisition system. Analogue signals were amplified and converted to digital signals by the data acquisition cards. The PXI box was used to provide power and communication pathways for the data acquisition cards. The PXI-PCI interface kit was used to provide the communication pathway between the PXI box and the personal computer.

The data acquisition card, PXI-6031E, could acquire analogue voltage signals from up to 64 analogue input channels simultaneously when the analogue inputs were configured in a single-ended ground referenced (RSE) mode. However, if the input mode was set as differential (DIFF) mode, it could acquire signals from up to 32 channels simultaneously. That meant the four PXI-6031E cards could acquire analogue voltage signals simultaneously from up to 256 channels in single-ended ground referenced input mode, and up to 128 channels in differential input mode. Figure 4.2 shows the pinout of the data acquisition card.

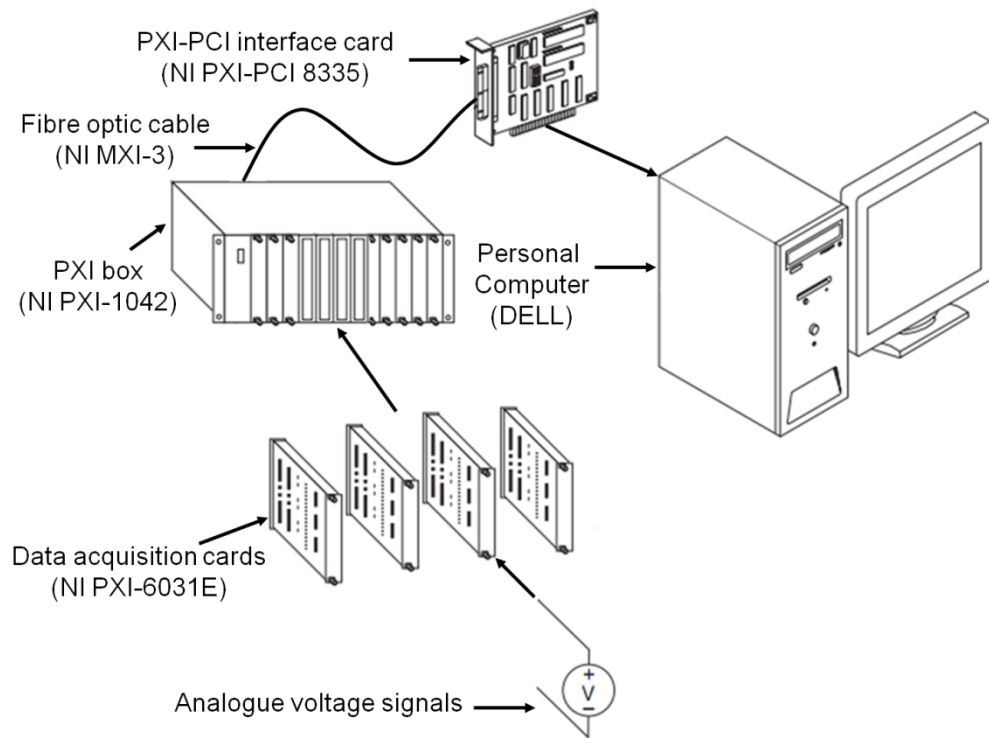


Figure 4.1 Overview of the data acquisition card system in the optical mapping system

Analogue voltage signals can be amplified and converted to digital signals by the four data acquisition cards (NI PXI-6031E), which have power supplied by the PXI box (NI PXI-1042). The digital signals are transferred to a personal computer by a PXI-PCI interface kit consisting of a fibre optic cable (NI MXI-3) and PXI-PCI interface card.

AI GND	1	51	AI 16
	2	52	AI 24
AI 0	3	53	AI 17
AI 8	4	54	AI 25
AI 1	5	55	AI 18
AI 9	6	56	AI 26
AI 2	7	57	AI 19
AI 10	8	58	AI 27
AI 3	9	59	AI 20
AI 11	10	60	AI 28
AI 4	11	61	AI 21
AI 12	12	62	AI 29
AI 5	13	63	AI 22
AI 13	14	64	AI 30
AI 6	15	65	AI 23
AI 14	16	66	AI 31
AI 7	17	67	AI 32
AI 15	18	68	AI 40
	19	69	AI 33
	20	70	AI 41
	21	71	AI 34
	22	72	AI 42
	23	73	AI 35
	24	74	AI 43
	25	75	
	26	76	
	27	77	AI 36
	28	78	AI 44
	29	79	AI 37
	30	80	AI 45
	31	81	AI 38
	32	82	AI 46
	33	83	AI 39
	34	84	AI 47
	35	85	AI 48
	36	86	AI 56
	37	87	AI 49
	38	88	AI 57
	39	89	AI 50
	40	90	AI 58
	41	91	AI 51
	42	92	AI 59
	43	93	AI 52
	44	94	AI 60
	45	95	AI 53
	46	96	AI 61
	47	97	AI 54
	48	98	AI 62
	49	99	AI 55
	50	100	AI 63

Figure 4.2 Pinout of the data acquisition card (NI PXI-6031E)

There were 100 pins in the data acquisition card, but only 65 pins would be used in the multi-electrode mapping system. Functions of the 65 pins are indicated beside the pins. AI indicates analogue input; AI GND indicates analogue input ground. There were 64 pins (AI 0, AI 1 ... AI 63) used for the inputs of the analogue voltage signals, and there was one pin (AI GND) used as the ground in the multi-electrode mapping system. The other 35 pins, which were not be used in the multi-electrode mapping system, are not labelled in this figure.

The maximum sampling rate of the PXI-6031E card was 100 kS/s and this rate could be reached when only one analogue input channel was used. When more than one channel was used simultaneously, the maximum sampling rate for each channel was 100 kS/s divided by the channel number. Hence, when 64 analogue input channels were using simultaneously, the maximum sampling rate for each channel was 1.5 kS/s.

The analogue voltage input resolution of the PXI-6031E card was 16 bits and the input range was ± 0.1 to ± 10 V.

4.1.3 Aim

The aim of this chapter was to develop a multi-electrode mapping system which could be used to map the electrical activation sequence of rabbit atria. It was planned to use the multi-electrode mapping system with arrays. However, repeated plugging and unplugging of the connectors from the PXI-6031E cards might destroy the delicate pins of the expensive PXI-6031E cards. To prevent this, connector extensions for the PXI-6031E were constructed. Development of the multi-electrode mapping system was divided into four parts:

- 1) Construction of four connector extensions for the data acquisition cards to connect the electrodes.
- 2) Construction of electrodes that could be used to record the electrical activity from the epicardium of the rabbit atria.
- 3) Development of software which can be used to control the data acquisition cards to acquire analogue voltage signals and store the

electrograms on a hard drive.

- 4) Development of software which can be used to analyse the electrograms and draw activation sequence maps.

4.2 Materials and methods

4.2.1 Construction of the connector extensions for the data acquisition cards

Four data acquisition cards needed four connector extensions. One 100-way connector (Plug, SCSI, RS Components) and two 37-way connectors (Socket, D-Sub, RS Components) and two 50-way flat cables (Maplin) were employed in each connector extension. The two 50-way flat cables were fixed on the 100-way connectors. Because there were 35 pins in the 100-pin data acquisition cards that would not be used in the multi-electrode mapping system, the corresponding 35 leads in the flat cables were removed. Then the other terminations of the flat cables were soldered to the two 37-way D-Sub connectors using a soldering iron (PS-3D, Weller).

4.2.2 Construction of the multi-electrode arrays

The main materials used in the construction of the multi-electrode arrays included: 37-way connectors (Plug; D-Sub; RS Components); various sized enamelled copper wire (Maplin); various sized shrink tubes (RS Components); various sized silicon tubing (Cole-Parmer); super glue (RS Components) and various sized flat copper braid (RS Components).

The first step to construct the electrode array was to make a template for the organisation of the enamelled copper wires (electrodes). The template was made of a thick (0.2mm) piece of paper; small holes were drilled in the paper using dissection pins (Fine Science) under a binocular microscope. Once the template was finished, the copper wires were inserted one by one in their appropriate holes in the template and fixed by super glue. Then a piece of shrink tube was placed on the copper wires and fixed by a heat gun. The electrodes with shrink tube were then shielded by flat copper braid and inserted in a piece of silicon tubing for protection. Next, the other terminations of the copper wires were soldered to the 37-way connectors. Finally, a black dot was drawn on one side of the electrode array to show the location of the first channel in the array.

4.2.3 Software development environment - LabVIEW

Laboratory Virtual Instrumentation Engineering Workbench (LabVIEW) is a graphical system design platform and development environment for a graphical programming language from the National Instruments Corporation (USA). LabVIEW is widely used for instrument control and data acquisition on various platforms including Microsoft Windows, Linux, UNIX and Mac OS X. It provides excellent integration with many hardware devices and offers built-in libraries for data acquisition, further analysis and visualisation. It is a perfect platform to develop the software needed by the multi-electrode mapping system. Both the recording software and analysis software for the multi-electrode mapping system were developed in LabVIEW 7.1.

4.3 Results

4.3.1 Connector extensions for the data acquisition cards

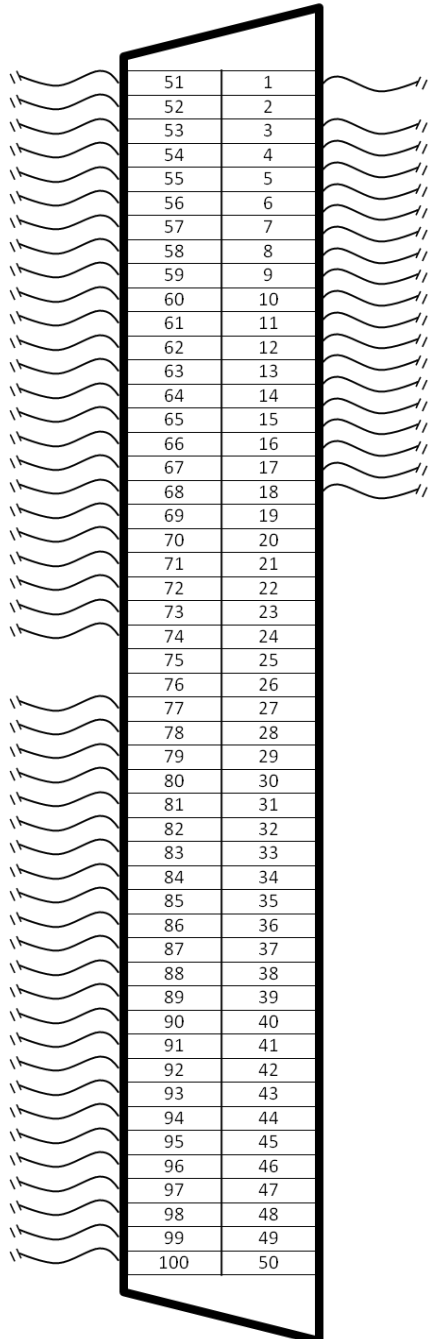
Four connector extensions for the four data acquisition cards were constructed.

Figure 4.3 shows the diagram of the pinout of the connector extensions.

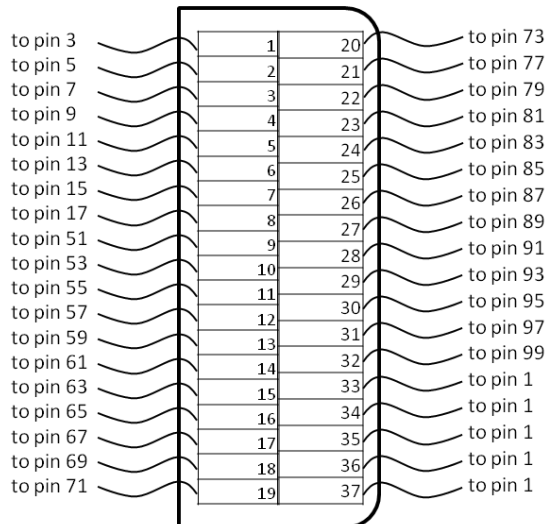
4.3.2 Multi-electrode arrays

Two different sized 64-channel electrode arrays were constructed. The first electrode array (smaller size array) was made of copper wires with a coated diameter of 0.25 mm. The interelectrode distance was approximately 0.7 mm in the longitudinal and 0.35 mm in the transverse direction. The total array dimensions were 4.5 mm length and 1.5 mm width. The length of the copper wires was approximately 2 metres and the silicon tubing used for protection had the same length. Figure 4.4 shows the diagram of its configuration; Figure 4.9A shows photos of this electrode array. The second electrode array (bigger size array) was made of copper wires with a coated diameter of 0.3 mm. The interelectrode distance was approximately 0.9 mm in the longitudinal and 0.75 mm in the transverse direction. The total array dimensions were 14 mm length and 4.5 mm width. The length of the copper wires was about 1.2 metres and the silicon tubing used for protection had the same length. The diagram of its configuration is shown in Figure 4.5.

100-pin connector



37-pin socket connector I



37-pin socket connector II

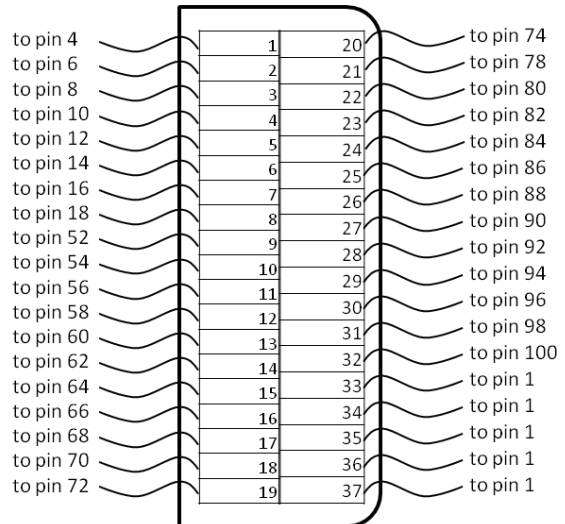


Figure 4.3 Diagram of the pinout of the connector extensions for the data acquisition card

The 100-pin connector connected to the data acquisition card (NI PXI-6031E) and the two 37-pin socket connectors connected to the electrodes. There were 65 pins in the 100-pin connector connected to the two 37-pin connectors. Pin 33, pin 34, pin 35, pin 36 and pin 37 in the 37-pin connectors were connected to pin 1 in the 100-pin connector for the analogue input ground.

4.3.3 Recording software

4.3.3.1 Initialisation of the data acquisition system in the recording software

The recording software consisted of two main interfaces, one was named ‘Initialisation’ interface and the other was named ‘Experiment’ interface. In the ‘Initialisation’ interface (Figure 4.6), the user can initialise the multi-electrode mapping system including selecting data acquisition channels, setting the data acquisition mode and setting the sampling rate and amplification rate.

According to the Nyquist-Shannon sampling theorem, the sampling rate must be at least twice the maximum component frequency of the analogue signals being sampled (Shannon, 1998). Therefore, mapping the activation sequence of rabbit atria requires a high sampling rate. For example, an electrode array with an interelectrode distance of 1 mm to map the activation sequence of rabbit atria with estimated conduction velocity of 1 m/s, the difference in activation time between adjacent electrode is 1 ms (1 kHz), and therefore the best determination of the activation sequence would require a sampling rate of at least 2 kHz in each channel of the multi-electrode mapping system. In the study of this thesis, the highest sampling rate of the data acquisition cards was used in all the mapping experiments.

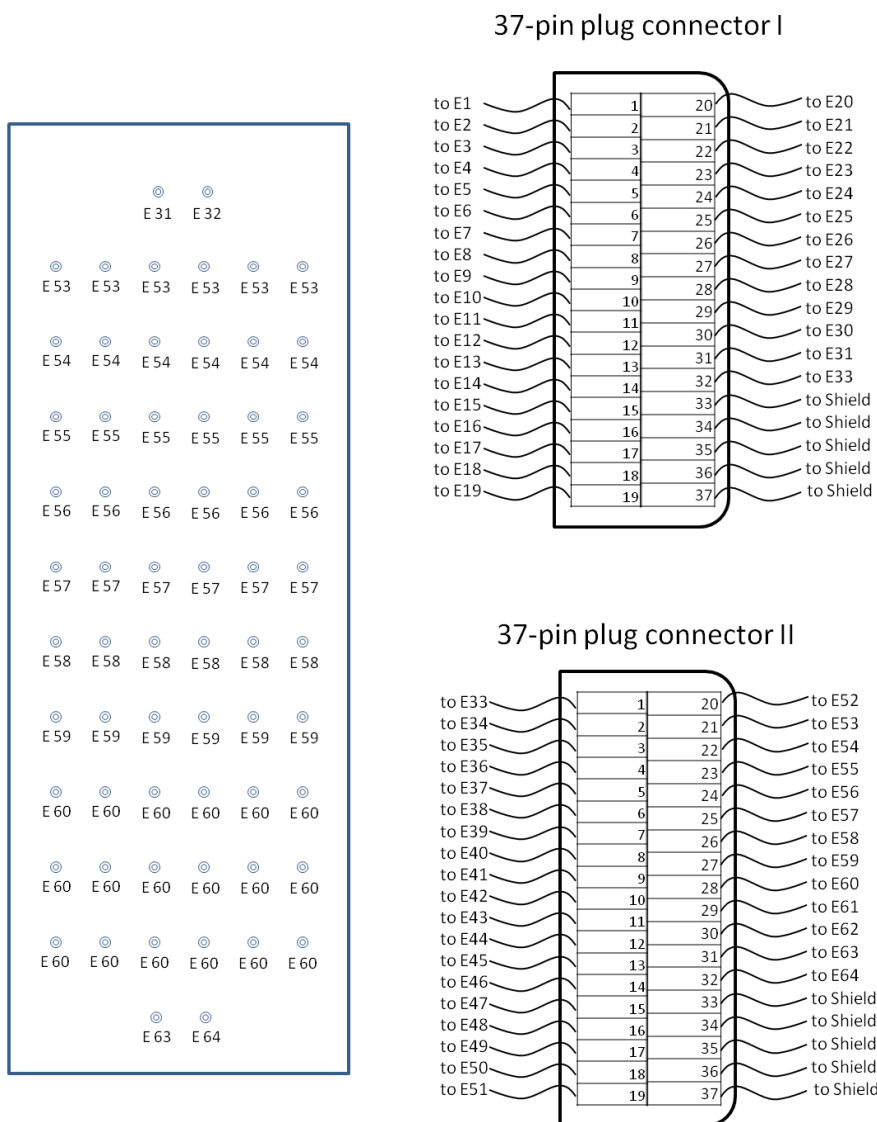


Figure 4.4 Diagram of the smaller size 64 channel electrode array

The left panel shows the configuration of the electrodes in the smaller sized array. The two 37-pin plug connectors were used to connect to the two 37-pin socket connectors in the connector extension (Figure 4.3).

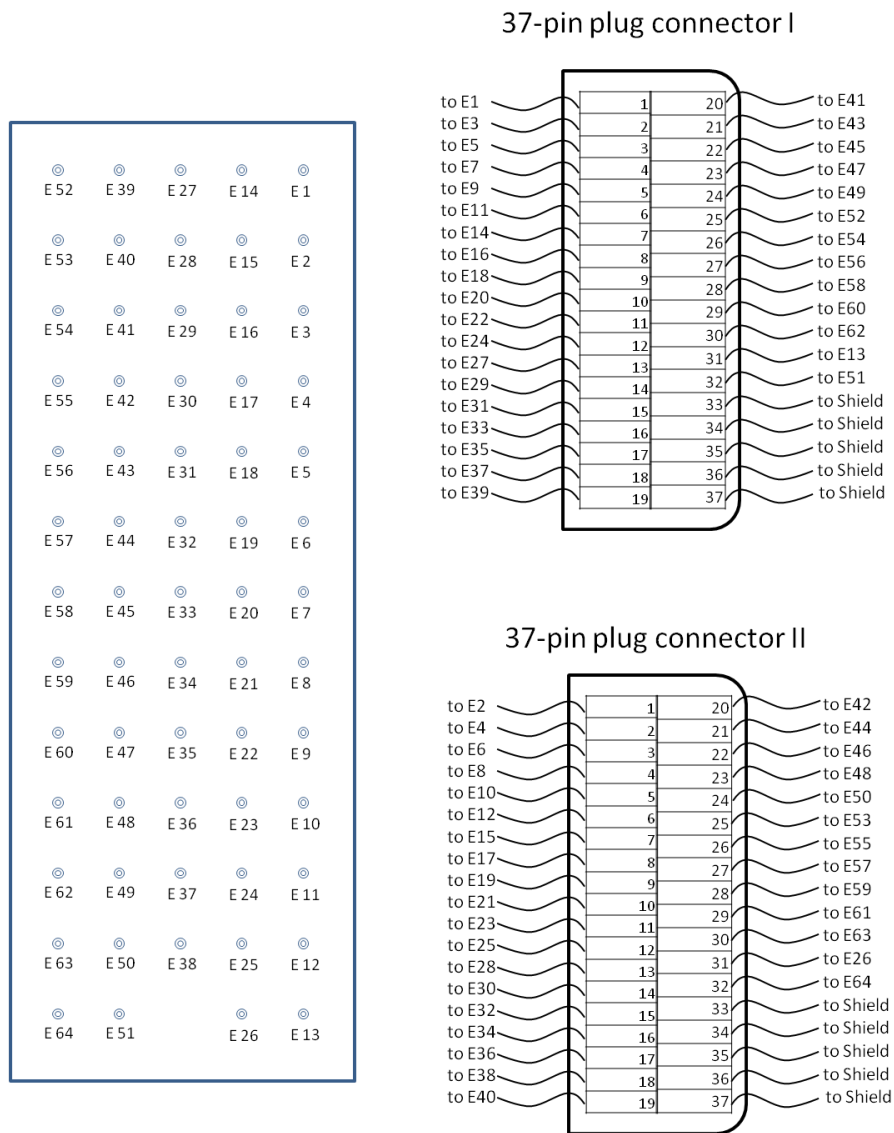


Figure 4.5 Diagram of the larger 64 channel electrode array

The left panel shows the configuration of the electrodes in the larger array. The two 37-pin plug connectors were used to connect to the two 37-pin socket connectors in the connector extension (Figure 4.3).

MEAmapping_v0596_6031E_192_Decration.vi

Initialization

19:26:26
12/04/2011

DAQ Setting

Sampling rate: 1500 Min. input: -1 Max. input: 1

Device I

Channel Parameters

Physical Channel
PXI2Slot2/ai0:63

input terminal configuration
RSE

Device I

Channel Parameters

Physical Channel 2
PXI2Slot3/ai0:63

input terminal configuration 2
RSE


Device III

Channel Parameters

Physical Channel 3
PXI2Slot4/ai0:63

input terminal configuration 3
RSE

Experiment



About

This software was developed by [Guoliang Hao](#) in 2010.
If you need it for your research, please contact us:
Guoliang.Hao@postgrad.manchester.ac.uk
Halina.Dobrzynski@manchester.ac.uk
Mark.Boyett@manchester.ac.uk

Figure 4.6 Initialisation interface of the recording software

Initialisation of the multi-electrode mapping system could be carried out using this interface. Users can select the data acquisitions channels and set the data acquisition mode in the 'Device Channel Parameters' region. The sampling rate and amplification rate can be set in the 'DAQ Setting' region. Users can also save the configuration by clicking the 'Save protocol' button, and reload the configuration by clicking the 'Load protocol' button.

4.3.3.2 Displaying of the multi-channel electrograms in the recording software

After the initialisation of the multi-electrode mapping system, users can begin to acquire the electrograms using the ‘Experiment’ interface of the recording software (Figure 4.7). After clicking the ‘Run’ button, the system begins to acquire electrograms. The electrograms are displayed systematically in the interface (i.e. the electrogram acquired from the first channel in the data acquisition card is displayed at the top and the electrogram acquired from the last channel is displayed at the bottom). This character is important for the user to monitor the electrograms during the experiment. The electrograms can also be magnified for observation during an experiment.

4.3.3.3 Filtering of the multi-channel electrograms in the recording software

There is a digital filter that can be used to filter noise in electrograms. The user is able to switch the filters on and off and control the parameters. The electrograms after filtering are displayed, but they cannot be saved in a file (only the original electrograms can be saved). Further filtering of the electrograms can be performed offline in the analysis software.

4.3.3.4 Recording of the multi-channel electrograms in the recording software

Electrograms can be saved in a file for off-line analysis by switching on the

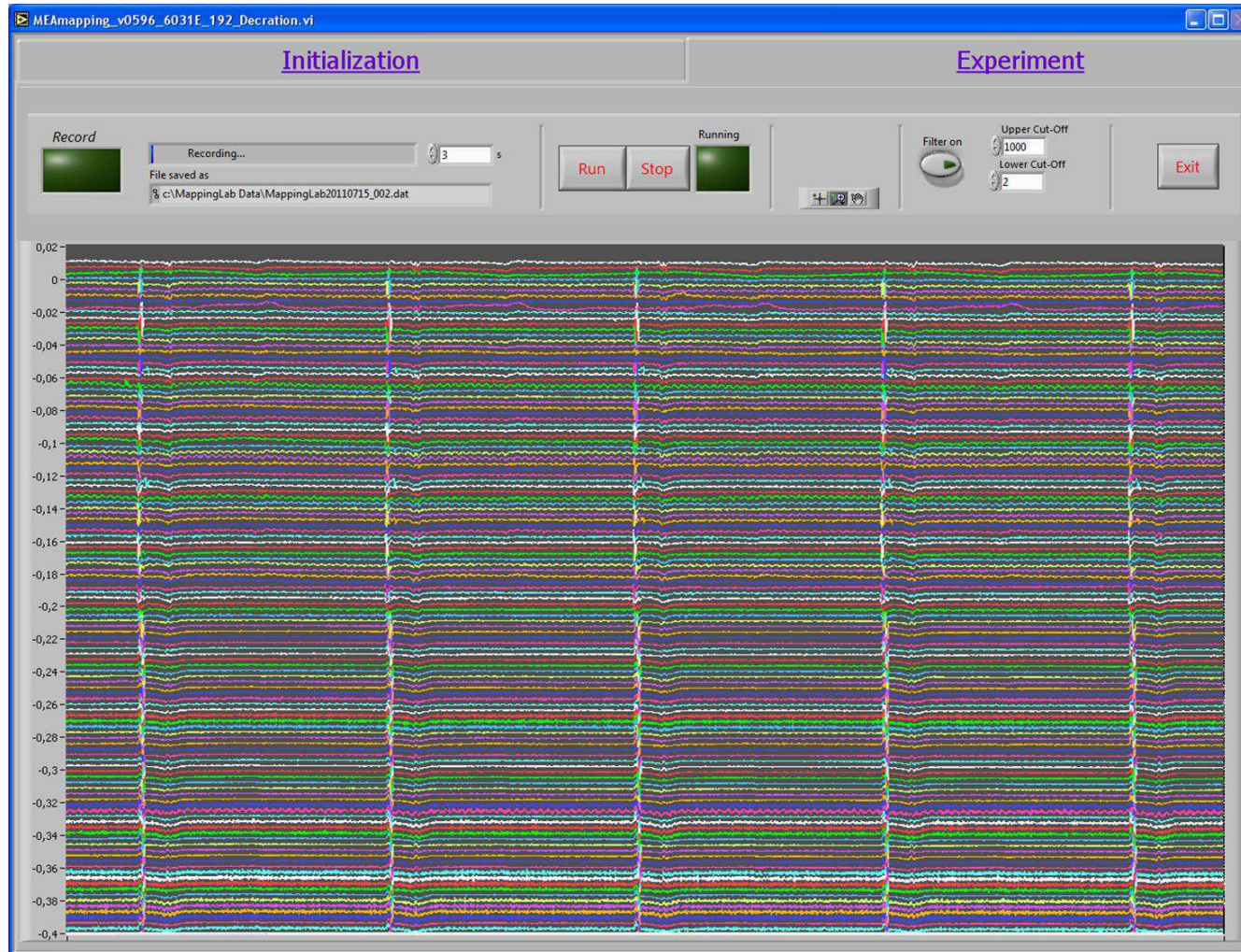


Figure 4.7 Experiment interface of the recording software

Users can begin to acquire and record the electrograms in this interface after initialisation of the multi-electrode mapping system. After clicking the ‘Run’ button, the mapping system begins to acquire electrograms and the electrograms are displayed orderly in this interface; after clicking the ‘Stop’ button, the mapping system stops the data acquisition. In this interface, the electrograms can also be filtered by a digital filter and be saved in a file for off-line analysis by clicking the ‘Record’ button.

'Recording' button in the 'Experiment' interface. The recording length can be set by the user and the file name can be automatically generated by the software according to the experiment date.

4.3.4 Analysis software

4.3.4.1 Determination of the local activation time

The analysis software developed in LabVIEW can be used to analyse the electrograms and determine the local activation time in each electrogram. Figure 4.8 shows the main interface of the analysis software. The electrograms recorded in the recording software can be imported into the analysis software, and each electrogram is labelled with a cursor. The cursors can be moved manually and the coordinates of the cursors are displayed in the interface. The maximal negative dV/dt in each electrogram is automatically found and labelled by the cursors. The maximal negative dV/dt is taken as the local activation time in this study. After finding the local activation time of each channel, the local activation time data can be exported to a text file for further analysis.

4.3.4.2 Drawing of activation map

A script file was developed in MATLAB to draw the activation maps. The local activation time data exported from the analysis software can be copied into the script file. Then, an activation map can be drawn based on the local activation times by running the script file in MATLAB.

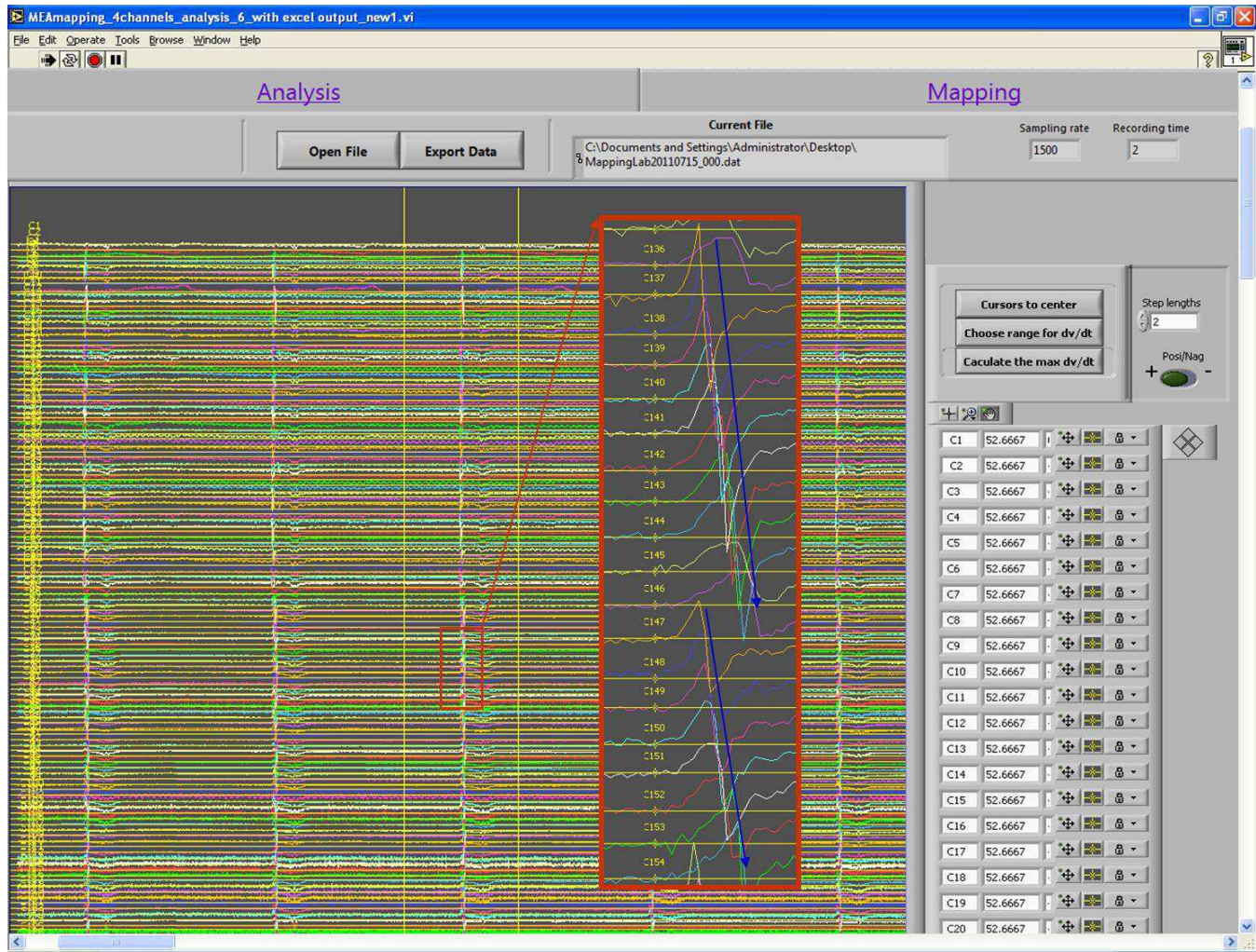


Figure 4.8 Analysis software of the multi-electrode mapping system

Rabbit electrograms recorded in the mapping system can be imported into this software by clicking 'Open File'. The electrograms are displayed in the order of acquisition and each of them is labelled with a cursor. The electrograms can be magnified (the electrograms in the large red rectangle show the electrograms in the smaller red rectangle after being magnified; the blue arrows show the direction of conduction). After clicking the 'Choose range for dV/dt', two vertical cursors are shown in the interface, and then the user can use the two cursors to choose the range where to find the activation time. The maximal negative dV/dt in each electrogram is automatically found and labelled with its cursor by clicking the 'Calculate the max dV/dt'. After finding the local activation time of each channel, the data of the local activation time can be exported to a text file by clicking 'Export Data'.

4.4 Discussion

Four connector extensions for the data acquisition cards and two different sized 64-channel electrode arrays were constructed. The recording software and analysis software for the multi-electrode mapping system was developed in LabVIEW and MATLAB. After finishing the multi-electrode mapping system, I mapped the electrical activation sequence of Bachmann's bundle of a Langendorff-perfused rabbit heart. Figure 4.9 shows the electrode array used in this experiment and the original electrograms acquired by the mapping system and the activation map drawn in MATLAB. The electrograms were clean, and could be easily analysed in the analysis software. The activation map clearly showed the action potential propagated from the superior vena cava region to the left atrial appendage through Bachmann's bundle. This experiment proved it was feasible to map the activation sequence of the Langendorff-perfused rabbit heart using the multi-electrode mapping system and it was also feasible to map the activation sequence of the whole rabbit atria with more electrode arrays.

With this mapping system, in addition to mapping the activation sequence of rabbit atria, I also mapped the activation sequence in other tissues including MKK4 knockout mice ventricles (see Figure 5 in Appendix III; Zi et al., 2011), mouse sinoatrial node preparations, rat sinoatrial node preparations, rat atrioventricular ring tissues and anaesthetised goat sinoatrial node (in vivo). In all these experiments, the multi-electrode mapping system performed very well.

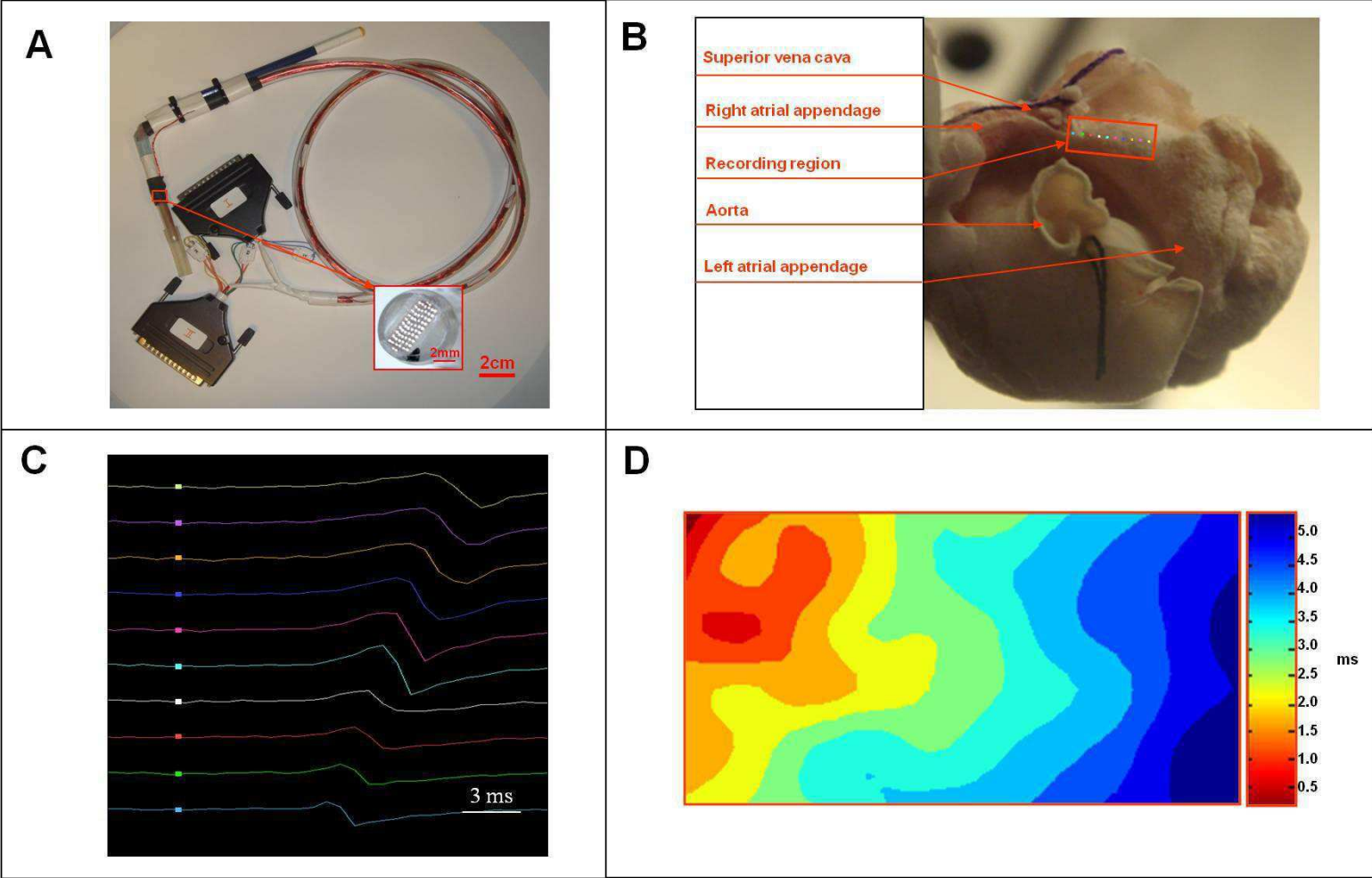


Figure 4.9 An example of a mapping experiment carried out on rabbit Bachmann's bundle

A, custom-designed 64 channel electrode array used in the experiment. A high power view of the electrode head is shown in the red square. B, frozen rabbit heart used to show the region (in red rectangle) from where the extracellular electrograms were recorded. C, original electrograms recorded from rabbit Bachmann's bundle. D, activation map constructed based on the local activation times acquired from the original electrograms.

Chapter 5 Experimental mapping and computer simulation of the electrical activation sequence of the rabbit atria

5.1 Introduction

5.1.1 Interatrial conduction routes

Bachmann's bundle and the atrial septum are regarded as two of the most important routes for the action potential propagating from the right atrium to the left atrium (Bachmann, 1916; Lemery et al., 2004; Seemann et al., 2006). In addition, several anatomical studies of human hearts and canine hearts have also shown that the coronary sinus provides a muscular connection between the right and left atrium (Chauvin et al., 2000; Lemmon et al., 1997; Maros et al., 1983; Sealy, 1994). Electrophysiological study of the canine heart has also shown the coronary sinus musculature forms an electrical connection between the two atria (Mohammadi and Hawkins, 1998). The human heart mapping study carried out by Boineau et al. (1988), showed that the coronary sinus provides a conduction route for the action potential to propagate from the right atrium to the left.

The coronary sinus in the rabbit heart, as shown in the 3D anatomical model

(Figure 3.9), is a big vessel connecting to the left superior vena cava (LSVC). This vessel (coronary sinus and the LSVC) forms a big muscular connection between the right and left atrium, and therefore it will play an important role in the electrical activation pattern of the rabbit atria if it provides an interatrial conduction pathway.

5.1.2 About experimental mapping in the rabbit atria

Experimental mapping techniques including optical mapping and multi-electrode mapping provide important tools to study the electrical activation of the heart. The experimental mapping data can be used to support and validate the computer simulation work. Both optical mapping and multi-electrode mapping techniques have been employed to study electrical activation during sinus rhythm in human atria (Cosio et al., 2004; Durrer et al., 1970), canine atria (Hayashi et al., 1982; Kumagai et al., 2000; Schuessler et al., 1993) and rabbit atria (De Carvalho et al., 1959; Eijsbouts et al., 2003; Fedorov et al., 2007). Regarding mapping of electrical activation of rabbit atria, De Carvalho et al. (1959) performed mapping in the rabbit right atrium with two sharp microelectrodes. Their data showed it took around 70 ms for the action potential to propagate from the SAN to the right atrial appendage (De Carvalho et al., 1959). Eijsbouts et al. (2003) mapped both the right and left atria with multi-electrode arrays, but they did not cover all the regions of the atria (Eijsbouts et al., 2003). Fedorov et al. (2007) mapped the atria and part of the ventricles using a 16 x 16 photodiode array optical mapping system with a 32 x 32 mm mapping area; the activation maps are shown in Figure 5.1. As

described in Section 1.2.2, the contraction of the muscle causes artefacts in optical mapping experiments. In the study of Fedorov et al. (2007), two ways to alleviate the contraction of the heart were used. The first way was to mechanically reduce the contractile movement by stretching the tissue with some pins. The second way was to perfuse the heart with an excitation-contraction uncoupler – blebbisatin. Figure 5.1A shows the activation maps in the rabbit atria and part of ventricles without using blebbisatin; some regions of the heart could not be mapped properly, because of the motion artefact. After using 10 μ M blebbisatin, as shown in Figure 5.1B, most regions of the rabbit atria were mapped, but the activation map was still not detailed enough (ie. activation sequences in Bachmann’s bundle, coronary sinus, pulmonary veins etc. are not clear). In addition, as shown in the optical mapping results of Fedorov et al. (2007), it took only around 18 ms for the action potential to propagate from the SAN to the right atrial appendage, which is very different to the data from De Carvalho et al. (1959).

5.1.3 About computer simulation of the whole rabbit atria

As described in section 1.3, in addition to experimental mapping techniques, computer simulation also provides a very important platform to study the fundamental mechanisms underlying normal and abnormal activation of the atria.

Based on a 3D rabbit right atrium model, Dr. Jue Li (University of Manchester) simulated the propagation of the action potential in the rabbit right atrium

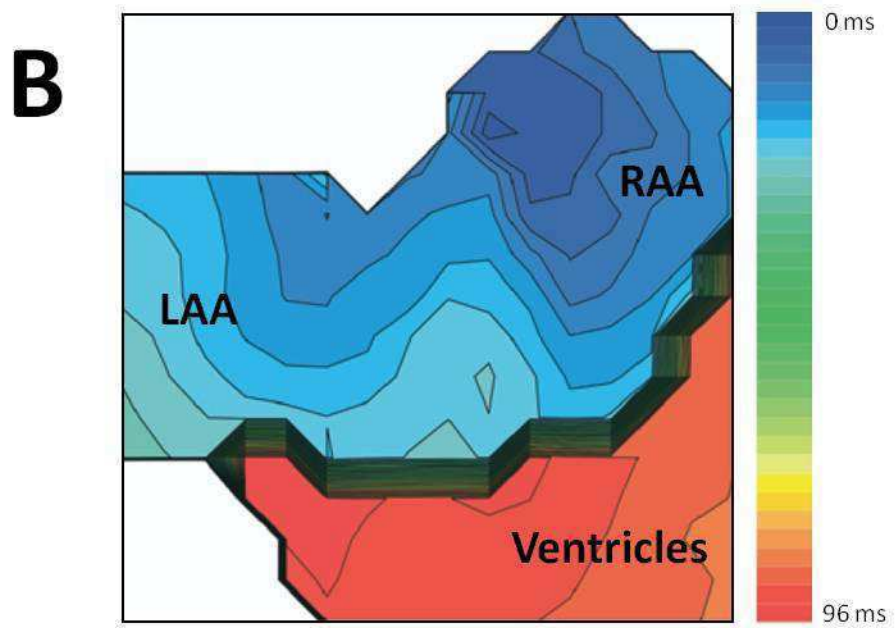
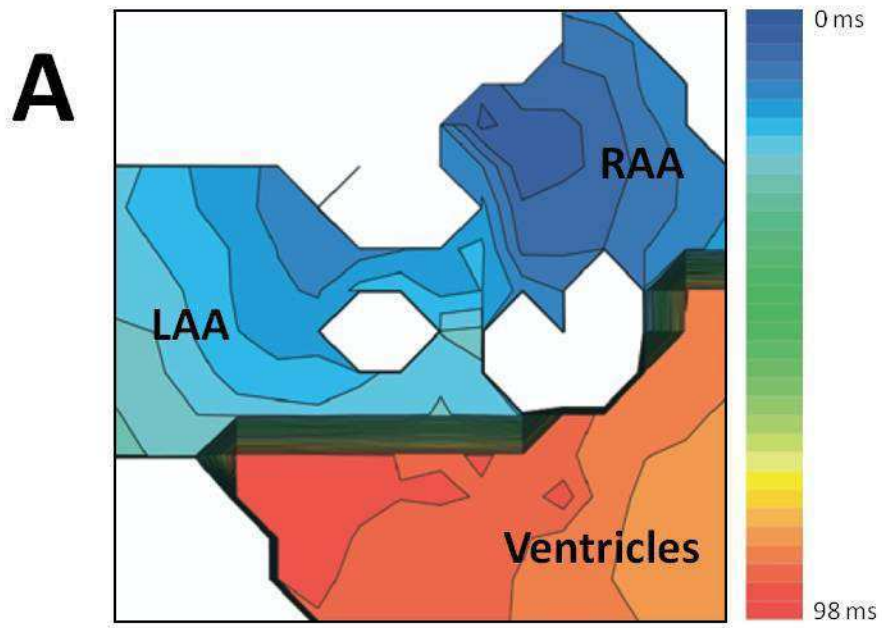


Figure 5.1 Epicardial activation maps of the Langendorff-perfused rabbit heart mapped with an optical mapping system

A, epicardial activation map of the rabbit heart during sinus rhythm without blebbistatin. B, epicardial activation map of the rabbit heart during sinus rhythm with 10 μ M blebbistatin. Earliest activation is found in dark blue, latest in dark red. The color bar and numbers indicate activation time in ms. LAA, left atrial appendage; RAA, right atrial appendage. Adapted and modified from Fedorov et al. (2007).

(unpublished data). There is no computer simulation of the two atria of the rabbit.

5.1.4 Aims

The first aim of chapter was to map electrical activation of Langendorff-perfused rabbit atria during sinus rhythm using optical mapping and multi-electrode mapping techniques. This will show if the coronary sinus and the LSVC provide an interatrial conduction route during sinus rhythm in the rabbit heart. This will also allow measurement of conduction velocities in the atria. Some studies have shown the conduction velocity in Bachmann's bundle is faster than that in other parts of atria (Childers et al., 1968; Hayashi et al., 1982; Wagner et al., 1966). These data can be used to support and validate computer simulation work.

The second aim of this chapter was to simulate electrical activation of the rabbit atria using the cellular automaton model of action potential conduction and the detailed 3D anatomical model of the rabbit atria described in Chapter 3.

5.2 Materials and methods

5.2.1 Animals and preparations

New Zealand White rabbits (male; 1.5 to 2 kg) were anaesthetised with pentobarbital (30 to 40 mg/kg IV), and then the chest was opened and the heart was quickly excised and submerged in Krebs-Ringer solution at 4°C. This study conformed to the United Kingdom Animals (Scientific Procedures) Act,

1986. The heart was cannulated with a stainless steel cannula and connected to the Langendorff perfusion system. Perfusion was performed at a constant flow rate of 20 ml/min. The composition of the Krebs-Ringer solution was as follows (mM): NaCl 120.3; KCl 4.0; CaCl₂ 1.2; MgSO₄ 1.3; NaH₂PO₄ 1.2; NaHCO₃ 25.2; glucose 11.0 (pH 7.4, equilibrated with 95% O₂/5%CO₂).

5.2.2 Optical mapping

Two rabbits were sacrificed for the optical mapping experiments. The rabbit heart was perfused with the Krebs-Ringer solution for 10 min to washout the blood remaining in the coronary arteries and veins. Then the heart was stained with the voltage sensitive dye RH237 by perfusion of the Krebs-Ringer solution with 2 μM RH237 for 20 min. Then the Langendorff-perfused heart was positioned in a custom-designed chamber with the atria facing a 256-channel optical mapping system.

As shown in Figure 5.1, the excitation-contraction uncoupler may slightly change the activation sequence of the rabbit heart. In this study, therefore, an excitation-contraction uncoupler was not used to alleviate the contraction in order to map the activation sequence of the rabbit atria. The atria appendages were pinned in a custom-designed chamber to mechanically reduce the contractile movement of the atria. Figure 1.1 shows the optical mapping system used in this study. The optical signals were recorded from 10 x 10 mm areas of the atria at a rate of 1500 frames per second. The data were monitored and transferred to the computer by custom-written software for off-line analysis.

5.2.3 Multi-electrode mapping

5.2.3.1 Bipolar electrode mapping

Two rabbits were sacrificed for the bipolar electrode mapping experiments. Langendorff-perfused heart preparations were made as described in Section 5.2.1. Twelve custom-designed steel bipolar electrodes were used to record the extracellular potentials from 12 different regions in the rabbit atria. Positioning of the electrodes in the atria is shown by the red arrows in Figures 5.4 and 5.5. The 12 electrograms were simultaneously recorded in the software described in section 4.3.3. The sampling rate was set as 3000 Hz and the amplification rate was set as 100. The electrograms were analysed in the software described in section 4.3.4.

5.2.3.2 Multi-electrode array mapping

Five Langendorff-perfused rabbit heart preparations were made for the multi-electrode array mapping experiments. Three multi-electrode arrays were used to map the electrical activation of the rabbit atria. All of these three electrode arrays were 64-channel arrays. Two of them were constructed by the author; detailed information of these two electrode arrays is described in Section 4.3.2. The third electrode array (width, 3.7 mm; length, 4.5 mm) was constructed by Dr. Athiq Wahab in 2008. The three multi-electrode arrays were attached to XYZ micromanipulators calibrated to 0.1 mm precision and gently touched on the epicardium of the Langendorff-perfused heart atria to record the extracellular potentials. In addition to the three electrode arrays, a bipolar

electrode was used as a static reference electrode. The bipolar electrode was gently clamped to the tip of right atrial appendage to record the extracellular potential at this point. The stainless steel cannula was connected to the ground channel of the multi-electrode mapping system as an indifferent electrode. The electrograms were monitored and recorded in the software described in Section 4.3.3. The sampling rate was set as 1500 Hz and the amplification was set at 100. The electrograms were analysed in the software described in Section 4.3.4. The activation maps were drawn in MATLAB and Adobe Illustrator.

Data are presented as mean \pm SEM (standard error of mean).

5.2.4 Anatomical model employed in the computer simulation

The detailed 3D anatomical model of the rabbit atria, which is described in Chapter 3, was used in computer simulation in this chapter. The 3D ‘Model Array’ in MATLAB described in Chapter 3 was converted to five binary files. The binary files were read into the RAM of the computer cluster used to run the simulation program. The five binary files consisted of about 4 million nodes; voxel size of each node was 60 μm x 60 μm x 60 μm . Each node was equivalent to a cluster of myocytes or connective tissue in the rabbit atria.

5.2.5 Cellular automaton model

The cellular automaton model is a useful and simple model to calculate the electrical activation sequence in a complex anatomical model (Bub et al., 2003; Gerhardt et al., 1990; Li et al., 2008). It was used in this study to simulate

action potential propagation in the rabbit atria. The setting of the cellular automaton model in this study is shown in Figure 5.2. Each node in the anatomical model array can be set at one of three states: resting, excited or refractory (Figure 5.2A). In resting state, the state index of the node is set as 0, and the node cannot excite its neighbouring node, but it is able to be excited by them. Figure 5.2B shows how the neighbouring nodes were defined. Node j is defined as one neighbouring node of node i if node j is found in the ellipsoid whose coordinates are defined by the position of node i and the values of R_x , R_y and R_z . In the excited state, the state index of the node is set as 1, and the node can excite its neighbouring nodes. If a node is in its refractory state, its state index is set as 0, and it can neither excite neighbouring nodes nor be excited.

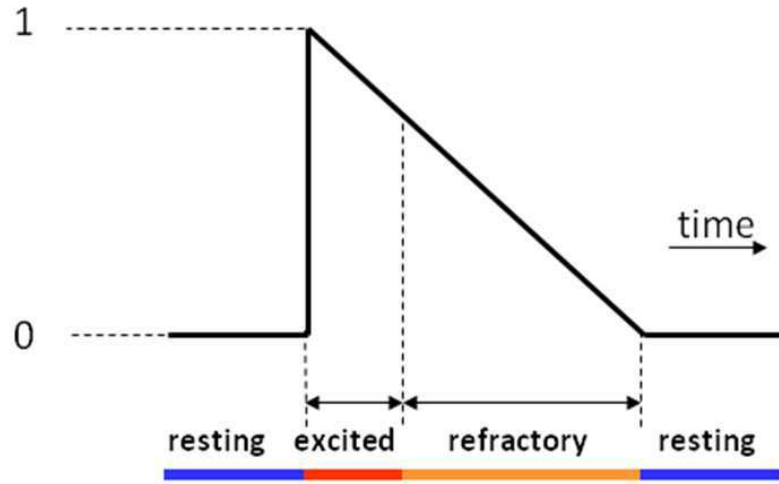
The use of an ellipsoid (Figure 5.2B) in the definition of neighbouring nodes makes it possible to set different conduction velocities and anisotropic properties in different cardiac tissues in the anatomical model. In this study, the conduction velocities in different cardiac tissues were set based on the experimental mapping data. Simulations were coded in C++ and were run on 40 nodes of a computer cluster with the Linux operating system.

5.3 Results

5.3.1 Optical mapping

An example of a result conducted from the 256-channel optical mapping system is shown in Figure 5.3. Figure 5.3A is the image from the visible light

A



B

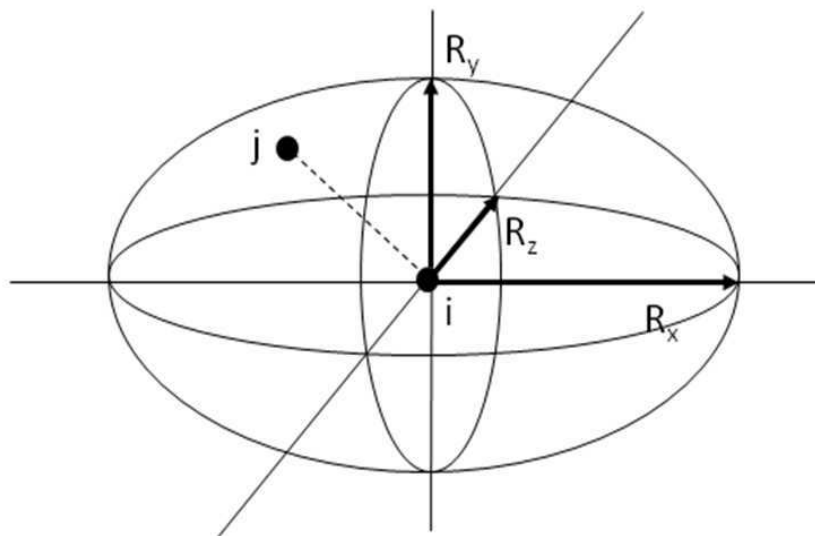


Figure 5.2 Setting of the cellular automaton model of action potential conduction

A, time course of the state of a node in the anatomical model. 0 is used to indicate the resting state of a node and 1 is used to indicate the excited state. A node in the resting state can be excited and then return to the resting state. B, definition of neighbouring nodes of a node in the anatomical model. All of the nodes in the ellipsoid are defined as neighbouring nodes of node i . R_x , R_y and R_z are parameters used to control the shape and size of the ellipsoid. Adapted and modified from Li et al. (2008).

camera showing the mapping area in the Langendorff-perfused rabbit heart. As described in section 1.2.2, the visible light camera and the PDA in the optical mapping system have the same focus, and so the camera can be used to determine if the tissue is on the focus of the mapping system or not. The white dashed curve in Figure 5.3A shows the area of the atria on the focus of the optical mapping system. Figure 5.3B shows the 256-channel (16 x 16) optical action potentials recorded from the corresponding area using the 256-channel optical mapping system.

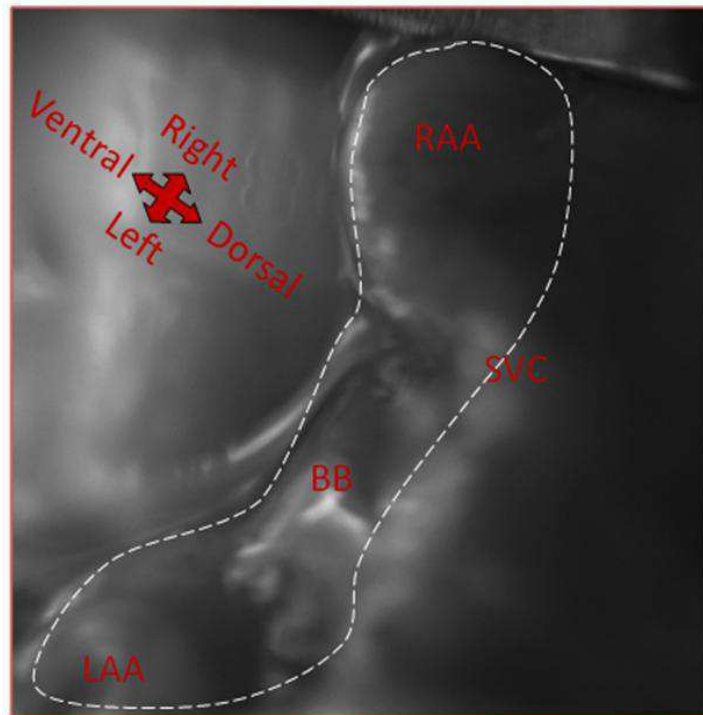
As shown in Figure 5.3B, almost all of the optical action potential signals recorded from the regions outside of the white dashed curve area have strange shapes. Local activation times were difficult to determine with such signals and the activation map could not be drawn for these regions. However, the signals recorded from the Bachmann's bundle region on the focus of the mapping system were clear and the local activation times could be determined. From the mapping results shown in Figure 5.3, the conduction velocity in Bachmann's bundle was determined as 89 cm/s (n=1).

5.3.2 Multi-electrode mapping

5.3.2.1 Bipolar electrode mapping

Twelve different regions in the rabbit atria were mapped by the bipolar electrodes. Using the dorsal view of the 3D rabbit atria model, Figures 5.4 and 5.5 show the positioning of the electrodes (red arrows) and the local activation times in milliseconds (white numbers) in two preparations.

A



B

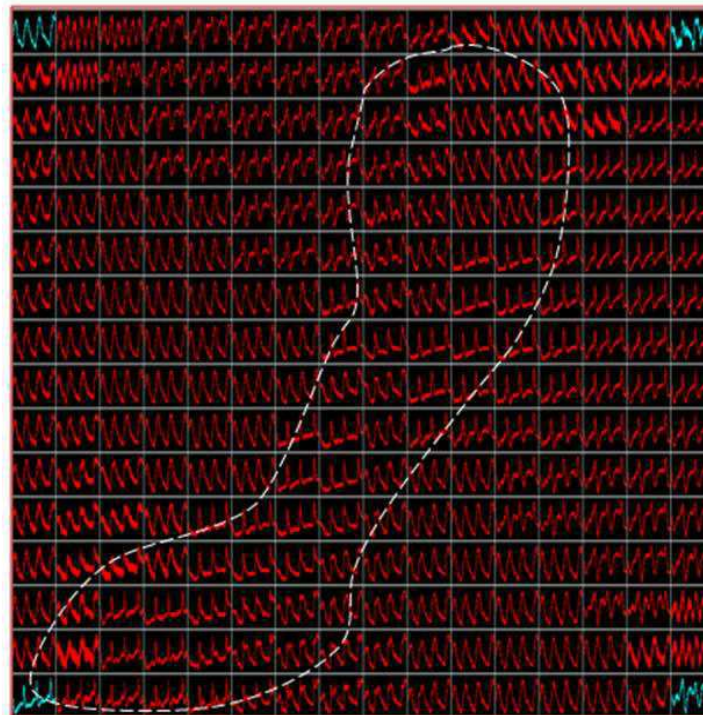


Figure 5.3 An example of a result obtained using the 256-channel optical mapping system

A, a visible light camera image of the Langendorff-perfused rabbit heart showing the mapping area. The white dashed curve shows the area of the atria on the focus of the optical mapping system. B, an example of optical action potentials recorded from the tissue above using the 256-channel optical mapping system. BB, Bachmann's bundle; LAA, left atrial appendage; RAA, right atrial appendage; SVC, superior vena cava.

As shown in Figures 5.4 and 5.5, the activation patterns of the two preparations were similar. The earliest activation site was found in the SAN region. The activation time of the SAN is shown as 0 ms, and the numbers in other regions show the time for the action potential to propagate from the SAN to the site. The regions to activate last were found in the tip of right atrial appendage and bottom of the left superior vena cava. In the right atrial appendage, the activation times of the recording sites ranged from 6 to 16 ms; in the left atrial appendage, the activation times ranged from 14 to 27 ms. The pulmonary vein region activated around 13 to 16 ms later than the SAN. The left superior vena cava activated even later than the pulmonary vein region.

5.3.2.2 Multi-electrode array mapping

The electrical activation sequences of five Langendorff-perfused rabbit atria during sinus rhythm were mapped with the multi-electrode array mapping system. About 1,600 sites were mapped in each preparation. The mapping spatial resolution was around 0.2 mm. Representative activation maps are shown in Figures 5.6 and 5.7. The earliest excitation region in the atria was found in the SAN and the last excitation regions were found in the tip of the left atrial appendage and the bottom of the left superior vena cava. The action potential propagated from the SAN to the whole right atrium in 6 to 20 ms, and to the whole left atrium in 12 to 30 ms.

As shown in Figures 5.6 and 5.7, arrow 1 indicates that the action potential propagated from the SAN down to the inferior vena cava through the crista terminalis; arrow 2 shows that the action potential propagated from the SAN

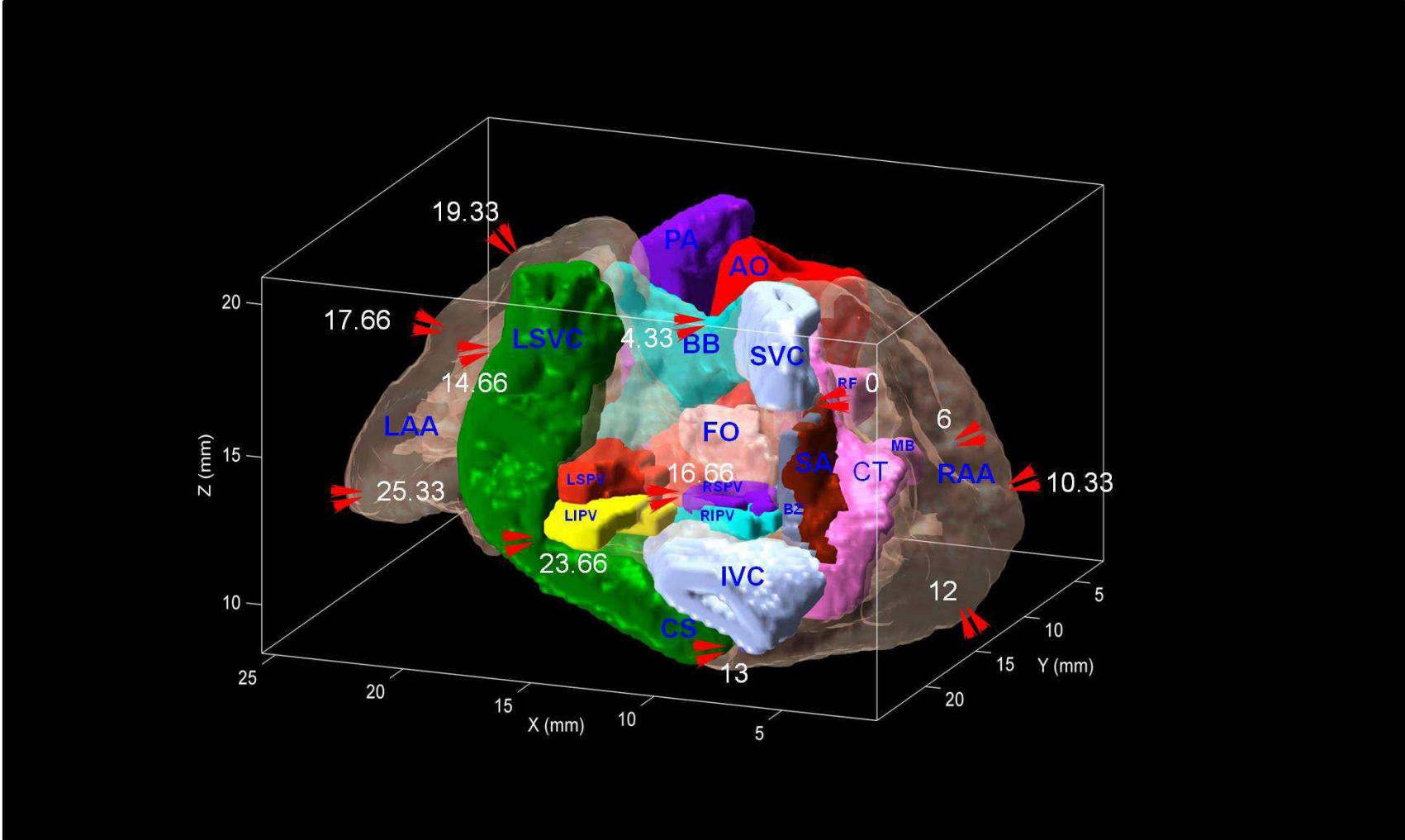


Figure 5.4 Mapping result obtained using the twelve bipolar electrodes (preparation I)

Red arrows indicate the position of the bipolar electrodes. Numbers in white indicate the local activation times in milliseconds. AO, aorta; BB, Bachmann's bundle; CS, coronary sinus; CT, crista terminalis; IVC, inferior vena cava; LAA, left atrial appendage; LIPV, left inferior pulmonary vein; LSPV, left superior pulmonary vein; LSVC, left superior vena cava; MB, main branch; PA, pulmonary artery; RAA, right atrial appendage; RB, roof bundle; RSPV, right superior pulmonary vein; RSVC, right superior vena cava; SA, sinus node.

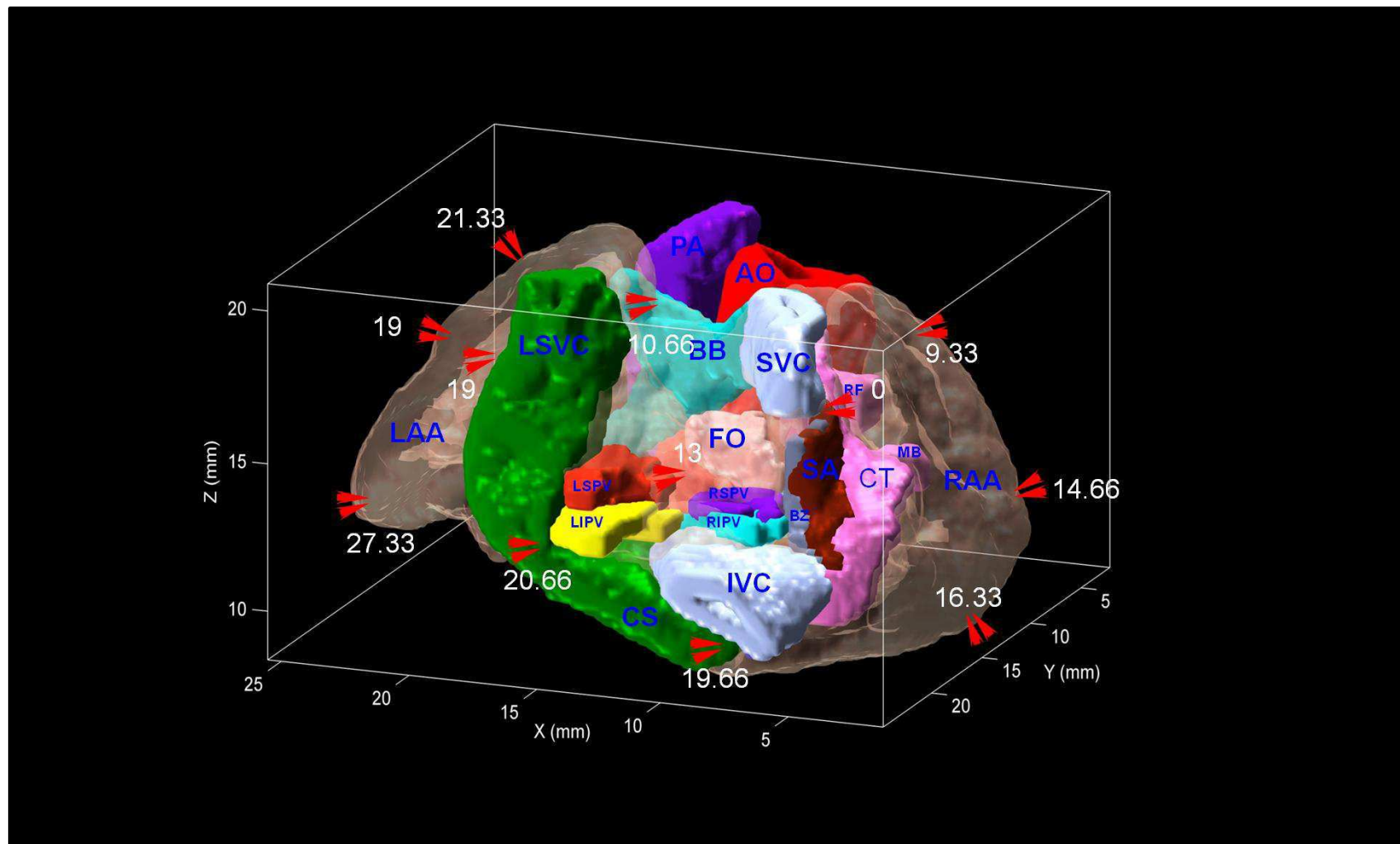


Figure 5.5 Mapping result obtained using the twelve bipolar electrodes (preparation II)

Red arrows indicate the position of the bipolar electrodes. Numbers in white indicate the local activation times in milliseconds. AO, aorta; BB, Bachmann's bundle; CS, coronary sinus; CT, crista terminalis; IVC, inferior vena cava; LAA, left atrial appendage; LIPV, left inferior pulmonary vein; LSPV, left superior pulmonary vein; LSVC, left superior vena cava; MB, main branch; PA, pulmonary artery; RAA, right atrial appendage; RB, roof bundle; RSPV, right superior pulmonary vein; RSVC, right superior vena cava; SA, sinus node.

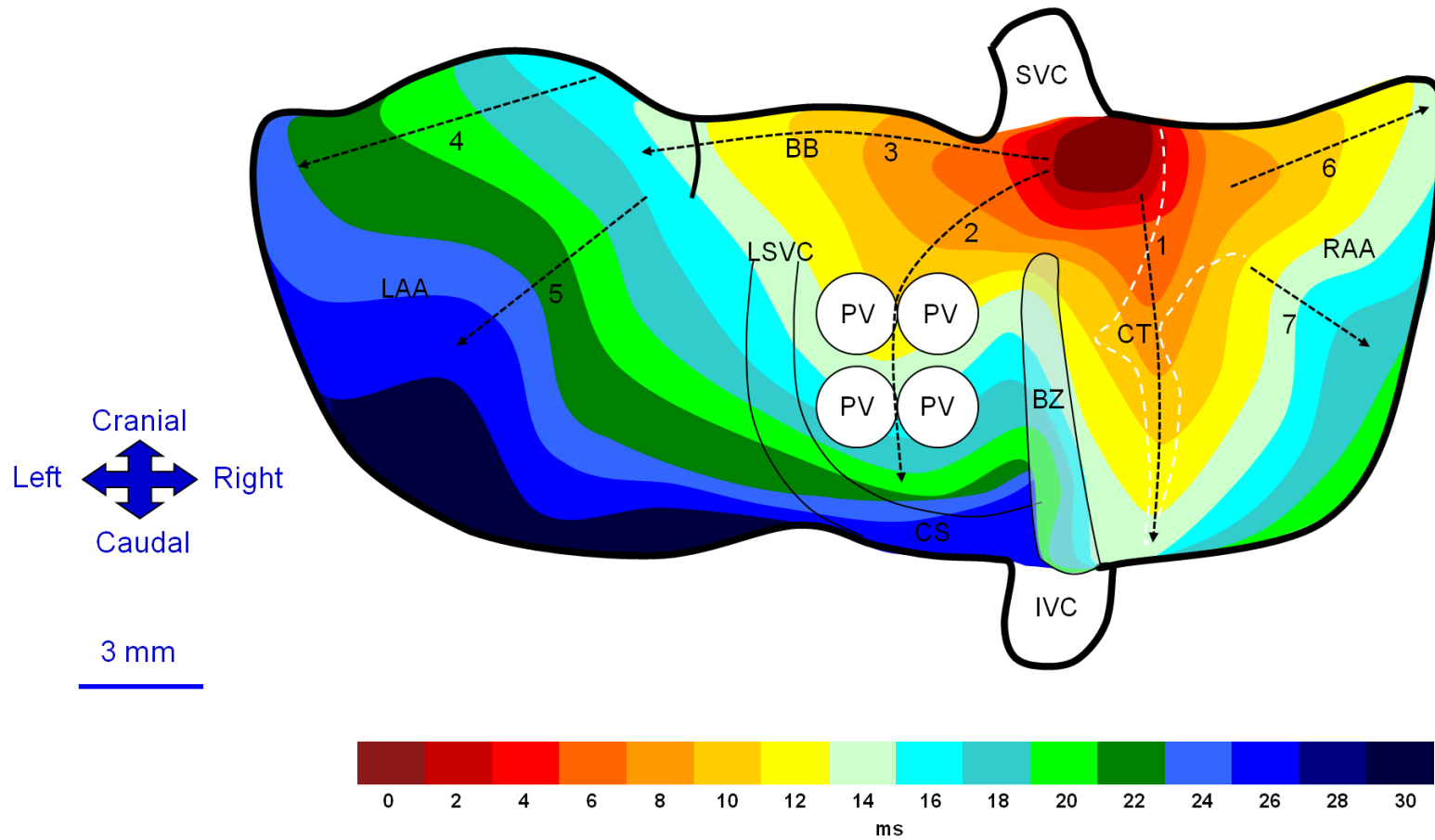


Figure 5.6 Representative epicardial activation map (dorsal view) of the Langendorff-perfused rabbit atria mapped with multi-electrode mapping system

Earliest activation is shown in dark red, latest in dark blue; numbers in the colour bar indicate the activation time in milliseconds. The black dashed lines show the direction of action potential propagation. The white dashed line shows the anatomy of the crista terminalis. The stippled region between the SVC and IVC shows the block zone, where the conduction velocity is very low. BB, Bachmann's bundle; BZ, block zone; CS, coronary sinus; CT, crista terminalis; IVC, inferior vena cava; LAA, left atrial appendage; LIPV, left inferior pulmonary vein; PV, pulmonary vein; RAA, right atrial appendage; SVC, superior vena cava.

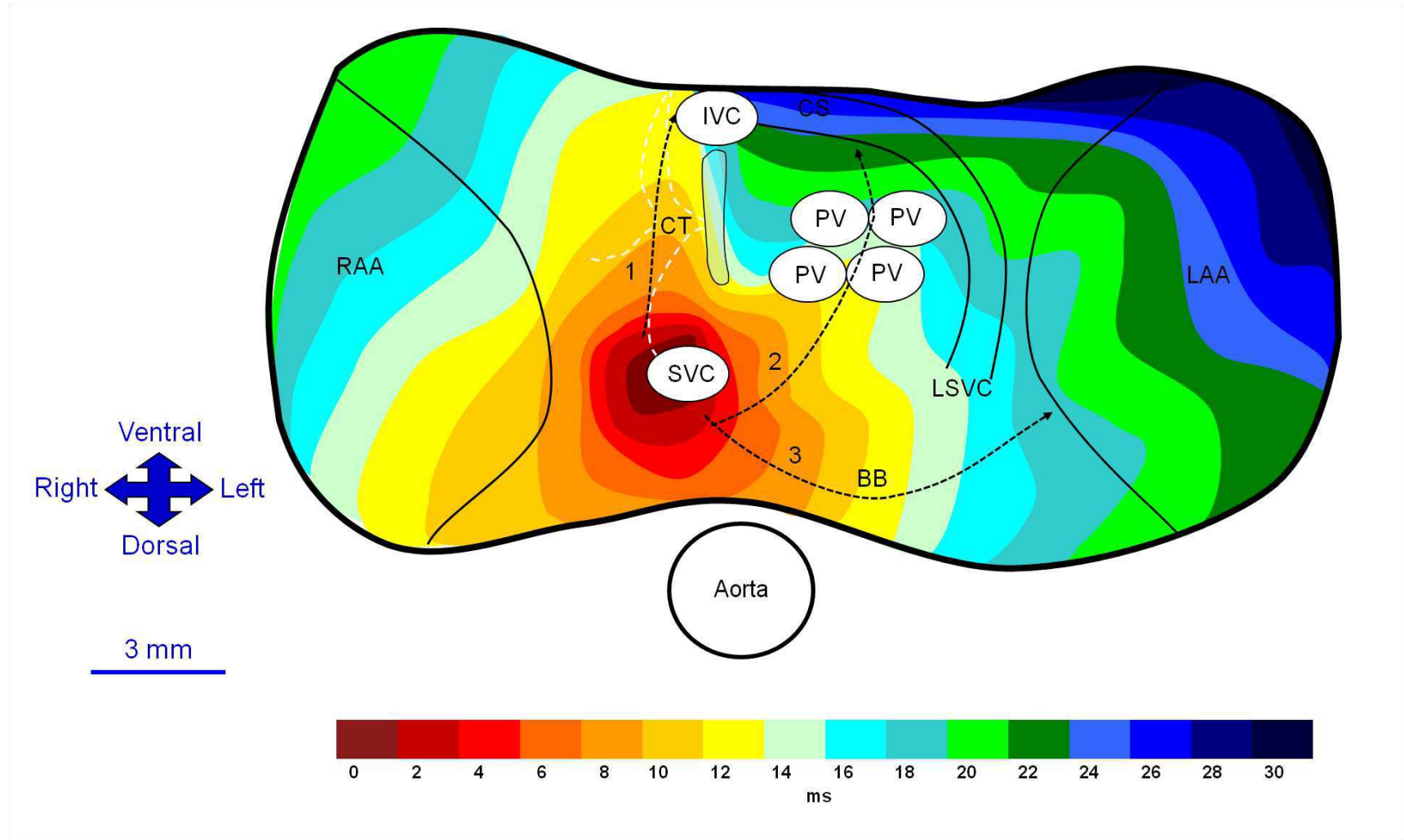


Figure 5.7 Representative epicardial activation map (top view) of the Langendorff-perfused rabbit atria mapped with multi-electrode mapping system

Earliest activation is shown in dark red, latest in dark blue; numbers in the colour bar indicate the activation time in milliseconds. The black dashed lines show the direction of action potential propagation. The white dashed line shows the anatomy of the crista terminalis. The tipped region between the SVC and IVC shows the block zone, where the conduction velocity is very low. BB, Bachmann's bundle; BZ, block zone; CS, coronary sinus; CT, crista terminalis; IVC, inferior vena cava; LAA, left atrial appendage; LIPV, left inferior pulmonary vein; PV, pulmonary vein; RAA, right atrial appendage; SVC, superior vena cava.

down to the pulmonary veins and then to the coronary sinus; arrow 3 shows that the action potential propagated from SAN to the left atrial appendage through Bachmann's bundle.

The most rapid conduction in the right atrium was found in the crista terminalis where the conduction velocity was 91.22 ± 1.7 cm/s. The conduction velocity in Bachmann's bundle was 90.79 ± 1.22 cm/s. The action potential propagated in waves in the left and right atrial appendages. The conduction velocities in some regions in the atrial appendage (as shown by arrows 4 and 6 in Figure 5.6) were faster than in the adjacent tissues.

The tipped region in Figures 5.6 and 5.7 shows the block zone where the tissue activated later than its adjacent region in the left atrium.

5.3.3 Computer simulation

In this study, computer simulations of the activation sequence of the rabbit atria were carried out under two different conditions: isotropic and anisotropic.

In the isotropic computer simulation, all the cardiac tissues (including Bachmann's bundle, crista terminalis, coronary sinus, block zone etc.) in the anatomical model had the same conduction velocity, 84 cm/s. Conduction was also set as isotropic ($R_x = R_y = R_z$). The isotropic computer simulation result is shown in Figure 5.8. The colour bar shows the activation time in milliseconds. The SAN excited first, and then the isotropic excitation propagated to other parts of the rabbit atria. It took around 26 ms for the action potential to propagate from the SAN to the whole atria.

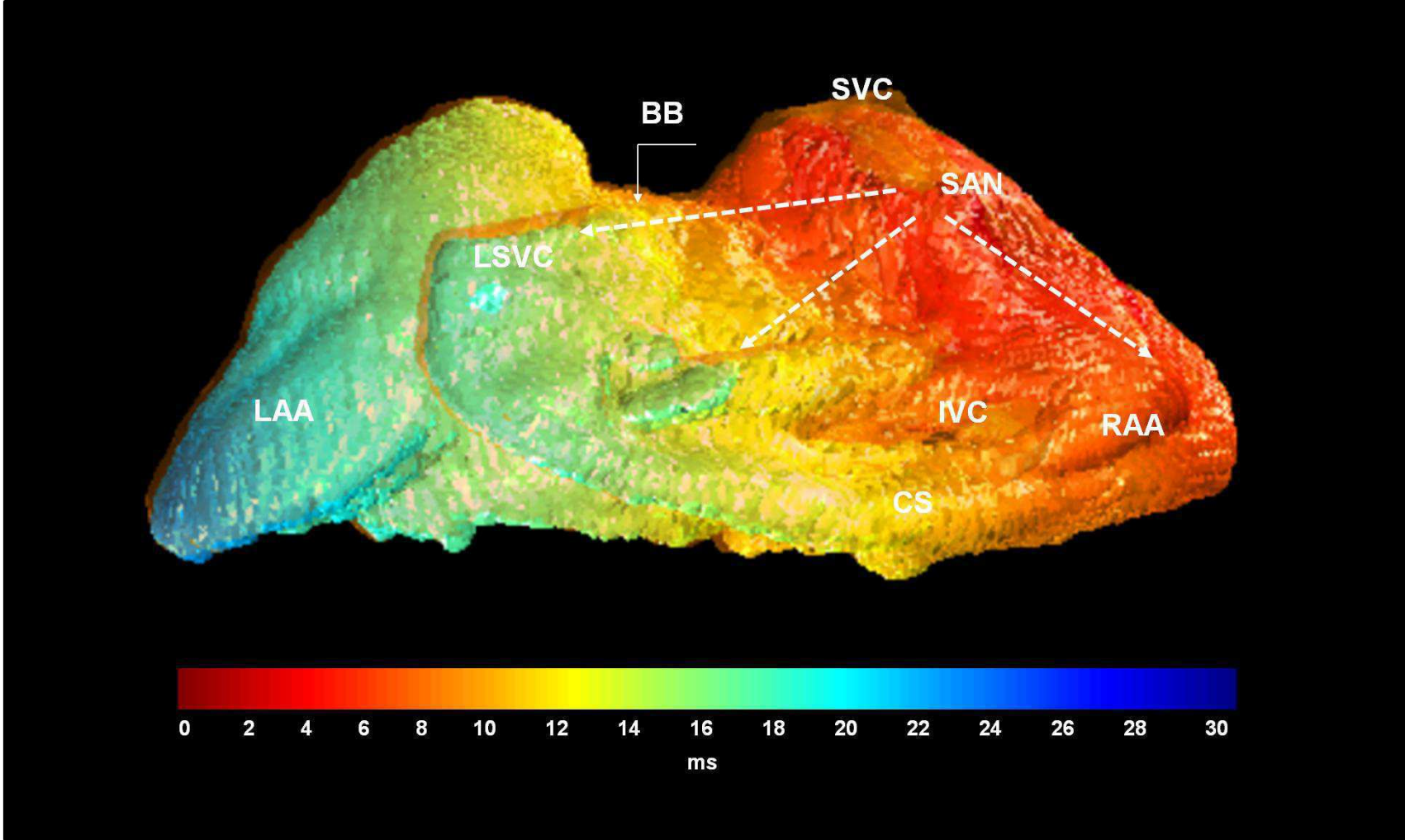


Figure 5.8 Isotropic computer simulation result obtained using the 3D rabbit atria model (together with the cellular automaton model of action potential conduction)

Dark red indicates the earliest activation and dark blue indicates the latest activation. Numbers in the colour bar indicate the activation time in milliseconds. The black dashed lines show the direction of action potential propagation. BB, Bachmann's bundle; BZ, block zone; CS, coronary sinus; CT, crista terminalis; IVC, inferior vena cava; LAA, left atrial appendage; LIPV, left inferior pulmonary vein; PV, pulmonary vein; RAA, right atrial appendage; SVC, superior vena cava.

In the anisotropic computer simulation, different components in the anatomical model were given different conduction properties according to the experimental mapping data. The conduction velocities along the axes of Bachmann's bundle and the crista terminalis were set at 90 cm/s and 91.2 cm/s, respectively. The conduction velocities in the direction transverse to the axes of the bundles were set lower than that along the axes; the ratio was set at 1:3. In accordance with the experimental mapping data, the conduction velocity in coronary sinus and left superior vena cava was set slow (60 cm/s) in the computer simulation. In other parts of the atria, the conduction velocity was set at 78 cm/s (average conduction velocity in the tissues highlighted by arrows 4, 5, 6 and 7 in Figure 5.6). The block zone was set as a tissue, which was unable to be activated.

Figure 5.9 shows the anisotropic simulation result. It took around 30 milliseconds for the action potential to propagate from the SAN to the whole atria. The conduction directions in the atria are shown by the white arrows in Figure 5.9. The block zone in the right atrium could be found in the computer simulation activation map. The bottom of the left superior vena cava and tip of the right atrial appendage were last activated.

5.4 Discussion

5.4.1 About the mapping techniques employed in this chapter

As described in Section 1.2.2, the optical mapping technique is a novel tool to

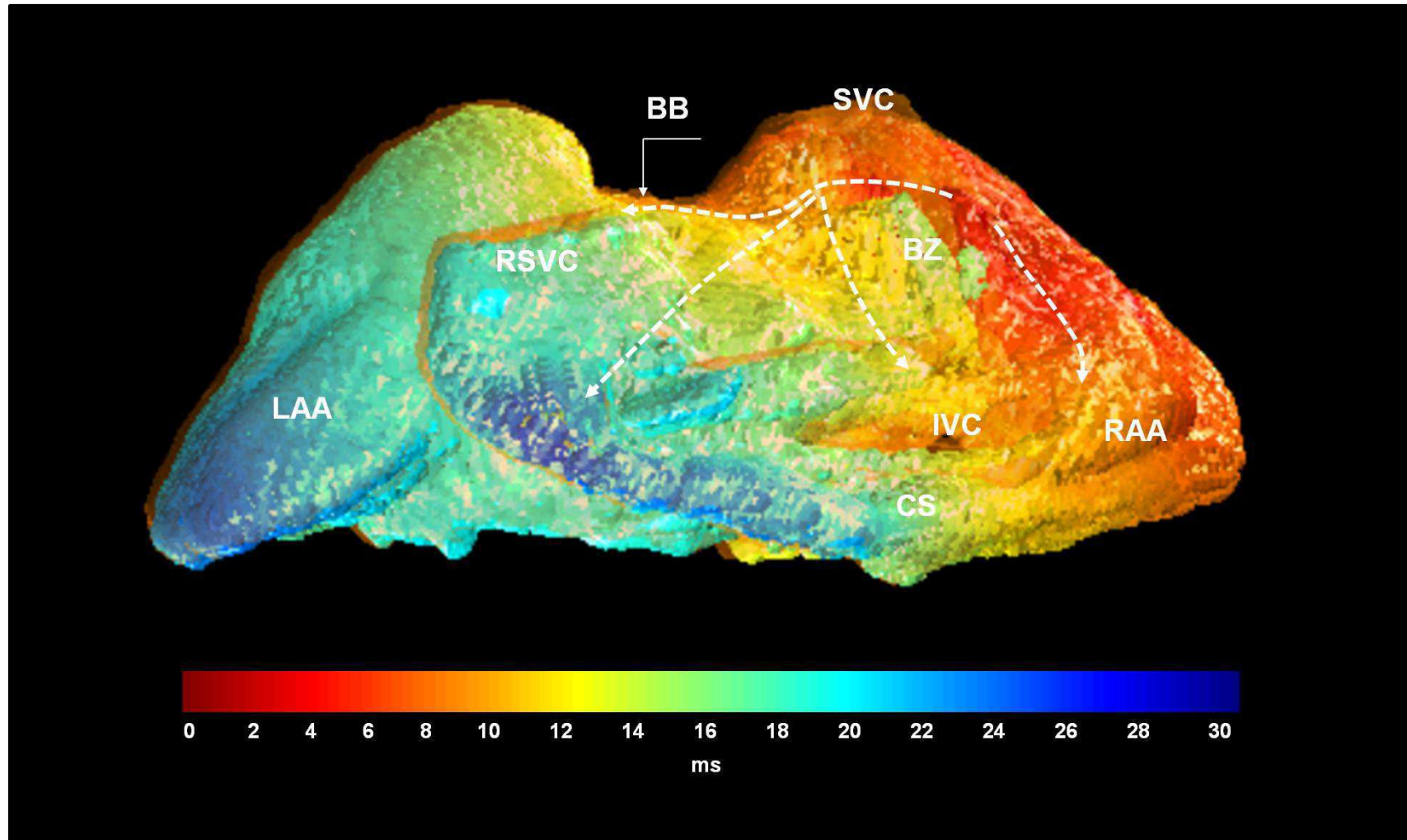


Figure 5.9 Anisotropic computer simulation result obtained using the 3D rabbit atria model (together with the cellular automaton model of action potential conduction)

Dark red indicates the earliest activation and dark blue indicates the latest activation. Numbers in the colour bar indicate the activation time in milliseconds. The black dashed lines show the direction of action potential propagation. BB, Bachmann's bundle; BZ, block zone; CS, coronary sinus; CT, crista terminalis; IVC, inferior vena cava; LAA, left atrial appendage; LIPV, left inferior pulmonary vein; PV, pulmonary vein; RAA, right atrial appendage; SVC, superior vena cava.

map the electrical activation in cardiac tissues. In this study, both optical mapping and multi-electrode mapping techniques were used to map the electrical activation sequence of the Langendorff-perfused rabbit atria. The conduction velocity in Bachmann's bundle measured by the optical mapping system was consistent with that measured by multi-electrode array mapping. However, because of a limited focal plane, the optical mapping system used in this study (Figure 1.1) was found not to be an ideal tool to map the activation sequence of the whole rabbit atria, which have a 3D structure. However, multi-electrode mapping techniques can overcome this limitation. The activation times in 12 regions of rabbit atria were mapped using 12 bipolar electrodes (Figures 5.4 and 5.5). The bipolar electrode mapping data roughly showed the activation sequence in the rabbit atria, but the conduction velocities could not be determined using these data. Using the multi-electrode array mapping system, the activation sequences in five rabbit atria were successfully mapped in detail (Figures 5.6 and 5.7) and conduction velocities in the rabbit atria were determined. As shown in Figures 5.4, 5.5, and 5.6, the activation pattern in rabbit atria mapped by the multi-electrode array mapping system was consistent with that mapped by the 12 bipolar electrodes.

5.4.2 About the electrical activation sequence of rabbit atria

In this study, experimental mapping techniques were used to map the electrical activation sequence of rabbit atria. The multi-electrode array mapping describes in detail the epicardial electrical activation sequence of rabbit atria.

The data showed, in the rabbit atria, Bachmann's bundle plays an important role in action potential propagation from the right atrium to the left atrium. This is consistent with mapping studies in human and canine hearts (Durrer et al., 1970); (Hayashi et al., 1982). Different to the human, however, the coronary sinus and the left superior vena cava in the rabbit atria does not act as an inter-atrial route for action potential propagation from the right atrium to the left atrium during sinus rhythm.

A block zone was observed between the right atrium and the atrial septum. The atrial septum only excited after the action potential propagated to Bachmann's bundle and then propagated around the top of the block zone. The border of the block zone in this study was defined as the region where the signal-to-noise ratio was below 6:1. The block zone in the heart has been found in various species including rabbit, canine and human (Boineau et al., 1988; Boyett et al., 2000; Fedorov et al., 2006), and the possible reasons for the conduction block in this region include a paucity of myocytes, poor excitability or poor electrical coupling between the cells (Boyett et al., 1999; Op't Hof et al., 1983).

The action potential propagated in a wave in the atrial appendages. The action potential propagated faster in some regions. It might be because of the presence of the pectinate muscle bundles. The propagation pattern in the atrial appendages is consistent with the activation pattern in canine and human atria (Boineau et al., 1988; Durrer et al., 1970; Hayashi et al., 1982).

Conduction velocities in different regions of the rabbit atria were measured using the multi-electrode array mapping. The data can be used to support and

validate the computer simulation work. The conduction velocity in the right atrium determined in this study was much faster than that determined by Carvalho et al. (1959). It took only around 20 ms for the action potential to propagate from the SAN to the whole right atrium, which is different from 70 ms determined by Carvalho et al. (1959). However, the conduction velocity determined in my study was consistent with that determined in the study of Fedorov et al. (2007). In the study of Carvalho et al. (1959), the rabbit right atrium was superfused in a chamber, but in my study and the study of Fedorov et al. (2007), the rabbit hearts were Langendorff-perfused. The poor perfusion condition may be why the conduction velocity measured by Carvalho et al. (1959) was slower.

5.4.3 About the computer simulation of rabbit atria

Computer simulation of the electrical activation of the rabbit atria was carried out with the cellular automaton model based on the detailed anatomical model in this study. The experimental mapping data acquired in this chapter was used to support the computer simulation. The computer simulation was carried out under two different conditions: isotropic and anisotropic. Figure 5.10 shows the comparison between the computer simulation results under the two conditions and the experimental mapping result. The activation pattern in the isotropic simulation was different to the experimental mapping result shown in Figure 5.10A. In the isotropic computer simulation, there was no block zone in the right atrium and the coronary sinus and the left superior vena cava played an important role for the action potential propagation to the left atrium.

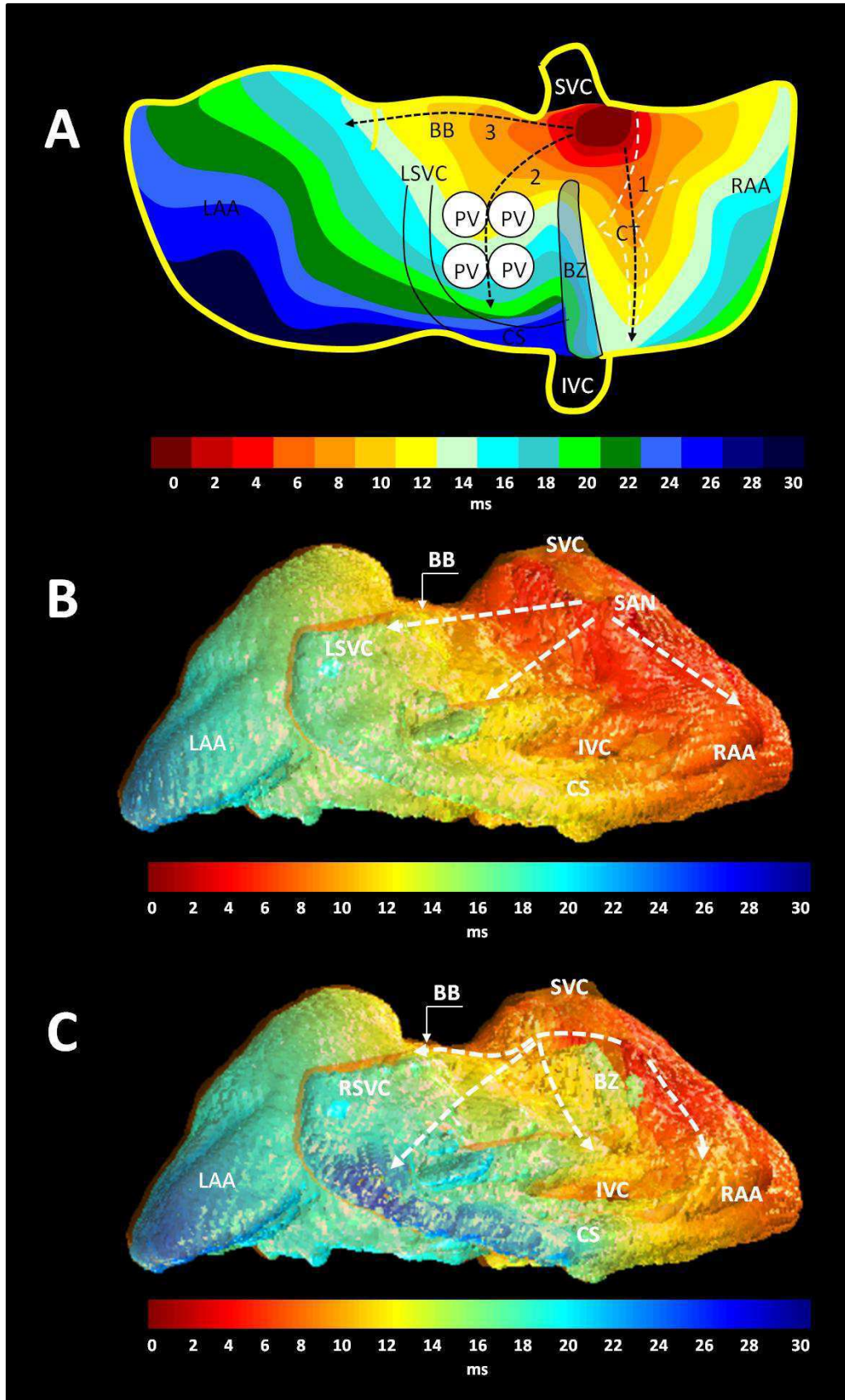


Figure 5.10 Comparison of the computer simulation results and the experimental mapping results

A, activation map of the rabbit atria drawn based on the multi-electrode array mapping. 1,2,3, indicate the conduction directions. BB, Bachmann's bundle; BZ, block zone; CS, coronary sinus; CT, crista terminalis; IVC, inferior vena cava; LAA, left atrial appendage; LIPV, left inferior pulmonary vein; PV, pulmonary vein; RAA, right atrial appendage; SVC, superior vena cava. B, activation map of the rabbit atria drawn based on the isotropic computer simulation. C, activation map of the rabbit atria drawn based on anisotropic computer simulation. Dark red indicates the earliest activation and dark blue indicates the latest activation. Numbers in the colour bar indicate activation time in milliseconds. The dashed lines show the direction of the action potential propagation.

In the anisotropic computer simulation with support from the experimental mapping data, it took around 30 ms for the action potential to propagate to the whole atria. The bottom of the left superior vena cava was the last activation region, which showed that the coronary sinus and the left superior vena cava did not provide an interatrial pathway for the propagation of the action potential. The anisotropic simulation results were consistent with the experimental data. It showed the action potential propagation in the rabbit atria during sinus rhythm can be accurately simulated, when the conduction properties of the different cardiac tissues in the detailed anatomical rabbit model were set properly. The computer simulation work in this study also showed the importance of the anatomical structure and electrophysiological heterogeneity in accurate computer simulation.

Chapter 6 Anatomical and functional investigation of the cardiac conduction system and arrhythmogenic atrioventricular ring tissues in the rat heart

6.1 Introduction

6.1.1 About atrioventricular ring tissues (AV rings)

As described in Section 1.1.5, the AV rings are anatomically continuous with the CCS (Yanni et al., 2009) and their location suggests that they could be a source of atrial tachycardia (Kistler et al., 2006). To the best of my knowledge, there is no anatomical heart model with the CCS and the AV rings.

Molecular studies carried out by my colleagues – Mr. Andrew Atkinson and Dr. Olga Fedorenko (unpublished paper, Appendix II) - showed that the expression profile of key transcription factors, ion channels, Na⁺-K⁺ pump, exchangers, Ca²⁺-handling proteins, connexins and extracellular matrix components of the adult rat AV rings is similar to that of the SAN and AVN. These data showed that the AV rings have characteristics that could result in the generation of ectopic beats and thus underlie atrial tachycardias known to originate within

the vestibules of the AV valves (Kistler et al., 2006). Both the SAN and AVN are able to generate spontaneous activity, but there is no study showing if the rat AV rings can generate spontaneous activity.

6.1.2 Aims

The first aim of this chapter was to construct a 3D anatomical model of the rat heart with the CCS and the specialised atrioventricular rings to show their location. The second aim was to study the spontaneous activity in the AV rings of the rat using multi-electrode mapping.

6.2 Materials and methods

6.2.1 Animals

Wistar Hanover rats (male; 250-300 g; provided by the University of Manchester) were used in this study.

6.2.2 MR imaging

Two rat hearts were used for MR imaging. Rats were humanely euthanized by cervical dislocation in accordance with the United Kingdom Animals (Scientific Procedures) Act, 1986. The chest was opened and the heart was removed rapidly. The heart was immobilised in formalin. Then MRI images were acquired with a 9.4 T spectrometer (Bruker BioSpin, Ettlingen, Germany) using a standard 3D FLASH sequence with an echo time of 7.9 ms, a repetition time of 50 ms, and 20 averages. Field of view was $12.8 \times 25.6 \times 12.8$ mm with

a matrix size of $128 \times 256 \times 128$, to give a voxel resolution of 0.1 mm isotropic.

6.2.3 Histological and immunohistochemical staining for 3D reconstruction

One rat heart was excised and frozen at -50°C in isopentane cooled by liquid N_2 and stored at -80°C . Then the frozen preparation was serially sectioned at 25 μm thickness in the plane of the long axis from posterior to anterior avoiding nonlinear deformation. Sections were mounted on Superfrost Plus glass slides (VWR) and stored at -80°C until use. Tissue sections were selected at 100 μm intervals for staining. Immunofluorescence experiments were carried out on the selected sections with the method described in Section 2.4. The sections were incubated in rabbit polyclonal anti HCN4 (Alomone Labs), mouse monoclonal anti Cx43 (Millipore), mouse monoclonal anti caveolin3 (BD Biosciences) and goat polyclonal anti-Cx40 (Santa Cruz Biotechnology). Primary antibodies were prepared at a concentration of 1:50 Cx43 and Cx40, 1:20 HCN4 and 1:100 caveolin-3 (Cav3) in 1% BSA overnight at 4°C . Adjacent sections were double labelled for either HCN4 and Cx43 or Cx40 and Cav3. The sections were then incubated in either Cy3 conjugated donkey anti-mouse IgG (Millipore), FITC conjugated donkey anti-rabbit IgG (Millipore) or FITC conjugated donkey anti-goat IgG (Millipore) secondary antibodies prepared at a concentration of 1:100 in 1% BSA. Sections were imaged using confocal laser scanning microscopy (LSM 5 Pascal, Carl Zeiss, NY, USA). The excitation wavelength used was 496 nm for FITC and 556 nm

for Cy3. Histology was performed on the same sections to show tissue morphology after imaging of immunohistochemical staining. Coverslips were removed and sections were washed with PBS 3 times (10 min each wash) and then Masson's trichrome staining was carried out with the method described in Section 3.2.5. The immunohistochemical and histological staining was used for the 3D reconstruction of the rat heart; the staining work in this chapter was carried out by my colleague, Dr. Olga Fedorenko.

6.2.4 3D reconstruction procedure

The procedure of 3D construction was divided into 7 steps:

- 1) MRI images and equal immunohistochemical sections at 100 μm interval were selected.
- 2) Based on the histology and the immunohistochemical staining results, the structures such as SAN, inferior nodal extension, AVN, penetrating bundle, His bundle, left bundle branch, right bundle branch, retroaortic node, left atrioventricular ring tissue, right atrioventricular ring tissue and Purkinje fibres were delineated on the immunohistochemically-stained sections. HCN4 was regarded as a positive marker for SAN, inferior nodal extension, AVN, penetrating bundle, His bundle, left bundle branch, right bundle branch, retroaortic node, left atrioventricular ring tissue, right atrioventricular ring tissue, whilst Cx43 was regarded as a positive marker for working myocardium (Chandler et al., 2011). Cx40 was regarded as a positive

marker to localise Purkinje fibres in the ventricular myocardium.

- 3) The delineated structures were superimposed on the MRI images.
- 4) The MRI images with the delineated structures were read into MATLAB to build a 3D mathematical array in the Workspace of MATLAB.
- 5) The voxel size in the mathematical array was interpolated as $100 \times 100 \times 100 \mu\text{m}$ using bicubic interpolation. The array consisted of 1,489,839 non-zero nodes.
- 6) Different structures in the array were indexed as different integer numbers in the custom developed software described in Section 3.2.8. The atrial and ventricular muscle of the heart was also segmented and indexed.
- 7) The isosurface method was used for the visualisation of the 3D anatomical model.

Figure 6.1 shows the procedure of the 3D reconstruction.

6.2.5 Preparations for electrophysiological study

Rats were humanely euthanized by cervical dislocation in accordance with the United Kingdom Animals (Scientific Procedures) Act, 1986. The chest was opened and the heart with the aortic arch was removed rapidly. The heart was cannulated with a stainless steel cannula and connected to the Langendorff perfusion system for 10 min to washout the blood remaining in the coronary

arteries and veins.

For studying the electrical activation in the right AV ring tissue, a preparation with the intact SAN and part of right AV ring tissue was made and studied. The right atrium with the atrial septum and part of the right ventricle was separated from the rest of the heart and opened by a longitudinal incision in the atrial septum to expose the endocardial surface. The preparation consisted of the intact SAN, part of the right atrium, part of the right ventricle and part of the right AV ring tissue (Figure 6.5A). After recording the extracellular potentials with a multi-electrode array, the preparation was cut along the dashed line (Figure 6.5A) to remove the SAN in order to study the isolated ring (Figure 6.5C). For the left AV ring tissue, the left atrium with part of left ventricle was separated from the rest of the heart and opened by a longitudinal incision to expose the endocardial surface. The preparation consisted of part of the left atrium, part of the left ventricle and part of the left ring (Figure 6.6A). When making the preparations, the atrioventricular nodal tissue and the atrioventricular valves were carefully removed.

The preparations were pinned to the floor of the tissue chamber described in section 1.1.7 with the endocardial surface up and superfused with oxygenated (95% O₂ and 5% CO₂) Krebs-Ringer solution via a peristaltic pump (Gilson Minipuls 3, Anachem) at 20 ml/min, 37°C and allowed to accommodate for 30 min. The bath temperature was monitored using a miniature thermistor. The composition of the perfusion solution was as follows (mM): NaCl 120.3; KCl 4.0; CaCl₂ 1.2; MgSO₄ 1.3; NaH₂PO₄ 1.2; NaHCO₃ 25.2; glucose 11.0 (pH 7.4,

equilibrated with 95% O₂/5%CO₂).

6.2.6 Multi-electrode mapping experiments on the AV rings

Mapping experiments were carried out on the right and left AV ring using the multi-electrode mapping system described in Chapter 4. For studying the electrical activation in the right AV ring, an area of 3.7×4.5 mm (black rectangle in Figure 6.5A) in the preparation with SAN and part of right AV ring (Figure 6.5A) was mapped at first with an 8×8 electrode array (0.2 mm diameter, ~ 0.6 mm interelectrode distance). After mapping, the SAN was removed (cut along the red dashed line in Figure 6.5A). Then the isolated right AV ring tissue was left to recover for 30 min in the tissue bath. Then an area of 1.5×4.5 mm (black rectangle in Figure 6.5C) in the isolated right AV ring tissue preparation was mapped with a 6×10 electrode array (described in Section 4.3.2; 0.25 mm diameter, ~ 0.2 mm interelectrode distance).

For the left ring, an area of 1.5×4.5 mm (black rectangle in Figure 6.6A) in a left AV ring tissue preparation was mapped with the same array used in the isolated right AV ring tissue preparation.

All the signals were acquired at 1.5 kHz, amplified 100 times, digitized with 16-bit resolution and stored on a hard drive for off-line analysis.

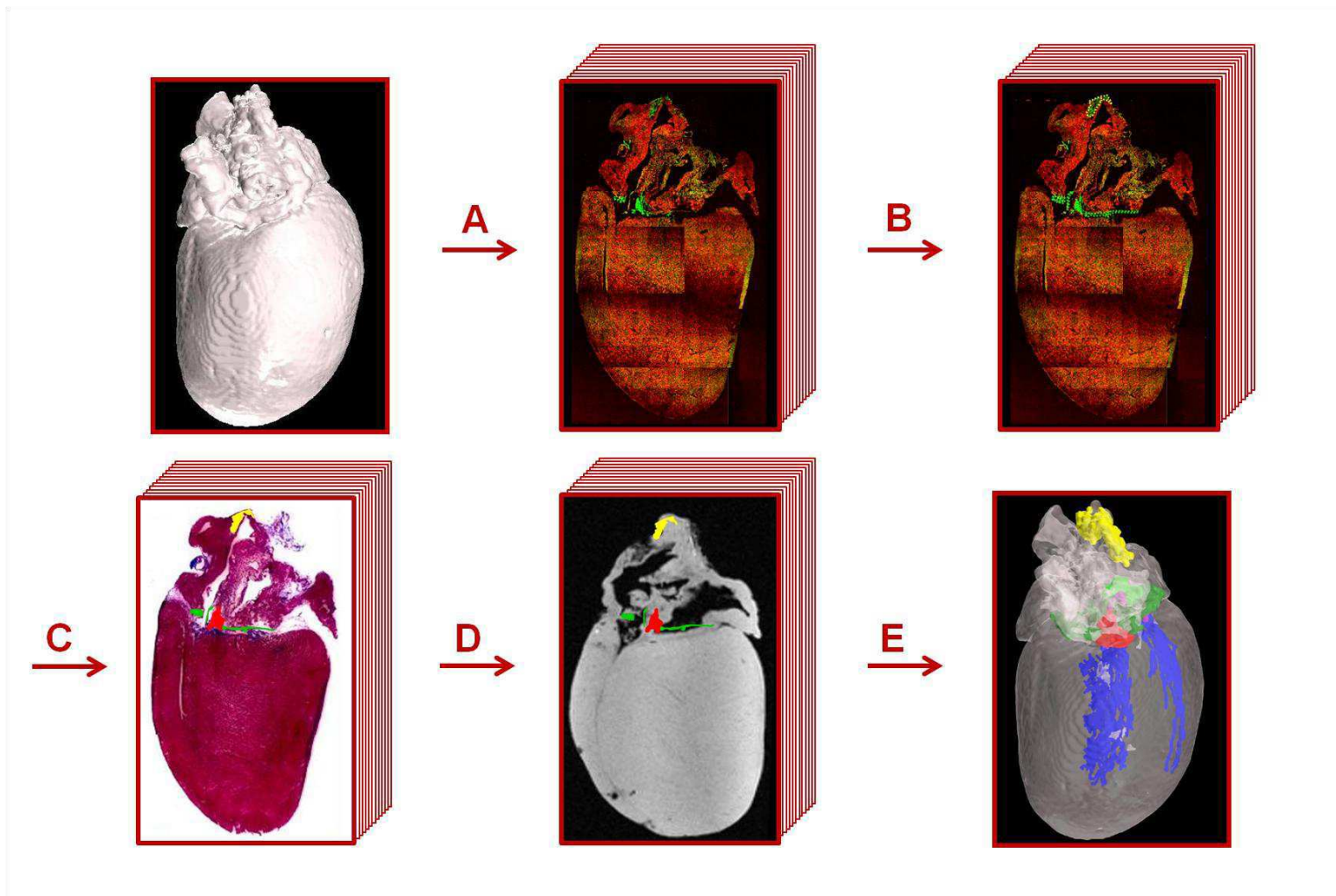


Figure 6.1 Flow diagram showing 3D reconstruction procedure

A, a whole heart was sectioned and immunolabeled. B, based on the immunolabelling, structures such as the SAN, AVN and AV rings etc. were delineated. C, the delineated structures were transferred onto the histological images. D, the delineated structures were superimposed on the corresponding MRI images. E, the MRI images with the delineated structures were imported into MATLAB and used to construct a 3D mathematical model.

6.2.7 Data analysis

The moment of maximum negative dV/dt in the extracellular electrograms was automatically found in the custom-developed software and taken as the local activation time as described in Section 4.3.4.2. Based on the local activation times, activation maps were drawn in custom-developed software in MATLAB as described in Section 4.3.4.2.

6.3 Results

6.3.1 3D reconstruction

For the 3D reconstruction, a 3D mathematical array was constructed in MATLAB. In the array: the atrium consisted of 284,094 nodes, which were indexed as 1; the ventricle consists of 1,180,021 nodes which were indexed as 2; and the SAN consists of 3,316, which were indexed as 3. The AVN and AV rings consist of 1,326 and 3,013 nodes, respectively, which were indexed as 4 and 5. The Purkinje fibres consist of 18,069 nodes, which were indexed as 6. The 3D reconstruction clearly shows the relation between the AV rings, retroaortic node and the principle parts of the CCS (Figures 6.2 - 6.4). The SAN (Figures 6.2 and 6.3, yellow) is an extensive structure found at the junction of the superior vena cava with the right atrium. Based on immunofluorescence, no evidence was found for any discrete specialised connections within the atrial walls between the SAN and the AVN. The AVN (Figures 6.2 - 6.4, red), lies in the atrial septal component of the AV junctional

area, with a prominent tongue of HCN4-positive tissue extending from the AVN into the atrial septum.

The right and left rings, shown in dark green (Figures 6.2 - 6.4), occupy the vestibules of the tricuspid and mitral valves, respectively. They are seen as small HCN4-positive regions at the insertion of the atrial myocardium into the AV junctions. When traced within the tricuspid vestibule, the right ring is seen to be continuous with the right nodal extension. The left ring is less well defined than the right ring, being no more than a thin strip of HCN4-positive tissue within the mitral valvar vestibule at the level of the left AV junction.

The retroaortic node is situated at the base of the atrial septum superior to the penetrating portion of the AV conduction axis (Figures 6.2 - 6.4, light green). It is an extended structure, with connections to both the right and left rings. The AV rings form a figure-of-eight configuration around the tricuspid and mitral valvar orifices, with the central components occupying the base of the atrial septum. As shown in Figures 6.2 - 6.4, the right and left rings are also continuous with both right and left nodal extensions from the AVN. The AV rings then unite ventrally in the retroaortic node as they cross cranially over the penetrating portion of the AV conduction axis. The transition of the AVN into the penetrating bundle is marked by the insulation of the AV conduction axis from the atrial myocardium. The Purkinje fibres ramify within the ventral aspect of the ventricular musculature (Figures 6.2 and 6.3, blue).

6.3.2 Electrophysiological study

For studying the spontaneous activity in the right AV ring tissue, multi-extracellular electrode mapping was carried out in 19 preparations. All the preparations (Figure 6.5A) consisting of SAN, part of right atrium and right AV ring tissue were active spontaneously and regularly. A representative activation map is shown in Figure 6.5B; the earliest excitation was found in the SAN region and excitation propagated to the right atrium and right atrioventricular ring tissue. After removing the SAN, the preparation of isolated right AV ring tissue (Figure 6.5C) was still active spontaneously, but the activity was irregular. The earliest excitation sites were located in the right ring. More than one pacemaker site was found in each preparation. Red stars in Figure 6.5C show the pacemaker sites. Exit block occurred in 5 of the 19 right AV ring tissue preparations under control conditions, but after 0.05 μ M isoproterenol was applied, the exit block disappeared. Figure 6.5D shows the activation map of the tissue in control condition and after the application of isoproterenol.

Multi-extracellular electrode mapping was also carried out on 11 isolated left AV ring tissue preparations (Figure 6.6A) to study the spontaneous activity in the left AV ring tissue. All the 11 preparations were active spontaneously. Similar to the isolated right AV ring tissue preparations, the activity in the left AV ring tissue was irregular and there was more than one pacemaker site in a preparation (Figure 6.6A, red stars). Exit block occurred in 4 of the 11 left ring tissue preparations under control conditions, and the exit block was relieved

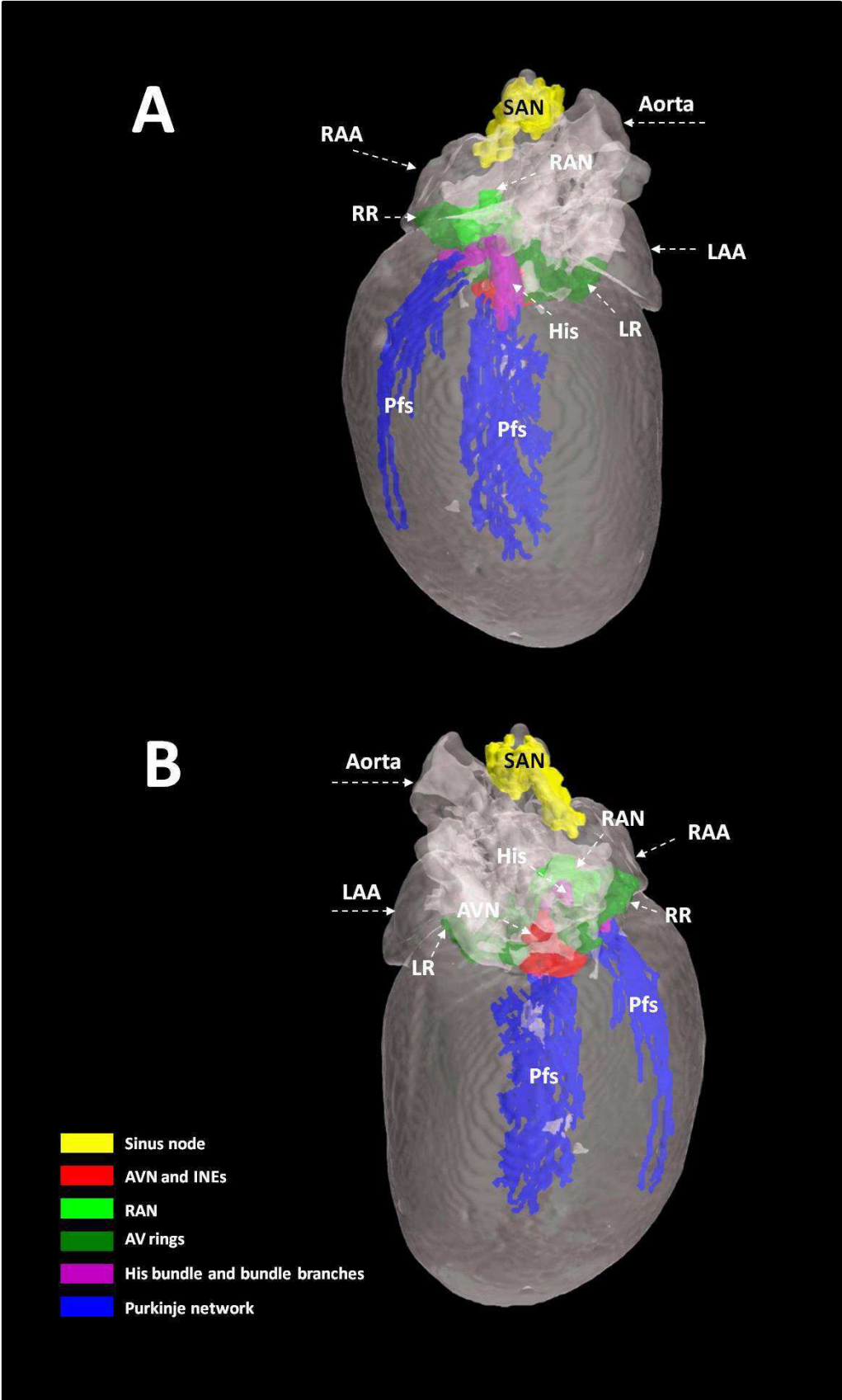


Figure 6.2 Complete transparent views of the 3D rat heart model with the CCS and the AV rings

A, dorsal view of the model. B, ventral view of the model. AVN, atrioventricular node; His, His bundle; LAA, left atrial appendage; LR, left ring tissue; Pfs, Purkinje fibres; RAA, right atrial appendage; RAN, retroaortic node; RR, right ring tissue; SAN, sinoatrial node.

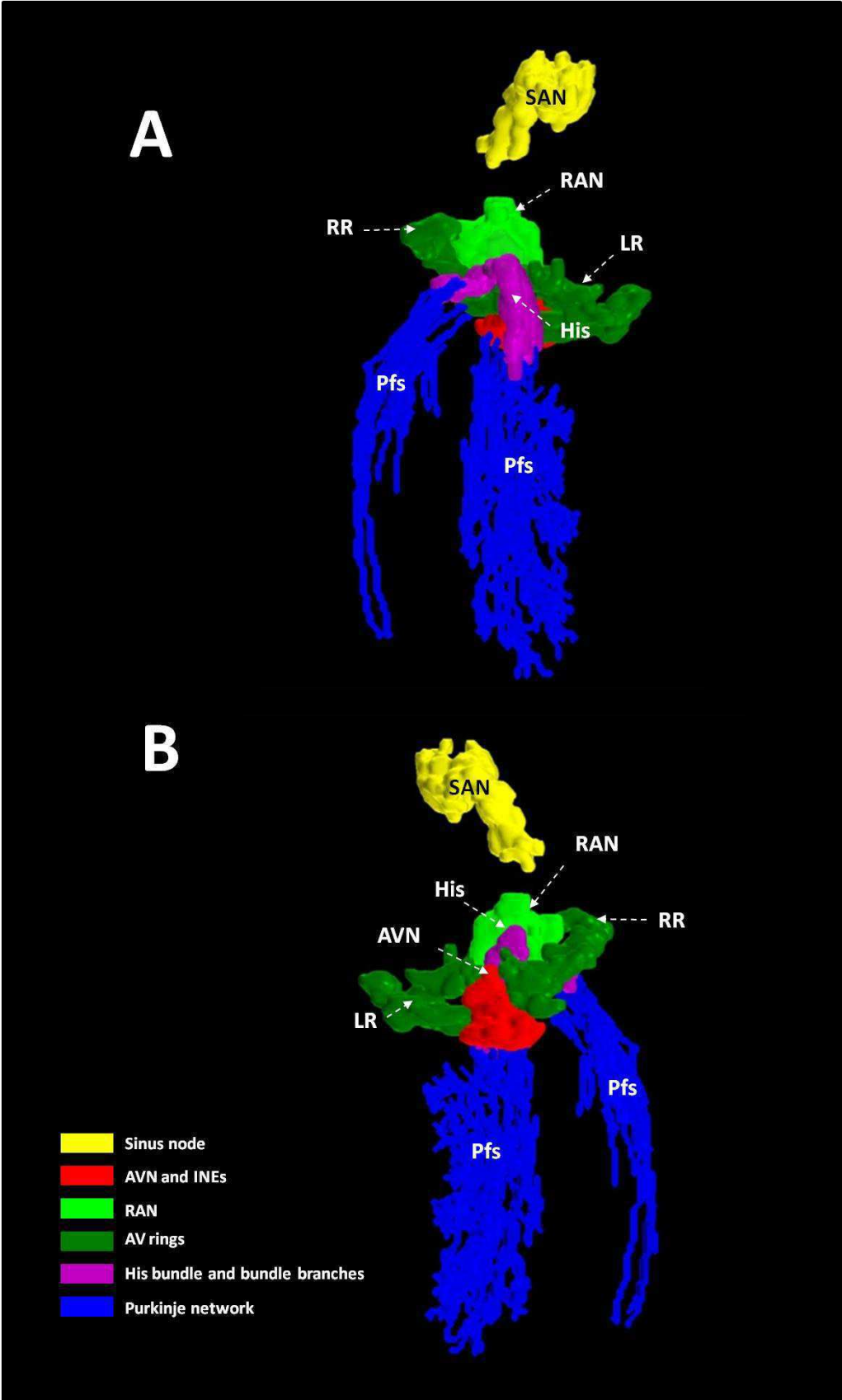


Figure 6.3 Two views of the CCS and the AV rings with myocardium removed

A, dorsal view of the model with myocardium removed. B, ventral view of the model with myocardium removed. AVN, atrioventricular node; His, His bundle; LR, left ring tissue; Pfs, Purkinje fibres; RAN, retroaortic node; RR, right ring tissue; SAN, sinoatrial node.

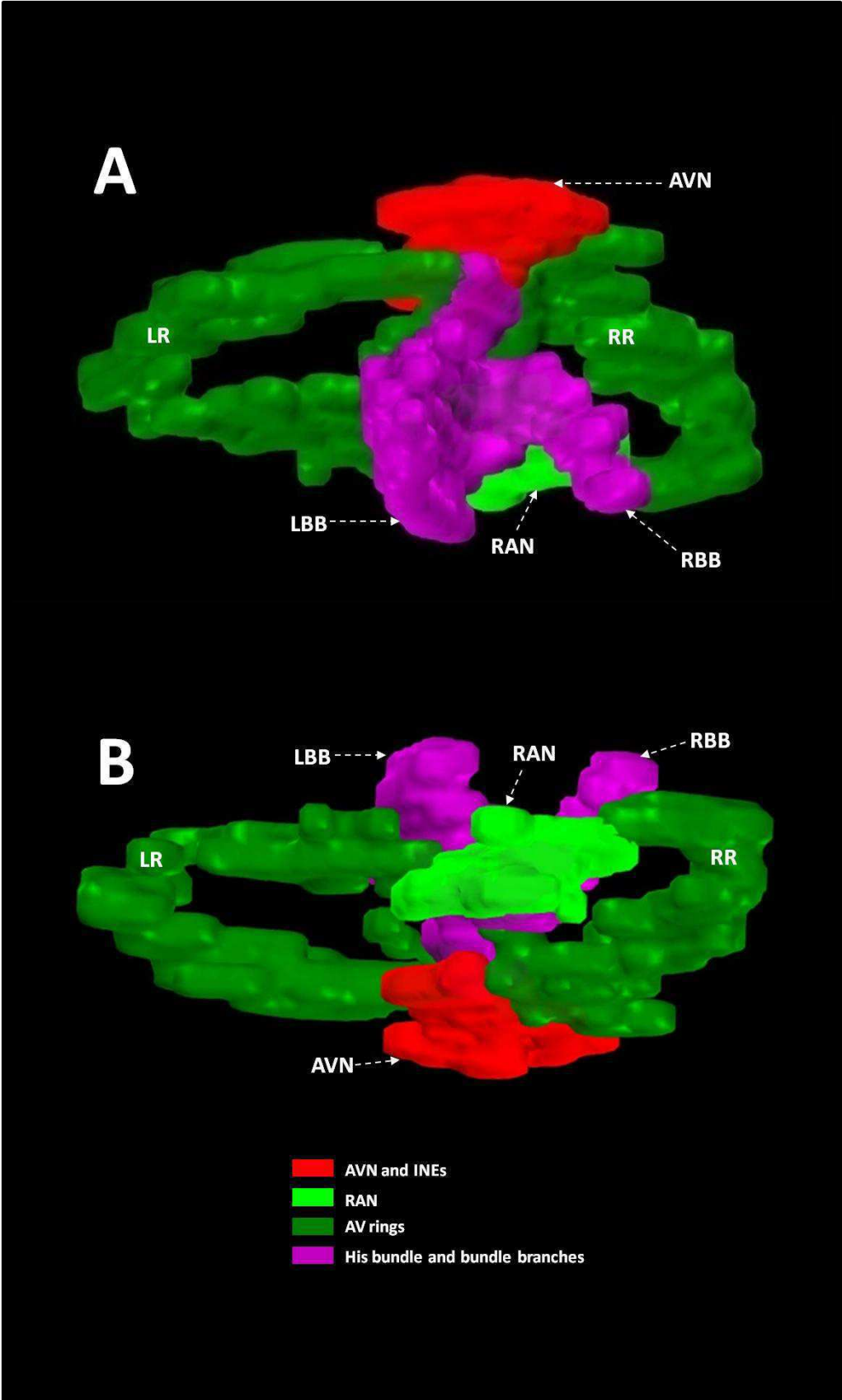


Figure 6.4 Two views showing the relationship between the atrioventricular conduction axis and the AV rings

A, top view showing the relationship between the atrioventricular conduction axis and the atrioventricular ring tissues. B, bottom view showing the relationship between the atrioventricular conduction axis and the atrioventricular ring tissue. AVN, atrioventricular node; His, His bundle; LR, left ring tissue; LBB, left His bundle branch; RAN, retroaortic node; RBB, right His bundle branch; RR, right ring tissue.

after applying 0.05 μM isoproterenol. Figure 6.6B shows the representative activation maps under control conditions and after the application of isoproterenol. In the right and left AV ring tissue preparations, the ventricular tissue was mapped as well, but there was no electrical activity was found.

6.4 Discussion

This study (i) presents the first 3D reconstruction/model of the entirety of the CCS including the AV rings and retroaortic node and (ii) demonstrates the pacemaker potentiality of the right ring. These data show that the AV rings could result in the generation of ectopic beats and thus underlie atrial tachycardias known to originate within the vestibules of the AV valves (Kistler et al., 2006).

6.4.1 3D anatomical model of the AV rings

This study represents for the first time a 3D reconstruction of the entire CCS. It shows the location, full extent and relationship of the CCS and AV rings in the adult rat heart. The components of the CCS were identifiable via their differential expression of ion channels and connexins. The 3D model (Figures 6.2 and 6.3) provides an anatomical reconstruction of the whole CCS and AV rings and, therefore, is a useful tool for teaching and research purposes.

Controversies concerning the extent and function of the cardiac conduction tissues have now raged for over 100 years. The rival notions of multiple muscular pathways for atrioventricular conduction as proposed by Kent (1893), and a solitary pathway proposed by His (1893), existed until the work of

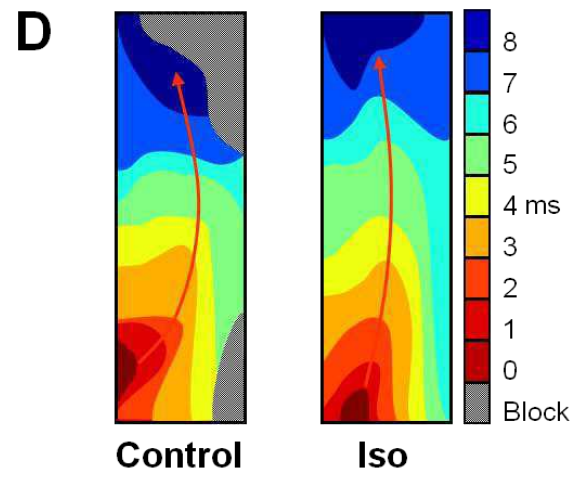
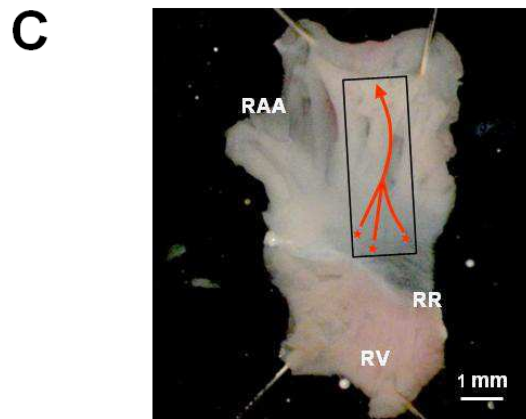
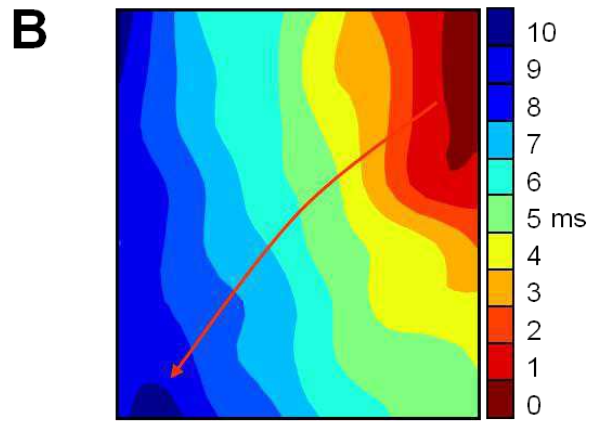
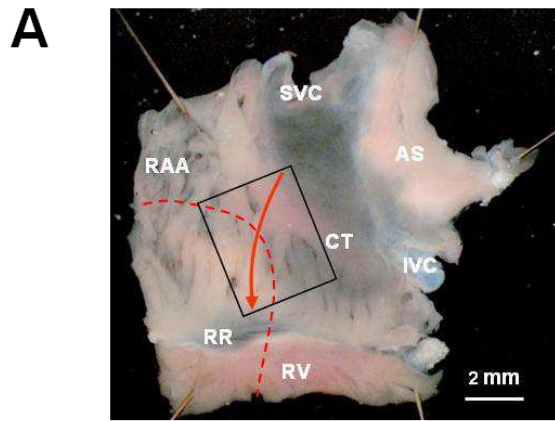


Figure 6.5 Pacemaker activities in right AV ring tissue

A, photograph of a right AV ring tissue and right atrial wall preparation. RAA, right atrial appendage; CT, crista terminalis; SVC, superior vena cava; AS, atrial septum; IVC, inferior vena cava; RV, right ventricle; TV, tricuspid valve. Rectangular box shows the position of the mapping array (8×8 electrodes) and the arrow indicates the direction of impulse propagation. Tissue was cut along the dashed line for studying isolated right AV ring tissue. B, activation map for the rectangular box in panel A, showing the leading pacemaker site (identified as the site of earliest activation) at the level of the sinus node and anterograde conduction in the right atrial free wall. C, photograph of isolated right AV ring tissue preparation. Rectangular box shows the position of the mapping array (6×10 electrodes). Stars denote the pacemaker sites in the right AV ring tissue and arrows show retrograde conduction from the three different pacemaker sites in the right AV ring tissue to the right atrium. D, activation map of the preparation in panel C under control conditions (left) and after application of $0.05 \mu\text{M}$ isoproterenol (right). CT, crista terminalis; IVC, inferior vena cava; RAA, right atrial appendage tissue; RR, right AV ring tissue; RV, right ventricular tissue; SVC, superior vena cava.

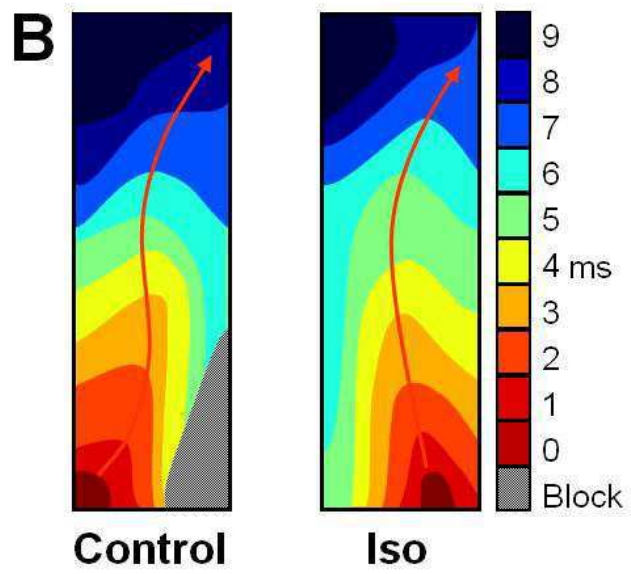
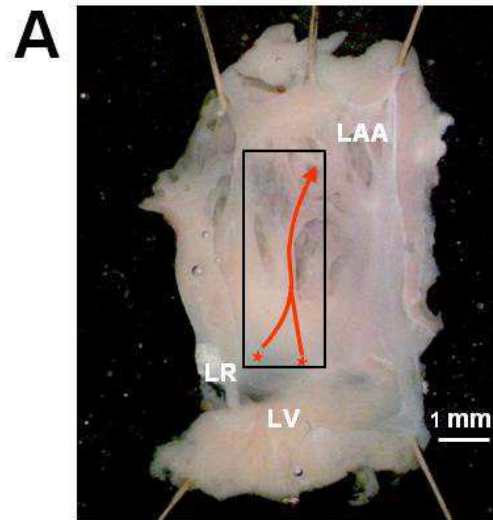


Figure 6.6 Pacemaker activities in left AV ring tissue

A, photograph of isolated left AV ring tissue preparation. Rectangular box shows the position of the mapping array (6 x 10 electrodes). Stars denote the pacemaker sites in the left AV ring tissue and arrows show retrograde conduction from the two different pacemaker sites in the left AV ring tissue to the left atrium. B, activation maps of the preparation under control conditions (left) and after application of 0.05 μ M isoproterenol (right). LAA, left atrial appendage tissue; LR, left AV ring tissue; LV, left ventricular tissue.

Tawara (Tawara, 1906) conclusively proved that there is only a solitary pathway connecting (anatomically and electrically) the atrial and ventricular muscular masses. The node like structures identified by Kent, however, do exist and have been shown to be constant features within the muscular vestibule of the tricuspid valve in structurally normal human hearts, albeit insulated from the ventricular myocardium (Anderson et al., 1974). There is little doubt that these structures, as seen in the human heart, are analogous to the more complete rings of specialised tissue identified in the hearts of rabbits, guinea-pigs, rats and mice (Anderson, 1972; Yanni et al., 2009). The morphology of the AV rings was misinterpreted in early studies, with two separate rings being shown surrounding the atrioventricular valves (Anderson, 1972; Anderson et al., 1974). This study shows that the AV rings and retroaortic node are continuous with the AV canal (Aanhaanen et al., 2010). The 3D model in this study demonstrates how the AV rings cross over the penetrating part of the AV conduction axis, forming the extensive retroaortic node recognised both histologically and immunohistochemically (Figures 6.2, 6.3 and 6.4). I presume that, initially, the retroaortic node is also in continuity with the ventral continuation of the AV conduction axis, because in the developing heart a ring is known to encircle the aortic root and return to the right atrial vestibule (Hoogaars et al., 2004; Lamers et al., 1992); I was unable to demonstrate this pathway in the current investigation. Based on its extent and its continuity with the AV rings, I also presume that the retroaortic node must have a functional role, although as yet this is unknown.

The 3D model also provides insights into the rest of the CCS. The 3D anatomical model is the first reconstruction of the sinus node in situ. The SAN is an extensive inverted U-shaped structure in the rat, endorsing the previous description of Yamamoto et al. (Yamamoto et al., 2006) and in agreement with observations in the rabbit and human (Chandler et al., 2011; Dobrzynski et al., 2005). The 3D model also shows that the bulk of the SAN lies in the region of the superior caval vein at the crest of the right atrial appendage, with a tail of nodal tissue extending down both the terminal crest and the interatrial groove, as observed in some human hearts (Yamamoto et al., 2006). The 3D model clearly shows that the SAN is far more extensive than is generally depicted in anatomical textbooks (Iaizzo, 2009).

In the developing heart, the nodal primordium is extensive and interconnected. Thus, in the mouse, as identified by marker genes such as the T-box transcription factor3 (Tbx3), a continuous tract of primary myocardium, the future nodal tissue, extends from within the confines of the systemic venous sinus, becoming continuous with the primary myocardium of the atrioventricular canal, from which will develop the AVN (Rentschler et al., 2001). This is consistent with the distribution of nodal tissue in the adult rabbit (Dobrzynski et al., 2007). The continuous tract of primary myocardium in the developing heart is suggestive of an “internodal tract”, such as that proposed by James (1963) to provide preferential conduction from the SAN to the AVN. The 3D model, however, reveals there is a gap between the SAN and the AVN in the adult heart. Moreover, use of standard histological techniques in the postnatal heart, basing the findings on the criteria proposed by Aschoff and

Monkeberg, has consistently failed to identify any insulated atrial tracts within the atrial myocardium (Janse and Anderson, 1974). It follows, therefore, that much of the primary myocardium must lose the histological features of nodal tissue as the embryo matures (Moorman et al., 2005). Furthermore, in the postnatal heart, preferential conduction from the SAN to the AVN, as well as into the left atrium, can adequately be explained on the basis of the orderly longitudinal packing of atrial myocytes in prominent muscular bundles, such as the terminal crest and Bachmann's bundle (Dobrzynski et al., 2007; James, 1963).

6.4.2 Spontaneous activity in the AV rings

Using surface electrode mapping, this study demonstrated that the AV rings are capable of pacemaking and propagating electrical activity to the atria, albeit only when the dominant pacemaking tissue of the SAN and AVN were detached (Figures 6.5 and 6.6).

The results from this study clearly show that the AV rings could potentially act as ectopic pacemakers. In patients with focal atrial tachycardia, ectopic foci are often found in the tricuspid and mitral valve annuli (Kistler et al., 2006; Morton et al., 2001). It is likely that the AV rings are responsible.

The functional role of the AV rings is still not clear and it will require further investigation to determine whether the AV ring tissues are solely a remnant from the development of the CCS or if they serve a specific function in cardiac conduction.

Chapter 7 General summary and future directions

7.1 About 3D anatomical models

7.1.1 Summary of the 3D anatomical models

As described in section 1.3, accurate computer simulation requires detailed anatomical models. In this study, three anatomical models were constructed:

- 1) A detailed 3D anatomical model of the rabbit heart: the whole of the atria and part of the ventricles) (Chapter 3).
- 2) A 3D anatomical model of the rat heart with the CCS and AV rings (Chapter 6).
- 3) A 3D anatomical model of the human AVN (Appendix I).

These anatomical models can be used in computer simulation and anatomical teaching. In Chapter 5, the 3D anatomical model of the rabbit atria was used to simulate the electrical activation sequence of the rabbit atria during sinus rhythm with the cellular automaton model. This 3D model will also be used by the group of Professor Henggui Zhang (University of Manchester) to simulate the electrical activation of the rabbit atria under normal and abnormal conditions with detailed action potential models. The 3D anatomical model of

the rat heart with the entire CCS and AV rings showed the structure of the AV rings and the location, full extent and relationship of the CCS and AV rings in the adult rat heart. It is a useful tool for teaching and can be used in computer simulation as well. The human AVN anatomical model (Appendix I) is to be used for computer simulation by Professor Henggui Zhang.

7.1.2 Future directions for the reconstruction of 3D anatomical models

The MRI technique was used in the development of the three anatomical models in this study. The voxel size of the MRI data used in the rabbit heart model, rat heart model and the human heart model was approximately 26.4 μm , 100 μm and 120 μm , respectively. Immunohistochemical and histological staining were used to distinguish the CCS in the models of the rat heart and the human heart.

Most recently, in the study of Stephenson et al. (2012), micro-CT (Henry Moseley Imaging Centre, University of Manchester) was used to scan the rat and rabbit hearts with an iodine-based contrast agent (I_2KI). The voxel size of the CT data ranged from 13 to 20 μm , which is smaller than in the MRI data sets used in this study. Interestingly, the structure of the CCS of the heart including the SAN, AVN, His bundle, the bundle branches and the Purkinje network could be directly distinguished in the CT images (Stephenson et al., 2012). Therefore, the study of Stephenson et al. (2012) showed a better way to construct 3D anatomical models of the heart in the future.

7.2 About multi-electrode mapping system

7.2.1 Summary of the multi-electrode mapping system

A multi-electrode mapping system was constructed in this study (Chapter 4). The mapping system consisted of multi-electrode electrode arrays and the data acquisition system. Four connector extensions for the data acquisition cards and two different sized 64-channel electrode arrays were constructed. Recording software and analysis software for the multi-electrode mapping system was developed in LabVIEW and MATLAB.

With this mapping system, I mapped the activation sequence in Langendorff-perfused rabbit atria (Chapter 5) and other cardiac tissues including MKK4-knockout mouse ventricles (see Figure 5 in Appendix I; Zi et al., 2011), mouse sinoatrial node preparations, rat sinoatrial node preparations, rat atrioventricular ring tissues (Chapter 6; Appendix II) and anaesthetised goat sinoatrial node (in vivo). In all these experiments, the multi-electrode mapping system performed very well.

7.2.2 Future directions for the improvement of the multi-electrode mapping system

In this study, the multi-electrode arrays were constructed manually. This was time consuming work, and the position of the electrodes was not easy to control. It will be worth to try to make the electrode array with printed circuit board (PCB) techniques. A computer could be used to control the positioning

of the electrodes when using PCB techniques. Therefore, the precision will be better than with manual control and it will be easier to make multi-electrode arrays with higher spatial resolution.

In addition to the improvement in making the arrays, the sampling rate of the mapping system can also be improved by replacing the data acquisition cards employed in the system. As described in Section 1.2, a higher sampling rate of the mapping system can provide higher temporal resolution of the activation map of the cardiac tissues. In addition, as described in Section 4.1.1.1, higher spatial resolution of the multi-electrode array also required higher sampling rates to determine the accurate activation sequence. The maximum sampling rate of the mapping system developed in this study was 1.5 kS/s when all the channels were used simultaneously. Using the multi-electrode arrays developed in this study, the maximum sampling rate of the mapping system was high enough to map the electrical activation of the cardiac tissue during sinus rhythm. However, the sampling rate of this system will not be high enough to map the electrical activation when the heart activates at a higher frequency (e.g. in atrial fibrillation). At present, there are new data acquisition cards available that can provide higher sampling rates. For example, one PXI-6255 (National Instruments) can be used to simultaneously record 80 channels at 9 kS/s. Therefore, the sampling rate of the mapping system will be increased six times if the data acquisition cards in the mapping system are replaced by the PXI-6255.

7.3 About experimental mapping and computer simulation of the electrical activation of the rabbit atria

7.3.1 Summary of the experimental mapping and computer simulation of the electrical activation of the rabbit atria

In this study, experimental mapping techniques including the optical mapping technique and the multi-electrode mapping technique were used to map the electrical activation sequence of rabbit atria (Chapter 5). The optical mapping system used in this study (Figure 1.1) was found not to be an ideal tool to map the activation sequence of the whole rabbit atria, which have a 3D structure. However, multi-electrode mapping techniques can overcome this limitation. Using the multi-electrode array mapping system, the activation sequences in five rabbit atria were successfully mapped in detail. The activation maps of the rabbit atria were drawn based on the mapping results. A block zone was observed between the right atrium and the atrial septum and was shown in the activation maps. The mapping results showed that Bachmann's bundle plays an important role in action potential propagation from the right atrium to the left atrium. However, the coronary sinus and the left superior vena cava in the rabbit atria do not act as an inter-atrial route during sinus rhythm. Conduction velocities in different regions of the rabbit atria were measured using the multi-electrode array mapping. The data can be used to support and validate

computer simulation work.

In Chapter 5, electrical activation of the rabbit atria during sinus rhythm was simulated using the cellular automaton model and the detailed 3D anatomical model constructed in Chapter 3. The experimental mapping data was used to support the computer simulation. The computer simulation work was validated by the experimental mapping data. The computer simulation work showed the importance of the anatomical structure and electrophysiological heterogeneity in accurate computer simulation.

7.3.2 Future directions for the experimental mapping and computer simulation of the electrical activation of the rabbit atria

Using the multi-electrode mapping technique, the activation of the rabbit atria was mapped from the epicardium. However, the study of Schuessler et.al. (1993) showed the epicardial and endocardial activation can be slightly different in some regions of the atria. Therefore, more information about the electrical activation of the rabbit atria can be obtained if endocardial mapping can be performed.

In addition to the experimental mapping, the computer simulation work was carried out in this study using the cellular automaton model. Compared to the full action potential model, the cellular automaton model is simpler to calculate the propagation of the action potential in the atria. However, the cellular automaton model cannot include detailed information about various kinds of

ion currents underlying the action potential. Therefore, the full action potential model is needed, if we want to simulate the effect of some ion currents on the activation of the atria under normal or abnormal condition.

7.4 About electrophysiological study on AV rings

7.4.1 Summary of electrophysiological study on AV rings

Using the multi-electrode mapping technique, this study demonstrated that the AV rings are capable of pacemaking and propagating electrical activity to the atria, albeit only when the dominant pacemaking tissue of the SAN and AVN are detached (Chapter 6). In patients with focal atrial tachycardia, ectopic foci are often found in the tricuspid and mitral valve annuli (Kistler et al., 2006; Morton et al., 2001). This study suggests that the AV rings may be responsible.

7.4.2 Future directions for the electrophysiological study on AV rings

Although the AV rings were proved to be able to generate spontaneous activity, the electrophysiological properties of the myocytes in the AV rings have not been investigated in this study. Dr. Sunil Logantha (University of Manchester) recorded the intracellular action potential from the AV rings with sharp microelectrodes (Appendix II). The intracellular action potentials recorded at the leading pacemaker site in the AV rings were sinus node-like, but the spontaneous rate was slower than that in the SAN. The mechanisms underlying

the diastolic depolarization in the AV rings have not been investigated. Further studies are needed to investigate the electrophysiological properties of the myocytes in the AV rings with the patch clamp technique.

References

Aanhaanen, W.T., Mommersteeg, M.T., Norden, J., Wakker, V., de Gier-de Vries, C., Anderson, R.H., Kispert, A., Moorman, A.F., and Christoffels, V.M. (2010). Developmental origin, growth, and three-dimensional architecture of the atrioventricular conduction axis of the mouse heart. *Circ Res* 107, 728-736.

Abed, A.A., Guo, T., Lovell, N.H., and Dokos, S. (2010). An anatomically realistic 3d model of atrial propagation based on experimentally recorded action potentials. *Conf Proc IEEE Eng Med Biol Soc* 2010, 243-246.

Akiyama, T. (2010). Sunao Tawara: discoverer of the atrioventricular conduction system of the heart. *Cardiol J* 17, 428-434.

Anderson, R.H. (1972). The disposition and innervation of atrioventricular ring specialized tissue in rats and rabbits. *J Anat* 113, 197-211.

Anderson, R.H., Becker, A.E., Arnold, R., and Wilkinson, J.L. (1974). The conducting tissues in congenitally corrected transposition. *Circulation* 50, 911-923.

Anderson, R.H., and Taylor, I.M. (1972). Development of atrioventricular specialized tissue in human heart. *Br Heart J* 34, 1205-1214.

Anderson, R.H., Yanni, J., Boyett, M.R., Chandler, N.J., and Dobrzynski, H. (2009). The anatomy of the cardiac conduction system. *Clin Anat* 22, 99-113.

Ausma, J., Dispersyn, G.D., Duimel, H., Thone, F., Ver Donck, L., Allessie, M.A., and Borgers, M. (2000). Changes in ultrastructural calcium distribution in goat atria during atrial fibrillation. In *J Mol Cell Cardiol*, pp. 355-364.

Bachmann, G. (1916). The inter-auricular time interval. *Am J Physiol*, 41:309.

Bishop, M.J., Plank, G., Burton, R.A., Schneider, J.E., Gavaghan, D.J., Grau, V., and Kohl, P. (2010). Development of an anatomically detailed MRI-derived rabbit ventricular model and assessment of its impact on simulations of electrophysiological function. *Am J Physiol Heart Circ Physiol* 298, H699-718.

Blanc, O., Virag, N., Vesin, J.M., and Kappenberger, L. (2001). A computer model of human atria with reasonable computation load and realistic anatomical properties. *IEEE Trans Biomed Eng* 48, 1229-1237.

- Boineau, J.P., Canavan, T.E., Schuessler, R.B., Cain, M.E., Corr, P.B., and Cox, J.L. (1988). Demonstration of a widely distributed atrial pacemaker complex in the human heart. *Circulation* 77, 1221-1237.
- Bordas, R., Gillow, K., Lou, Q., Efimov, I.R., Gavaghan, D., Kohl, P., Grau, V., and Rodriguez, B. (2011). Rabbit-specific ventricular model of cardiac electrophysiological function including specialized conduction system. *Prog Biophys Mol Biol* 107, 90-100.
- Boyett, M.R. (2009). 'And the beat goes on.' The cardiac conduction system: the wiring system of the heart. *Exp Physiol* 94, 1035-1049.
- Boyett, M.R., and Dobrzynski, H. (2007). The sinoatrial node is still setting the pace 100 years after its discovery. *Circ Res* 100, 1543-1545.
- Boyett, M.R., Honjo, H., and Kodama, I. (2000). The sinoatrial node, a heterogeneous pacemaker structure. *Cardiovasc Res* 47, 658-687.
- Boyett, M.R., Honjo, H., Yamamoto, M., Nikmaram, M.R., Niwa, R., and Kodama, I. (1999). Downward gradient in action potential duration along conduction path in and around the sinoatrial node. *Am J Physiol* 276, H686-698.
- Boyett, M.R., Li, J., Inada, S., Dobrzynski, H., Schneider, J.E., Holden, A.V., and Zhang, H. (2005). Imaging the heart: computer 3-dimensional anatomic models of the heart. *J Electrocardiol* 38, 113-120.
- Bub, G., Tateno, K., Shrier, A., and Glass, L. (2003). Spontaneous initiation and termination of complex rhythms in cardiac cell culture. *J Cardiovasc Electrophysiol* 14, S229-236.
- Chandler, N., Aslanidi, O., Buckley, D., Inada, S., Birchall, S., Atkinson, A., Kirk, D., Monfredi, O., Molenaar, P., Anderson, R., et al. (2011). Computer three-dimensional anatomical reconstruction of the human sinus node and a novel paranodal area. *Anat Rec (Hoboken)* 294, 970-979.
- Chauvin, M., Shah, D.C., Haissaguerre, M., Marcellin, L., and Brechenmacher, C. (2000). The anatomic basis of connections between the coronary sinus musculature and the left atrium in humans. *Circulation* 101, 647-652.
- Childers, R.W., Merideth, J., and Moe, G.K. (1968). Supernormality in Bachmann's bundle. An in vitro and in vivo study in the dog. *Circ Res* 22, 363-370.
- Christoffels, V.M., Smits, G.J., Kispert, A., and Moorman, A.F. (2010). Development of the pacemaker tissues of the heart. *Circ Res* 106, 240-254.
- Cosio, F.G., Martin-Penato, A., Pastor, A., Nunez, A., Montero, M.A., Cantale,

C.P., and Schames, S. (2004). Atrial activation mapping in sinus rhythm in the clinical electrophysiology laboratory: observations during Bachmann's bundle block. *J Cardiovasc Electrophysiol* 15, 524-531.

De Carvalho, A.P., De Mello, W.C., and Hoffman, B.F. (1959). Electrophysiological evidence for specialized fiber types in rabbit atrium. *Am J Physiol* 196, 483-488.

De Mello, W.C. (1977). Passive electrical properties of the atrio-ventricular node. *Pflugers Archiv : European journal of physiology* 371, 135-139.

Dobrzynski, H., Boyett, M.R., and Anderson, R.H. (2007). New insights into pacemaker activity: promoting understanding of sick sinus syndrome. *Circulation* 115, 1921-1932.

Dobrzynski, H., Li, J., Tellez, J., Greener, I.D., Nikolski, V.P., Wright, S.E., Parson, S.H., Jones, S.A., Lancaster, M.K., Yamamoto, M., et al. (2005). Computer three-dimensional reconstruction of the sinoatrial node. *Circulation* 111, 846-854.

Doring, H.J. (1990). The isolated perfused heart according to Langendorff technique--function--application. *Physiol Bohemoslov* 39, 481-504.

Durrer, D., van Dam, R.T., Freud, G.E., Janse, M.J., Meijler, F.L., and Arzbaecher, R.C. (1970). Total excitation of the isolated human heart. *Circulation* 41, 899-912.

Efimov, I.R., Nikolski, V.P., and Salama, G. (2004). Optical imaging of the heart. *Circ Res* 95, 21-33.

Eijsbouts, S.C., Majidi, M., van Zandvoort, M., and Allessie, M.A. (2003). Effects of acute atrial dilation on heterogeneity in conduction in the isolated rabbit heart. *J Cardiovasc Electrophysiol* 14, 269-278.

Entcheva, E., and Bien, H. (2006). Macroscopic optical mapping of excitation in cardiac cell networks with ultra-high spatiotemporal resolution. *Prog Biophys Mol Biol* 92, 232-257.

Fedorov, V.V., Hucker, W.J., Dobrzynski, H., Rosenshtraukh, L.V., and Efimov, I.R. (2006). Postganglionic nerve stimulation induces temporal inhibition of excitability in rabbit sinoatrial node. *Am J Physiol Heart Circ Physiol* 291, H612-623.

Fedorov, V.V., Lozinsky, I.T., Sosunov, E.A., Anyukhovskiy, E.P., Rosen, M.R., Balke, C.W., and Efimov, I.R. (2007). Application of blebbistatin as an excitation-contraction uncoupler for electrophysiologic study of rat and rabbit hearts. *Heart Rhythm* 4, 619-626.

Gerhardt, M., Schuster, H., and Tyson, J.J. (1990). A cellular automation model of excitable media including curvature and dispersion. *Science* 247, 1563-1566.

Harris, A.S. (1941). The spread of excitation in turtle, dog, cat and monkey ventricles. *Am J Physiol Heart Circ Physiol* 134.

Hayashi, H., Lux, R.L., Wyatt, R.F., Burgess, M.J., and Abildskov, J.A. (1982). Relation of canine atrial activation sequence to anatomic landmarks. *Am J Physiol* 242, H421-428.

Hoogaars, W.M., Engel, A., Brons, J.F., Verkerk, A.O., de Lange, F.J., Wong, L.Y., Bakker, M.L., Clout, D.E., Wakker, V., Barnett, P., et al. (2007). *Tbx3* controls the sinoatrial node gene program and imposes pacemaker function on the atria. *Genes Dev* 21, 1098-1112.

Hoogaars, W.M., Tessari, A., Moorman, A.F., de Boer, P.A., Hagoort, J., Soufan, A.T., Campione, M., and Christoffels, V.M. (2004). The transcriptional repressor *Tbx3* delineates the developing central conduction system of the heart. *Cardiovasc Res* 62, 489-499.

Iaizzo, P.A. (2009). *Handbook of Cardiac Anatomy, Physiology, and Devices*. 2nd edition. Totowa, NJ; Humana Press;

James, T.N. (1963). The Connecting Pathways between the Sinus Node and a-V Node and between the Right and the Left Atrium in the Human Heart. *Am Heart J* 66, 498-508.

Janse, M.J., and Anderson, R.H. (1974). Specialized internodal atrial pathways: fact or fiction? *Eur J Cardiol* 2, 117-136.

Kanai, A., and Salama, G. (1995). Optical mapping reveals that repolarization spreads anisotropically and is guided by fiber orientation in guinea pig hearts. *Circ Res* 77, 784-802.

Kistler, P.M., Roberts-Thomson, K.C., Haqqani, H.M., Fynn, S.P., Singarayar, S., Vohra, J.K., Morton, J.B., Sparks, P.B., and Kalman, J.M. (2006). P-wave morphology in focal atrial tachycardia: development of an algorithm to predict the anatomic site of origin. *J Am Coll Cardiol* 48, 1010-1017.

Komuro, H., Sakai, T., Hirota, A., and Kamino, K. (1986). Conduction pattern of excitation in the amphibian atrium assessed by multiple-site optical recording of action potentials. *Jpn J Physiol* 36, 123-137.

Kumagai, K., Uno, K., Khrestian, C., and Waldo, A.L. (2000). Single site radiofrequency catheter ablation of atrial fibrillation: studies guided by simultaneous multisite mapping in the canine sterile pericarditis model. *J Am Coll Cardiol* 36, 917-923.

Lamers, W.H., Wessels, A., Verbeek, F.J., Moorman, A.F., Viragh, S., Wenink, A.C., Gittenberger-de Groot, A.C., and Anderson, R.H. (1992). New findings concerning ventricular septation in the human heart. Implications for maldevelopment. *Circulation* 86, 1194-1205.

Lan, D.Z., Pollard, A.E., Knisley, S.B., and Fast, V.G. (2007). Optical mapping of $V(m)$ and $Ca(i)(2+)$ in a model of arrhythmias induced by local catecholamine application in patterned cell cultures. *Pflugers Arch* 453, 871-877.

Langendorff, O. (1895). Untersuchungen am uberlebenden Säugethierherzen. *Pflugers Arch* 61.

Lemery, R., Soucie, L., Martin, B., Tang, A.S., Green, M., and Healey, J. (2004). Human study of biatrial electrical coupling: determinants of endocardial septal activation and conduction over interatrial connections. *Circulation* 110, 2083-2089.

Lemmon, M.A., Falasca, M., Schlessinger, J., and Ferguson, K. (1997). Regulatory recruitment of signalling molecules to the cell membrane by pleckstrin homology domains. *Trends Cell Biol* 7, 237-242.

Lewis, T. (1920). The mechanism and graphic registration of the heart beat. New York: Hoeber.

Li, J. (2005). A detailed 3D model of the rabbit right atrium including the sinoatrial node, atrioventricular node, surrounding blood vessels and valves. *Computers in Cardiology*, 32:603-606.

Li, J., Greener, I.D., Inada, S., Nikolski, V.P., Yamamoto, M., Hancox, J.C., Zhang, H., Billeter, R., Efimov, I.R., Dobrzynski, H., et al. (2008). Computer three-dimensional reconstruction of the atrioventricular node. *Circ Res* 102, 975-985.

Li, T., Sperelakis, N., Teneick, R.E., and Solaro, R.J. (1985). Effects of diacetyl monoxime on cardiac excitation-contraction coupling. *J Pharmacol Exp Ther* 232, 688-695.

Lou, Q., Fedorov, V.V., Glukhov, A.V., Moazami, N., Fast, V.G., and Efimov, I.R. (2011). Transmural heterogeneity and remodeling of ventricular excitation-contraction coupling in human heart failure. *Circulation* 123, 1881-1890.

Malkin, R.A., Kramer, N., Schnitz, B., Gopalakrishnan, M., and Curry, A.L. (2005). Advances in electrical and mechanical cardiac mapping. *Physiol Meas* 26, R1-14.

Maros, T.N., Racz, L., Plugor, S., and Maros, T.G. (1983). Contributions to the

morphology of the human coronary sinus. *Anat Anz* 154, 133-144.

McGuire, M.A., de Bakker, J.M., Vermeulen, J.T., Moorman, A.F., Loh, P., Thibault, B., Vermeulen, J.L., Becker, A.E., and Janse, M.J. (1996). Atrioventricular junctional tissue. Discrepancy between histological and electrophysiological characteristics. *Circulation* 94, 571-577.

McGuire, M.A., de Bakker, J.M., Vermeulen, J.T., Opthof, T., Becker, A.E., and Janse, M.J. (1994). Origin and significance of double potentials near the atrioventricular node. Correlation of extracellular potentials, intracellular potentials, and histology. *Circulation* 89, 2351-2360.

Mejia-Alvarez, R., Manno, C., Villalba-Galea, C.A., del Valle Fernandez, L., Costa, R.R., Fill, M., Gharbi, T., and Escobar, A.L. (2003). Pulsed local-field fluorescence microscopy: a new approach for measuring cellular signals in the beating heart. *Pflugers Arch* 445, 747-758.

Mohammadi, S.A., and Hawkins, R.E. (1998). Efficient transgene regulation from a single tetracycline-controlled positive feedback regulatory system. *Gene Ther* 5, 76-84.

Moorman, A.F., Christoffels, V.M., and Anderson, R.H. (2005). Anatomic substrates for cardiac conduction. *Heart Rhythm* 2, 875-886.

Morad, M., Dillon, S., and Weiss, J. (1986). An acousto-optically steered laser scanning system for measurement of action potential spread in intact heart. *Soc Gen Physiol Ser* 40, 211-226.

Morton, J.B., Sanders, P., Das, A., Vohra, J.K., Sparks, P.B., and Kalman, J.M. (2001). Focal atrial tachycardia arising from the tricuspid annulus: electrophysiologic and electrocardiographic characteristics. *J Cardiovasc Electrophysiol* 12, 653-659.

Op't Hof, T., Bleeker, W.K., Masson-Pevet, M., Jongasma, H.J., and Bouman, L.N. (1983). Little-excitabile transitional cells in the rabbit sinoatrial node: a statistical, morphological and electrophysiological study. *Experientia* 39, 1099-1101.

Rentschler, S., Vaidya, D.M., Tamaddon, H., Degenhardt, K., Sassoon, D., Morley, G.E., Jalife, J., and Fishman, G.I. (2001). Visualization and functional characterization of the developing murine cardiac conduction system. *Development* 128, 1785-1792.

Sakai, T., Hirota, A., Momose-Sato, Y., Sato, K., and Kamino, K. (1997). Optical mapping of conduction patterns of normal and tachycardia-like excitations in the rat atrium. *Jpn J Physiol* 47, 179-188.

Schuessler, R.B., Kawamoto, T., Hand, D.E., Mitsuno, M., Bromberg, B.I.,

- Cox, J.L., and Boineau, J.P. (1993). Simultaneous epicardial and endocardial activation sequence mapping in the isolated canine right atrium. *Circulation* 88, 250-263.
- Sealy, W.C. (1994). Surgical anatomy of accessory connections of atrioventricular conduction. *Ann Thorac Surg* 57, 1675-1683.
- Seemann, G., Hoper, C., Sachse, F.B., Dossel, O., Holden, A.V., and Zhang, H. (2006). Heterogeneous three-dimensional anatomical and electrophysiological model of human atria. *Philos Transact A Math Phys Eng Sci* 364, 1465-1481.
- Sellin, L.C., and McArdle, J.J. (1994). Multiple effects of 2,3-butanedione monoxime. *Pharmacol Toxicol* 74, 305-313.
- Shannon, C.E. (1998). Communication theory of secrecy systems. 1945. *MD Comput* 15, 57-64.
- Smith, W.M. (2003). Optical and electrical mapping of cardiac activity. *Engineering in Medicine and Biology Society, 2003 Proceedings of the 25th Annual International Conference of the IEEE* 4, 3753 - 3755 Vol.3754.
- Stephenson, R.S., Boyett, M.R., Hart, G., Nikolaidou, T., Cai, X., Corno, A.F., Alphonso, N., Jeffery, N., and Jarvis, J.C. (2012). Contrast enhanced micro-computed tomography resolves the 3-dimensional morphology of the cardiac conduction system in mammalian hearts. *PLoS One* 7, e35299.
- Tawara, S. (1906). *Das Reizleitungssystem des Säugetierherzens. Eine anatomisch histologische Studie über das Atrioventrikularbündel und die Purkinjeschen Fasern.* Jena: Gustav Fischer.
- Wagner, M.L., Lazzara, R., Weiss, R.M., and Hoffman, B.F. (1966). Specialized conducting fibers in the interatrial band. *Circ Res* 18, 502-518.
- Witkowski, F.X., Plonsey, R., Penkoske, P.A., and Kavanagh, K.M. (1994). Significance of inwardly directed transmembrane current in determination of local myocardial electrical activation during ventricular fibrillation. *Circ Res* 74, 507-524.
- Yamamoto, M., Dobrzynski, H., Tellez, J., Niwa, R., Billeter, R., Honjo, H., Kodama, I., and Boyett, M.R. (2006). Extended atrial conduction system characterised by the expression of the HCN4 channel and connexin45. *Cardiovasc Res* 72, 271-281.
- Yanni, J., Boyett, M.R., Anderson, R.H., and Dobrzynski, H. (2009). The extent of the specialized atrioventricular ring tissues. *Heart Rhythm* 6, 672-680.

Publications

Full papers

- Zi M, Kimura TE, Liu W, Jin J, Higham J, Kharche S, **Hao G**, Shi Y, Shen W, Prehar S, Mironov A, Neyses L, Bierhuizen MF, Boyett MR, Zhang H, Lei M, Cartwright EJ, Wang X. Mitogen-activated protein kinase kinase 4 deficiency in cardiomyocytes causes connexin 43 reduction and couples hypertrophic signals to ventricular arrhythmogenesis. *J Biol Chem.* 2011;286:17821-17830
- Atkinson A, **Hao G**^{*}, Logantha S, Fedorenko O, Sinha A, Yanni J, Gilber S, Benson A, Henderson D, Buckley D, Anderson RH, Boyett MR, Dobrzynski H. Functional, anatomical and molecular investigation of the cardiac conduction system and arrhythmogenic atrioventricular ring tissues in the rat heart. (submitted) * Joint first author.
- **Hao G**, Li J, Dobrzynski H, Boyett MR. Imaging of the rabbit atria – from experiment to computer modelling. (in preparation)

Conference Presentation

- Hart G, Cai X, Yanni J, Jones C, Corno AF, Hutcheon R, Monfredi O, **Hao G**, Dobrzynski H, Boyett MR. Role of the cardiac conduction system in pathophysiology of congestive heart failure. *Circulation.* 2011; 124:A14754
- Hart G, Cai X, Yanni J, Jones C, Corno AF, Hutcheon R, Monfredi O, **Hao G**, Jarvis J, Dobrzynski H, Boyett MR. Mechanisms of delayed intraventricular conduction in heart failure. *Cardiac Electrophysiology Society* (November, 2011)
- Yanni J, Cai X, Yamanushi T, Tellez JO, Jones C, Hutcheon R, Monfredi O, **Hao G**, Mackiewicz U, Maczewski M, Beresewicz A, Jahraus J, Dobrzynski H, Boyett MR. Two pathways to sinoatrial node dysfunction in heart failure. *Proc Physiol Soc* 23 (2011) PC162

- Hao G, Li J, Monfredi O, Dobrzynski H, Boyett MR. A detailed three-dimensional mathematical model of the rabbit atria. Proc Physiol Soc 19 (2010) PC205
- Fedorenko O, **Hao G**, Atkinson A, Yanni J, Gilbert S, Benson A, Henderson D, Buckley D, Anderson R, Boyett MR, Dobrzynski H. The full extent of the cardiac conduction system and atrioventricular ring tissue in the rat heart - 3D anatomical model. Proc Physiol Soc 19 (2010) C55

Appendix I: Three dimensional anatomical model of the human atrioventricular node

Introduction

An anatomical model of human AVN constructed based on immunohistochemical staining is lacking. The aim of this appendix was to construct an anatomical model of the human AVN.

Method

1) Preparation

A human AVN preparation from a healthy human hearts (but unsuitable for transplantation; male; 60 years old) was obtained from the Prince Charles Hospital, Australia. This work was ethically approved by the Queensland Government and the University of Manchester. The preparation was frozen in liquid N₂ and stored at -80°C.

2) Procedure of the 3D reconstruction of the human AVN

The 3D reconstruction of the human AVN was based on CT images, histology and immunohistochemistry staining images. The procedure can be divided into eight steps:

1. The human AVN preparation was fixed in 10 % neutral buffered formalin (pH 7.4, Sigma) for 14 days. The preparation was then imaged by micro-CT with the Metris X-tek custom 320 kV bay system at the Henry Moseley Imaging Centre, University of Manchester. All scans were acquired using 1440 projections over 360° and imaging parameters were optimised for each preparation based on pilot x-ray projections to maximise contrast and resolution. Scan times were approximately 15 min. Data were viewed and analysed using Avizo. The voxel size in the CT images was 24 µm.
2. The human AVN preparation after the micro-CT scanning was frozen in liquid N₂ and stored at -80°C. Then the frozen preparation was cut using a cryostat. 25 µm sections were cut and subsequently mounted on Superfrost Plus glass slides (VWR). Then 58 sections at 0.5 mm intervals were stained with Masson's trichrome to show the histology. The Masson's trichrome staining method is described in the general methods (Section 2.2).
3. Immunohistochemistry staining was carried out on 56 sections (at the same levels as the histology) for connexin43 (Cx43) to help delineate the AVN and the working myocardium. The immunohistochemistry staining method is described in the general methods (Section 2.4). The primary antibody used was rabbit polyclonal antibody to Cx43 (Millipore), and the second antibody used was FITC conjugated donkey anti-rabbit IgG (Millipore).

4. Based on the histology and the immunohistochemical staining results, the structures such as left inferior nodal extension, right inferior nodal extension, compact node and penetrating bundle were delineated on the histological sections. The left and right inferior nodal extensions and the compact node were recognised as Cx43-negative. Figure AI.1 shows an example to delineate the left and right inferior nodal extensions on one histological section.
5. The CT dataset was re-sliced to obtain 2D images corresponding to the cryosectioned sections. The re-slicing was carried out in Avizo (Visualization Sciences Group, Inc., USA).
6. The re-sliced CT images and corresponding histological and immunohistochemical sections at 0.5 mm intervals were selected. Then delineated structures were superimposed on the CT images.
7. The CT images with the delineated structures were imported in MATLAB to build a 3D mathematical array in MATLAB. Different structures in the 3D array were indexed with different integer numbers using in previously described custom developed software (Li J et al, 2008).

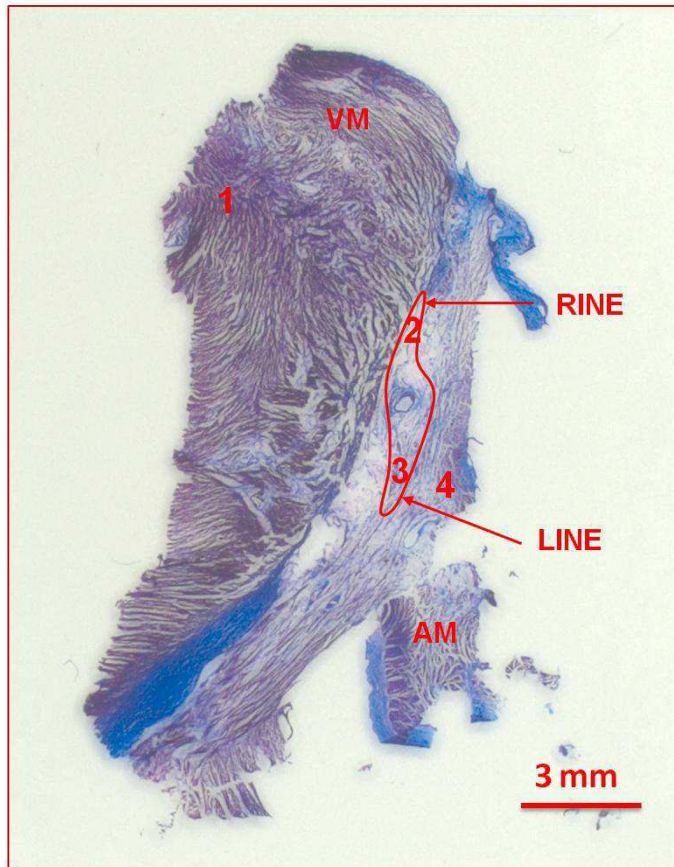
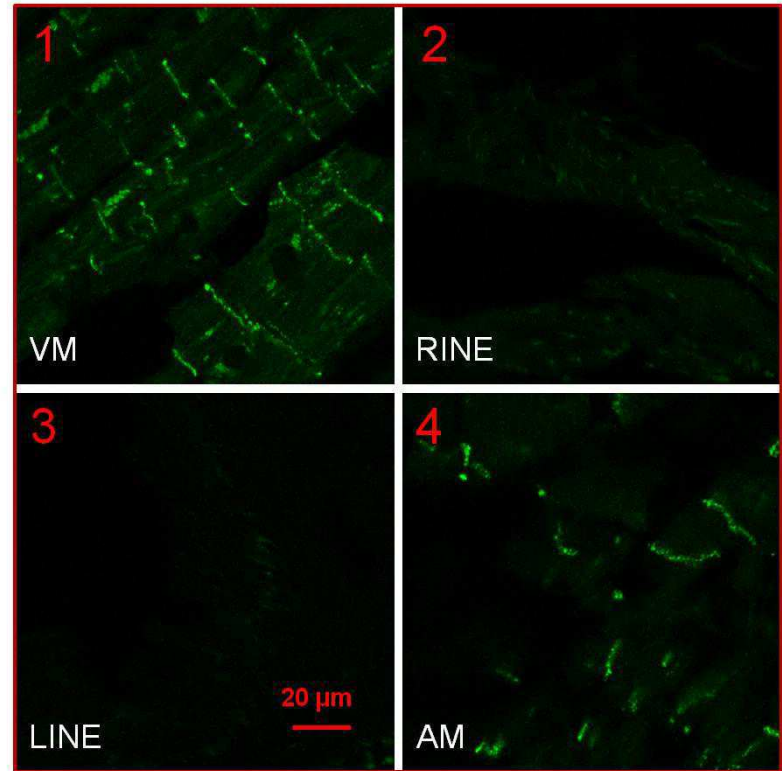
A**B**

Figure AI.1 An exempling showing delineation of the inferior nodal extension on one histological section

A, image of a histologically stained section. B, Cx43 staining on the adjacent slide Cx43 labelling was present in ventricular and atrial muscle and was absent in the left and right inferior nodal extensions. AM, atrial muscle; LINE, left inferior nodal extension; RINE, right inferior nodal extension; VM, ventricular muscle.

8. The voxel size in the mathematical array was interpolated as $0.5 \times 0.5 \times 0.5$ mm using bicubic interpolation. The array consisted of 60,213 non-zero nodes.

Results

A 3D mathematical array (Appendix IV, Array 4) for the anatomical model of the human AVN was constructed in MATLAB. The model consists of the left inferior nodal extension, right inferior nodal extension, compact node and penetrating bundle. Figure AI.2 shows 3D visualisations of the model. In the array, the left inferior nodal extension consists of 424 nodes which are indexed as 2; right inferior nodal extension consists of 2,402 nodes which are indexed as 3; compact node consists of 622 nodes which are indexed as 4; penetrating bundle consists of 451 nodes which are indexed as 5. The aorta, ventricular muscle, atrial muscle and mitral valve in the preparation are indexed as 1.

Discussion

An anatomical model of human AVN was constructed. This anatomical model is being used in computer simulations carried out by Professor Henggui Zhang (University of Manchester).

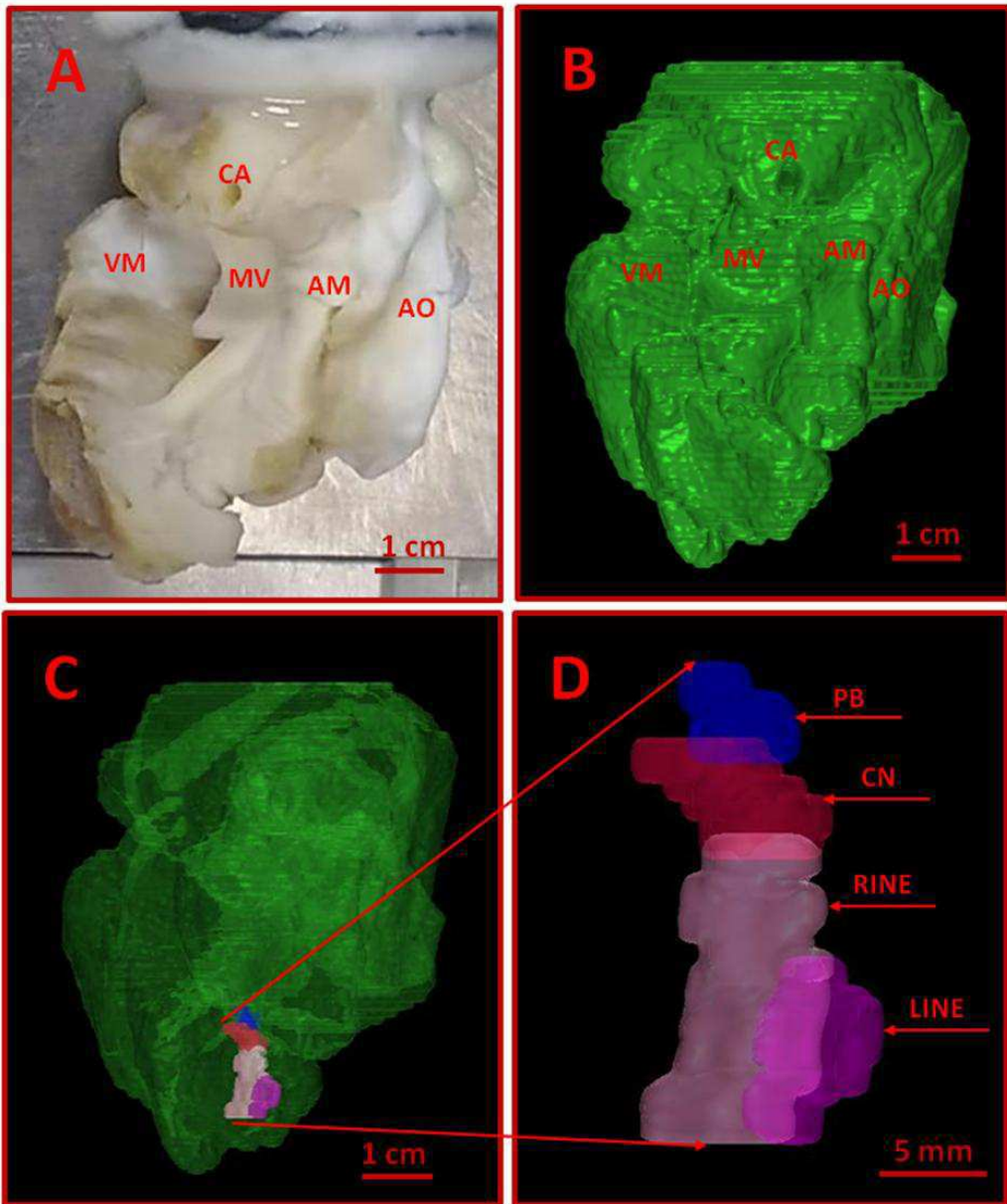


Figure AI.2 3D visualisations of the anatomical model of the human AVN

A, photo of frozen human AVN preparation. B, solid 3D visualisation of the anatomical model of the human AVN preparation. C, transparent 3D visualisation of the anatomical model of the human AVN preparation. D, 3D visualisation of the human AVN without the atrial and ventricular muscle. AO, aorta; AM, atrial muscle; CA, coronary artery; CN, compact node; LINE, left inferior nodal extension; RINE, right inferior nodal extension; MV, mitral valve; PB, penetrating bundle; VM, ventricular muscle.

**Appendix II: Functional, anatomical and
molecular investigation of the cardiac conduction
system and arrhythmogenic atrioventricular ring
tissues in the rat heart**

Functional, anatomical and molecular investigation of the cardiac conduction system and arrhythmogenic atrioventricular ring tissue in the rat heart

Short title: Cardiac conduction system and atrioventricular ring tissue

¹Andrew J. Atkinson, MSc* ; ¹Guoliang Hao, MSc* ; ¹Sunil Jit R.J. Logantha, PhD* ; ¹Olga Fedorenko, PhD* ;

¹Aditi Sinha, BSc; ¹Joseph Yanni, PhD; ⁴Stephen H. Gilbert, PhD; ²Alan P. Benson, PhD;

³Deborah J. Henderson, PhD; ²David L. Buckley, PhD; ¹Robert H. Anderson, MD; ¹Mark R. Boyett, PhD;

¹Halina Dobrzynski, PhD

*Joint first authors

¹University of Manchester; ²University of Leeds; ³University of Newcastle; ⁴Université Bordeaux Segalen

Correspondence to: Dr. H. Dobrzynski and Professor M.R. Boyett, Cardiovascular Research Group,
University of Manchester, Core Technology Facility, 46 Grafton Street, Manchester, M13 9NT, UK.

Email: halina.dobrzynski@manchester.ac.uk; mark.boyett@manchester.ac.uk

Abstract

Background-The cardiac conduction system (CCS) consists of the sinus node (SN), nodal extensions, atrioventricular (AV) node, penetrating bundle, bundle branches and Purkinje fibres. However, nodal-like AV ring tissue also exist at the AV junctions and the right and left rings unite at the retroaortic node. The study aims were to (i) construct a three-dimensional (3D) anatomical model of the AV rings and retroaortic node, (ii) map electrical activation in the right ring and study its action potential characteristics and (iii) examine gene expression in the right ring and retroaortic node.

Methods and Results-3D reconstruction (based on MRI, histology and immunohistochemistry) showed the extent and organisation of the specialised tissues, for example how the AV rings form the right and left nodal extensions into the AV node. Multi-extracellular electrode array and microelectrode mapping of isolated right ring preparations revealed robust spontaneous activity with characteristic diastolic depolarization. Using laser microdissection gene expression measured at mRNA level using qPCR and protein level using qPCR and immunohistochemistry) showed that the right ring and retroaortic node, like the SN and AV node but unlike ventricular muscle, had statistically significant higher expression of key transcription factors (including Tbx3, Msx2 and Id2) and ion channels (including HCN4, Ca_v3.1, Ca_v3.2, K_v1.5, SK1, K_{ir}3.1, K_{ir}3.4) and lower expression of other key ion channels (Na_v1.5, K_{ir}2.1).

Conclusions-The AV rings and retroaortic node possess gene expression profiles similar to that of the AV node. Ion channel expression and electrophysiological recordings show the AV rings could act as ectopic pacemakers and a source of atrial tachycardia.

Key Words: cardiac conduction system, atrioventricular ring tissues, action potential, ion channels, arrhythmogenesis

Introduction

The cardiac conduction system (CCS), generally considered to consist of the sinus node (SN) and the atrioventricular (AV) conduction axis, is responsible for the initiation and conduction of the action potential throughout the heart, leading to coordinated contraction of the heart.¹ The AV conduction axis is known to be made up of nodal extensions, AV node, penetrating or His bundle, bundle branches and Purkinje fibres. Further areas of histologically specialised tissue, distinct from these well recognised areas of the CCS, have been shown to exist within the muscular AV junctions, initially being illustrated by Kent in 1893, who incorrectly suggested that they provided multiple pathways for normal AV conduction. It was subsequently established, however, that the AV conduction axis provides the only pathway for conduction across the AV junctions in structurally normal hearts, and that the nodes identified by Kent were part of so-called AV rings, which are rings of nodal-like myocytes occupying the vestibules of the tricuspid and mitral valvar orifices and which unite in the retroaortic node.² The AV rings are also anatomically continuous with the CCS,³ although they are not thought to contribute to the normal functioning of the heart. Their location suggests that they could be a source of atrial tachycardia.⁴

For most of the preceding 100 years, the components of the CCS have been identified on the basis of the histological criteria established by Aschoff and Monckeberg. With the emergence of new techniques, it is now possible to identify transcription factors involved in the development of the CCS, these factors then serving to identify the conduction tissues. Work by Hoogaars et al.⁵ showed that the transcription factor Tbx3 is expressed in the entire CCS, including the previously described AV rings.² More recently, Aanhaanen et al.⁶ demonstrated that the AV rings are formed from the embryonic AV canal musculature, which also contributes to the retroaortic node, nodal extensions and compact AV node. AV rings have been demonstrated using immunohistochemistry in many species: human,⁷ rabbit, guinea-pig, rat³ and mouse.^{3,6} The fact that the AV rings share common developmental origins with the AV node suggests that they may have similar gene expression profiles and possess some subsidiary pacemaker functionality. HCN4, the principal ion channel responsible for the funny current (I_f), an important pacemaker current in the SN and AV node, is known to be expressed in the AV rings.³ We showed previously that the AV rings have high expression of connexin45 (Cx45) and low expression of connexin43 (Cx43), characteristics shared with the SN and AV node.^{3,8} Electrophysiological investigations have shown nodal-type action potentials in the vestibule of the tricuspid valve in pig and dog hearts.^{9,10} The functionality of the AV rings in the adult heart,

however, is unknown. The aims of this study were threefold: (i) to develop a 3D model of the anatomy of the AV rings and retroaortic node to show their extent and location; (ii) to map electrical activation in the right AV ring and study its action potential characteristics; and (iii) to examine the expression of functionally important molecules (including transcription factors, ion channels, Ca²⁺-handling proteins and gap junction channels) in the right ring.

Methods

A full description of the methods is included in the Data Supplement (DS). **3D reconstruction.** Six rat hearts were serially sectioned and the sections stained for histology and immunolabelled for CCS marker proteins. In each section, CCS tissues (including AV ring tissues) were identified and outlined and the outlines transferred to equivalent magnetic resonance images of a heart to form a 3D model of the complete CCS. **Electrophysiology.** Using a multi-extracellular electrode array and sharp microelectrodes, extracellular potentials and intracellular action potentials were recorded from right AV ring preparations from 19 rat hearts. **Quantitative PCR (qPCR).** Samples of different CCS tissues (including AV ring tissues) from 12 rat hearts were collected using laser microdissection. RNA was isolated and reverse transcribed and the abundance of 82 transcripts measured using qPCR. Significant differences were determined using a moderated (limma) t-test (significance level, $P < 0.05$) and the FDR (false discovery rate) test (significance level, $FDR < 0.2$). **Protein analysis.** Immunohistochemistry was performed on tissue sections and immunolabelling quantified.

Results

Location of AV rings and retroaortic node and relationship to CCS

By using histology and immunohistochemistry, we were able to localise all components of the CCS of the rat heart including the AV rings and retroaortic node: the SN, right and left rings, retroaortic node, nodal extensions, AV node, penetrating bundle and right and left bundle branches were HCN4-positive and Cx43-negative (Fig. 1). Immunolabelling of HCN4 and Cx43 at various levels through the heart is shown in DS Figs. 1-3. HCN4 is a positive marker for the CCS, whilst Cx43 is a positive marker for working myocardium.¹¹ Although the Purkinje fibres did not show discernible labelling of HCN4, they could be localised because they were positive for Cx40; Cx40 was not discernibly expressed in the SN, AV rings and AV node (retroaortic node not tested), whereas it was expressed in the penetrating bundle, bundle branches and Purkinje fibres (DS Figs. 3 and 4). Cx40 is a positive marker for the ventricular conduction system. The

identified components occupied the same location in all investigated hearts. MRI data for one of the hearts was used as a template onto which we mapped the location of the AV rings, retroaortic node and the remainder of the CCS (Fig. 2; DS Movie 1). The 3D reconstruction or model shows the relation between the AV rings, retroaortic node and the principal parts of the CCS. The SN (Fig. 2, yellow) is an extensive structure found at the junction of the superior caval vein with the right atrium. Based on HCN4 immunofluorescence, we found no evidence for any discrete specialised connections within the atrial walls between the SN and the AV node. The AV node (Fig. 2, red) lies in the atrial septal component of the AV junctional area, with a prominent tongue of HCN4-positive tissue extending from the AV node into the atrial septum (DS Fig. 2). The right and left rings (Fig. 2, green) occupy the vestibules of the tricuspid and mitral valves, respectively. They are seen as small HCN4-positive regions at the insertion of the atrial myocardium into the AV junctions (DS Fig. 1). When traced within the tricuspid vestibule, the right ring is seen to be continuous with the right nodal extension (DS Fig. 1). The left ring is less well defined than the right ring, being no more than a thin strip of HCN4-positive tissue within the mitral valvar vestibule at the level of the left AV junction (DS Fig. 1). The retroaortic node is situated at the base of the atrial septum superior to the penetrating portion of the AV conduction axis (Fig. 2, dark green; DS Fig. 3). It is an extended structure, with connections to both the right and left rings. Expression of HCN4, as seen by immunofluorescence, was less in the AV rings than in the SN and AV node, and less in the left ring than in the right ring. Tracing the HCN4-positive signal through the heart shows how the ring tissues form a figure-of-eight configuration around the tricuspid and mitral valvar orifices, with the central components occupying the base of the atrial septum. As shown in Fig. 2, the right and left rings are also continuous with both right and left nodal extensions from the AV node, the AV rings then uniting ventrally in the retroaortic node as they cross cranially over the penetrating portion of the AV conduction axis. The transition of the AV node into the penetrating bundle is marked by the insulation of the AV conduction axis from the atrial myocardium (DS Fig. 2). The Purkinje fibres ramify within the ventral aspect of the ventricular musculature (Fig. 2, blue; DS Figs. 3 and 4).

Action potential recording

Multi-extracellular electrode mapping in the isolated rear wall of the right atrium (Fig. 3A) revealed the site of earliest activation at the level of the SN. From here, electrical activity propagated to the rest of the right atrium and further onto the right ring. A representative activation map is shown in Fig. 3B. After

detaching the SN, all preparations showed spontaneous activation and the site of earliest activation was located in the right ring. Electrical excitation occurred at irregular intervals and activation maps revealed multiple pacemaker sites (indicated by red stars in Fig. 3C) within the right ring. In 5 out of 19 preparations, exit blocks occurred and an example is shown in Fig. 3D. Microelectrode recordings from the sites of earliest activation in isolated right ring preparations revealed spontaneous action potentials with characteristic diastolic depolarization (Fig. 3E). The frequency of spontaneous action potentials varied from 0.9 to 4.4 Hz, with a mean value of 2.1 ± 0.3 Hz ($n=4$ preparations; 13 impalements; Table 1). The upstroke of the action potential (phase 0) was slow, with a maximum upstroke velocity (dV/dt_{\max}) of 7 ± 1 V/s (Table 1). The action potential amplitude was 49 ± 3 mV and there was little or no overshoot (Table 1). The repolarization phase lacked a prominent plateau, and the duration of the action potential (at -30 mV) varied from 35 to 144 ms, with an average value of 78 ± 11 ms (Table 1). The maximum diastolic potential (MDP) reached after the action potential was -50 ± 3 mV (Table 1). The characteristics of right AV ring pacemaker action potentials are summarised in Table 1, along with corresponding measurements for action potentials recorded from the centre of the SN and the terminal crest of the right atrium.

qPCR

In the right ring and retroaortic node (as well as SN and AV node and atrial and ventricular muscle for comparison), qPCR was used to measure the expression (at mRNA level) of 82 markers, transcription factors, ion channels, Na^+ - K^+ pump, exchangers, Ca^{2+} -handling proteins, connexins, extracellular matrix components and a few miscellaneous targets. For information on the expression of all targets see DS Table 1. The expression of two atrial markers (ANP and BNP) was, as expected, high in atrial muscle and low in ventricular muscle and intermediate in the specialised tissues (DS Fig. 5). Generally, there was significantly higher expression of extracellular matrix components (e.g. collagens 1 and 3, vimentin and elastin) in the right ring and retroaortic node than in the ventricular (and in some cases atrial) muscle; the SN and AV node tended to show the same expression pattern (DS Fig. 6). This suggests that the right ring and retroaortic node contain more fibrous tissue (well known properties of SN and AV node). The expression pattern of transcription factors (responsible for tissue phenotype) and ion channels, Na^+ - K^+ pump, exchangers, Ca^{2+} -handling proteins and connexins (collectively responsible for electrical activity) are described in detail below. An overview of differences in the expression of these targets between regions is shown in Table 2.

Transcription factors

The right ring and retroaortic node (and in general SN and AV node) had significantly higher expression of Tbx3 (Fig. 4), Tbx5, Id2 and Msx2 (DS Fig. 5) than the ventricular (and in general atrial) muscle. The right ring also had significantly higher expression of Nkx2.5 and GATA4 than the ventricular muscle (DS Fig. 6); the retroaortic node had significantly higher expression of GATA6 than the ventricular muscle (DS Fig. 6). There were no significant regional differences in Msx1 expression (Table 2).

Channels carrying inward current

HCN channels are important pacemaker channels and, as expected, HCN4 was the most abundantly expressed HCN channel (Fig. 4). Expression of HCN4 was significantly higher in the right ring and retroaortic node than in the working myocardium – expression was similar to that in the AV node, but not as high as that in the SN (Fig. 4). The expression pattern of HCN1 was similar to that of HCN4, whereas HCN2 was most abundant in the ventricular muscle (Fig. 4). A minor Na⁺ channel in the heart, Na_v1.1, tended to be evenly expressed in the tissues investigated (DS Fig. 5). However, expression of the dominant Na⁺ channel, Na_v1.5 (responsible for action potential upstroke in working myocardium), tended to be lower in the right ring and retroaortic node (and in AV node, but unexpectedly not in SN) than in the working myocardium (Fig. 4). Two Na⁺ channel β subunits were differentially expressed in the right ring and retroaortic node (DS Fig. 5). Whereas there were no significant differences in expression of the major L-type Ca²⁺ channel, Ca_v1.2, between tissues, expression of two T-type Ca²⁺ channels, Ca_v3.1 and Ca_v3.2 (important for pacemaker activity), was higher in the right ring and retroaortic node (and SN and AV node) than in the ventricular muscle (Fig. 4).

K⁺ channels carrying outward current

Voltage-gated and Ca²⁺-activated K⁺ channels control action potential duration. The expression of some of these (K_v1.5, ERG, K_vβ1, SK1/K_{Ca}2.1 and SK3/K_{Ca}2.3) tended to be higher in the right ring and retroaortic node (and SN and AV node) than in the working myocardium (Fig. 4). In contrast, expression of K_v1.2, tended to be lower (Fig. 4) and others (K_v1.4, K_v2.1, K_v4.2, K_v4.3, K_vLQT1 and SK2) unchanged (DS Fig. 5; Table 2). In rat atrium, K_v1.2, K_v1.5 and K_v4.2 are reported to be functionally important channels.¹³ K_{ir}2.1 is the major inward rectifier K⁺ channel responsible for the resting potential in the working myocardium. Expression of K_{ir}2.1 was significantly lower in the right ring and retroaortic node (and SN and AV node) than in the ventricular muscle (Fig. 4). K_{ir}2.1 was more highly expressed in the ventricle than the atrium, but

the reverse was true for $K_{ir}2.2$; expression of $K_{ir}2.2$ tended to be less in the right ring and retroaortic node (and AV node) than in the atrial muscle (Fig. 4; Table 2). Expression of $K_{ir}3.1$ and $K_{ir}3.4$ (responsible for ACh-activated K^+ channel) was significantly higher in all tissues including the right ring and retroaortic node than in the ventricular muscle (Fig. 4). Twin pore K^+ channels potentially could play a role in the resting potential; interestingly, TASK2 ($K_{2p}5.1$) and TWIK2 ($K_{2p}6.1$) expression tended to be higher in the right ring and retroaortic node (and SN and AV node) than in the working myocardium (Fig. 4; DS Fig. 5).

Na^+ - K^+ pump, transporters and Ca^{2+} -handling proteins

Expression of the $\alpha 3$ isoform of the Na^+ - K^+ pump (Na^+ - K^+ ATPase $\alpha 3$), the Na^+ - H^+ exchanger (NHE1) and the Na^+ - Ca^{2+} exchanger (NCX1) was significantly higher in the right ring and retroaortic node than in the ventricular muscle (and in one case atrial muscle); the SN and AV node showed a similar expression profile (Fig. 5). Of the two ryanodine receptors (sarcoplasmic reticulum Ca^{2+} release channels), RYR2 was more highly expressed in all tissues (Fig. 5). In terms of four Ca^{2+} -handling molecules (RYR2, RYR3, SERCA2 and sarcolipin), expression in the right ring was similar to that in the SN, whereas expression in the retroaortic node was similar to that in the AV node; in the right ring (and SN), expression of RYR3, SERCA2 and sarcolipin was significantly higher than in the ventricular muscle (Fig. 5). Interestingly, sarcolipin was effectively absent from ventricular muscle (Fig. 5).

Connexins

Of the three connexins measured (Cx40, Cx43 and Cx45), Cx43 was the most abundant in all tissues (Fig. 5). There was a trend of lower expression of Cx43 in the right ring and retroaortic node (and SN and AV node) compared to the working myocardium (Fig. 5). Cx40 expression was higher in the right ring (and in SN and AV node, but not in retroaortic node) than in the working myocardium (significantly so in case of ventricular muscle; Fig. 5). Cx45 was uniformly expressed in all tissues, except for the ventricular muscle in which Cx45 expression was significantly lower (Fig. 5).

Cluster analysis and correlation

Based on the expression of 79 transcripts measured using TLDA cards, two-way hierarchical cluster analysis separated the samples into seven clusters (Fig. 6A). The samples fell into four unique sets, with the right ring, retroaortic node and AV node samples clustering together (clusters 3 and 7), the SN and atrial muscle samples clustering together (clusters 1 and 6), and the ventricular muscle samples clustering separately (clusters 2 and 5). The only exception to this pattern was the grouping of the retroaortic node with

the SN in cluster 4. Spearman rank order correlation shows that the right ring has a greater similarity to the retroaortic node and the remainder of the CCS than the working myocardium - the order of correlation for the right ring was retroaortic node>AV node>SN>atrial muscle>ventricular muscle (Fig. 6B,C). The retroaortic node also had greatest similarity to the right ring and the remainder of the CCS: AV node=right ring>SN>atrial muscle>ventricular muscle (Fig. 6C).

Protein expression

If possible (dependent on availability of suitable antibody), expression of targets was also investigated at the protein level in the right ring. For a description of all proteins investigated see DS Table 2. Expression of HCN4, Cx40 and Cx43 at the protein level has already been described (Fig. 1; DS Figs. 1-4) and is consistent with the mRNA expression (Figs. 4 and 5). Consistent with $\text{Na}_v1.5$ mRNA expression (Fig. 4), Fig. 7A shows that $\text{Na}_v1.5$ protein labelling was not found (above background fluorescence) within the right ring (and AV node) compared to the working myocardium. In the working myocardium, $\text{Na}_v1.5$ protein was expressed at the cell membrane (data not shown). Consistent with mRNA expression (Fig. 4), expression of $\text{Ca}_v3.1$ protein was observed in the right AV ring (DS Fig. 7A). High SK1 ($\text{K}_{Ca2.1}$) protein expression (at cell membrane) was observed in the penetrating bundle (Fig. 7B; DS Fig. 7G). Expression of SK1 was also observed in the right ring (Fig. 7C), whilst no expression was observed in the working myocardium (Fig. 7D; DS Fig. 7F). This is generally consistent with SK1 mRNA expression (Fig. 4). $\text{K}_{ir2.1}$ protein expression (at cell membrane) was lower in the right ring than in the ventricular muscle (Fig. 8A,B), consistent with mRNA expression (Fig. 4). There was no detectable labelling of $\text{K}_{ir3.1}$ in the right ring, whilst there was in the atrial muscle (DS Fig. 7D,E). In contrast, $\text{K}_{ir3.4}$ protein expression was observed in the right ring (at cell membrane), whilst there was weaker expression in the ventricular muscle (Fig. 8C,D). The expression pattern of $\text{K}_{ir3.1}$ and $\text{K}_{ir3.4}$ proteins is consistent with the mRNA expression (Fig. 4). Expression of RYR2 (Fig. 8E,F) and NCX1 (DS Fig. 7B,C) proteins was similar in the right ring and ventricular muscle, consistent with the mRNA expression (Fig. 5).

Discussion

This study (i) presents the first 3D reconstruction/model of the entirety of the CCS including the AV rings and retroaortic node, (ii) demonstrates the pacemaker potentiality of the right ring and (iii) shows that the expression profile of key transcription factors, ion channels, $\text{Na}^+\text{-K}^+$ pump, exchangers, Ca^{2+} -handling proteins, connexins and extracellular matrix components of the right ring and retroaortic node is similar to

that of the SN and AV node. Together these data show that the right ring and retroaortic node have characteristics that could result in the generation of ectopic beats and thus underlie atrial tachycardias known to originate within the vestibules of the AV valves.⁴

Anatomy of extended CCS

The rival notions of multiple muscular pathways for normal AV conduction, as proposed by Kent (1893), and a solitary pathway, as proposed by His (1893), existed until the work of Tawara¹⁴ conclusively proved that there was but a solitary pathway connecting (anatomically and electrically) the atrial and ventricular muscular masses. The node-like structures illustrated by Kent, however, do exist and have been shown to be constant features within the muscular vestibule of the tricuspid valve in structurally normal human hearts, albeit insulated from the ventricular myocardium.¹⁵ There is little doubt that these structures, as seen in the human heart, are analogous to the more complete rings of specialised tissue identified in the hearts of rabbits, guinea-pigs, rats and mice.^{2,3} The morphology of the AV rings was misinterpreted in early studies, with two separate rings being shown surrounding the AV valves.² Our current study (Fig. 2; DS Movie 1) shows unequivocally that the AV rings and retroaortic node are continuous with the AV conduction axis. There is strong evidence showing that the AV rings are remnants of the embryonic AV canal.⁶ Our 3D model demonstrates how the AV rings cross over the penetrating part of the AV conduction axis, forming the extensive retroaortic node recognised both histologically and immunohistochemically (Fig. 2; DS Movie 1). This ‘third’ node is anatomically discrete from the AV node³ and not continuous with it as suggested by Blom et al.¹⁶ We presume that, initially, the retroaortic node is also in continuity with the ventral continuation of the AV conduction axis, because in the developing heart a ring is known to encircle the aortic root and return to the right atrial vestibule,^{5,17} we were unable to demonstrate this pathway in the current investigation. Based on its extent and its continuity with the AV rings, we also presume that the retroaortic node must have a functional role, although as yet this is unknown.

The 3D model (Fig. 2; DS Movie 1) also provides insights into the rest of the CCS. The 3D model shows the sinus node *in situ* (Fig. 2; DS Movie 1). The SN is an extensive inverted U-shaped structure in the rat, endorsing the previous description of Yamamoto et al.⁸ and in agreement with observations in the human and rabbit.^{11,12} The 3D model shows that the bulk of the SN lies in the region of the superior caval vein at the crest of the right atrial appendage, with a tail of nodal tissue extending down both the terminal crest and the

interatrial groove, as observed in some human hearts.¹⁸ In the 3D model (Fig. 2; DS Movie 1), the SN is more extensive than is generally depicted in anatomical textbooks.¹⁹

In the developing heart, the nodal primordiums are extensive and interconnected. Thus, in the mouse, as identified by marker genes such as the transcription factor Tbx3, a continuous tract of primary myocardium, the future nodal tissue, extends from within the confines of the systemic venous sinus, becoming continuous with the primary myocardium of the AV canal, from which will develop the AV node.^{20,21} The continuous tract of primary myocardium in the developing heart is suggestive of an “internodal tract”, such as that proposed by James²² to provide preferential conduction from the SN to the AV node. The 3D model (Fig. 2; DS Movie 1), however, reveals there is a gap between the SN and the AV node in the adult heart. Moreover, use of standard histological techniques in the postnatal heart, basing the findings on the criteria proposed by Aschoff and Monkeberg, has consistently failed to identify any insulated tracts within the atrial myocardium.²³ It follows, therefore, that much of the primary myocardium must lose the histological features of nodal tissue as the embryo matures.²¹ Furthermore, in the postnatal heart, preferential conduction from the SN to the AV node, as well as into the left atrium, can adequately be explained on the basis of the orderly longitudinal packing of atrial myocytes in prominent muscular bundles, such as the terminal crest and Bachmann’s bundle.^{24,25}

Transcription factors

The establishment of the pacemaking phenotype in specific regions of the heart is achieved during the embryonic development of the heart, with expression of transcription factors being critical in enhancing or repressing the expression of certain genes during development.²⁶ Tbx3 has been shown to repress chamber (i.e. working myocardium) -specific genes such as Na_v1.5, Cx40 and Cx45.^{5,6} Our results show Tbx3 expression in the right ring and retroaortic node to be comparable to that in other components of the CCS (Fig. 4). Expression of Tbx5 and Nkx2.5 was also high in the right ring (DS Fig. 5). Nkx2.5 expression in the nodal regions is reported to be low (it is thought to act as a repressor of HCN4,²⁷ although some evidence exists for HCN4 expression in Nkx2.5 positive regions in humans).²⁸ Msx2 has been found in the AV canal, particularly in the cushions, and in close association with the CCS,²⁹ where it is thought to interact with the Tbx transcription factors to regulate connexin expression.^{29,30} Msx2 knockout mice have been shown to develop abnormal AV valves, along with the expression of chamber-specific markers in the cardiomyocytes of the AV junction.^{29,30} The finding of a high level of Msx2 in the right ring (DS Fig. 5) supports the

hypothesis that AV rings are developmentally similar to the main components of the CCS. The GATA4 and GATA6 transcription factors are known to affect the expression of genes within the heart, with GATA binding motifs identified on many genes, including NCX1.³¹ We observed high GATA4 expression in the right ring and high GATA6 expression in the retroaortic node (DS Fig. 5), although the functional consequence of these differences is unclear. Id2 is a promoter of conduction system gene expression and has been shown to have functional binding sites for Tbx5 and is cooperatively regulated by Tbx5 and Nkx2.5.^{32,33} Expression of Id2 was high in the right ring and retroaortic node as well as the SN and AV node (DS Fig. 5). The complex interactions between the transcription factors, the high degree of redundancy and multiple levels of regulation including gene expression levels and post transcriptional modification is thought to provide a mechanism ensuring tight regulation of the patterning and functioning of the CCS.³⁴ Our qPCR data shows that the right ring and retroaortic node share an expression profile of transcription factors closer to that of the CCS than the working myocardium (Table 2), again supporting the developmental evidence that the right ring and retroaortic node originate from the same primordium as the AV node.

Pacemaking in right ring

Using surface electrode mapping, we demonstrated that the right ring is capable of pacemaking and propagating electrical activity to the atria, albeit only when the dominant pacemaking tissue of the SN and AV node were detached (Fig. 3). Microelectrode recordings revealed a less negative MDP in the right ring, comparable to the MDP in the SN (Fig. 3E; Table 1). Consistent with this, we observed low mRNA and protein levels in the right ring and SN for $K_{ir}2.1$ (Figs. 4 and 8), a channel that contributes to $I_{K,1}$, which is responsible for the resting membrane potential in the working myocardium.³⁵ Expression of $K_{ir}2.2$ (another channel contributing to $I_{K,1}$) in the right ring was also relatively low (Table 2). A less negative MDP in the right ring, like in the SN, is expected to favour pacemaking. At the site of earliest activation in the right ring, action potentials showed spontaneous diastolic depolarizations, akin to that in the SN. Our results clearly support the pacemaking potentiality of the right AV ring and are consistent with the observation of action potentials with diastolic depolarizations recorded from the AV ring region of other species.^{10,36,37} Although the MDP (and dV/dt_{max} and action potential amplitude and duration) in the right ring was similar to that in the SN, the spontaneous rate in the right ring was slower (Fig. 3; Table 1). Whilst the mechanisms underlying the diastolic depolarization in the right ring are yet to be fully investigated, the expression data from this study suggests involvement of both membrane- and Ca^{2+} -clock mechanisms. HCN channels and I_f

are major determinants of the diastolic depolarization in the SN.³⁸ In the right ring and retroaortic node, we observed expression of HCN1 and HCN4 channels at mRNA and protein levels comparable to that in the AV node (Fig. 4; DS Figs. 1-3). $Ca_v3.1$ and $Ca_v3.2$ are responsible for the T-type Ca^{2+} current ($I_{Ca,T}$), which is also thought to contribute to the diastolic depolarization in the SN.³⁹ High HCN, $Ca_v3.1$ and $Ca_v3.2$ expression in the right ring and retroaortic node supports the operation of the membrane-clock pacemaking mechanism. According to the Ca^{2+} -clock mechanism of pacemaking, spontaneous Ca^{2+} release (via ryanodine receptor, RYR2) from the sarcoplasmic reticulum initiates an inward Na^+-Ca^{2+} exchanger (NCX1) current (I_{NaCa}) that contributes to the diastolic depolarization.⁴⁰ The data shows high mRNA and protein expression of RYR2 and NCX1 in the right ring and possibly retroaortic node (Figs. 5 and 8; DS Fig. 7). Thus, our data suggests that a number of mechanisms contribute to pacemaking in the right ring and this is not unlike pacemaking in the SN. $Na_v1.5$ is responsible for the large and fast Na^+ current, I_{Na} , which in turn is responsible for the action potential upstroke in working myocardium. Because of the absence of $Na_v1.5$ in nodal tissues (Figs. 4 and 7A), $Ca_v1.2$ (and $Ca_v1.3$) and the smaller and slower L-type Ca^{2+} current, $I_{Ca,L}$, is responsible for the action potential upstroke in nodal tissues.⁴¹ This is the reason why dV/dt_{max} is high in the working myocardium and low in nodal tissues (Table 1). In the right ring, dV/dt_{max} was ~ 7 V/s, comparable to that in the SN (~ 12 V/s), as opposed to 180 V/s in the right atrium (Table 1). This is likely to be the result of the lack of $Na_v1.5$ in the right ring (Figs. 4 and 7A) and it presumably indicates that $I_{Ca,L}$ is responsible for the action potential upstroke in the right AV ring. The action potential in the right ring, like that in the SN, was longer than that in the atrial muscle (Table 1). This could be the result of a decrease in expression of $K_v1.2$ in the right ring and SN (Fig. 4). There was high expression of SK1 ($K_{Ca2.1}$) (Figs. 4 and 7) in the right ring. This channel is involved in phase 3 repolarization during the action potential⁴² and has been linked to spontaneous activity and arrhythmia.^{43,44} In patients with focal atrial tachycardia, ectopic foci are often found in the tricuspid and mitral valve annuli.^{44,45} It is likely that the AV rings are responsible.

Conduction velocity and connexin expression

Connexin expression determines the degree of electrical coupling of myocytes, which in turn is an important determinant of the conduction velocity of the action potential. The lowest expression of the principal connexin, Cx43 (large conductance connexin), at the mRNA level, was found in the right ring, retroaortic node and AV node (Fig. 5). Fig. 1 and DS Figs. 1-3 show that there was no discernible labelling of Cx43 protein in the AV rings and retroaortic node as well as the SN and AV node. It is well known that

the conduction velocity of the SN and AV node is low and this suggests that the conduction velocity of the AV rings is also low and this may be important for arrhythmogenesis. In the rabbit, de Carvalho et al.³⁶ reported a low conduction velocity in the expected location of the right ring. We observed high Cx45 (small conductance connexin) expression in the right ring (and retroaortic node, SN and AV node; Fig. 5), which is consistent with the findings of Coppen et al.⁴⁶ who demonstrated the presence of Cx45 expression at the AV junction at a location that matches the anatomy of the AV rings.

Similarities and differences between AV rings, retroaortic node and AV node

We have shown that, anatomically, the AV rings, retroaortic node and AV node form a continuous structure surrounding the AV valvar orifices. It is known that, developmentally, the ring tissues are derived from the AV canal, implying that they would possess some of the same functionality as the AV nodes.⁶ In our study, out of the 82 transcripts studied using qPCR, we observed no significant differences between the right ring and retroaortic node, 10 significant differences between the right ring and the AV node, and three significant differences between the retroaortic node and the AV node (Table 2), suggesting that the different tissues have similar profiles of expression of the genes investigated, albeit with some differences between the right ring/retroaortic node and the AV node, which presumably could be critical in preventing the ring tissues from acting as primary pacemakers under normal conditions. In general, the gene expression profile of the right ring and retroaortic node is that of a pacemaker tissue and it is likely that both tissues could act as ectopic pacemakers.

Disclosures

None.

Acknowledgements

This study was supported by the British Heart Foundation.

References

- 1) Anderson RH, Yanni J, Boyett MR, Chandler NJ, Dobrzynski H. The anatomy of the cardiac conduction system. *Clin Anat.* 2009; 22:99-113.
- 2) Anderson RH. The disposition and innervation of atrioventricular ring specialized tissue in rats and rabbits. *Journal of Anatomy.* 1972; 113:197-211.
- 3) Yanni J, Boyett MR, Anderson RH, Dobrzynski H. The extent of the specialized atrioventricular ring tissues. *Heart Rhythm.* 2009; 6:672-680.
- 4) Kistler PM, Roberts-Thomson KC, Haqqani HM, Fynn SP, Singarayar S, Vohra JK, Morton JB, Sparks PB, Kalman JM. P-wave morphology in focal atrial tachycardia: development of an algorithm to predict the anatomic site of origin. *J Am Coll Cardiol.* 2006; 48:1010-7.
- 5) Hoogaars WM, Tessari A, Moorman AF, de Boer PA, Hagoort J, Soufan AT, Campione M, Christoffels VM. The transcriptional repressor Tbx3 delineates the developing central conduction system of the heart. *Cardiovasc Res.* 2004; 62:489-99.
- 6) Aanhaanen WT, Mommersteeg MT, Norden J, Wakker V, de Gier-de Vries C, Anderson RH, Kispert A, Moorman AF, Christoffels VM. Developmental origin, growth, and three-dimensional architecture of the atrioventricular conduction axis of the mouse heart. *Circ Res.* 2010; 107:728-36.
- 7) Anderson RH, Taylor IM. Development of atrioventricular specialized tissue in human heart. *Br Heart J.* 1972; 34:1205-14.
- 8) Yamamoto M, Dobrzynski H, Tellez J, Niwa R, Billeter R, Honjo H, Kodama I, Boyett MR. Extended atrial conduction system characterised by the expression of the HCN4 channel and connexin45. *Cardiovasc Res.* 2006; 72:271-81.
- 9) McGuire MA, de Bakker JM, Vermeulen JT, Opthof T, Becker AE, Janse MJ. Origin and significance of double potentials near the atrioventricular node. Correlation of extracellular potentials, intracellular potentials, and histology. *Circulation.* 1994; 89:2351-60
- 10) McGuire MA, de Bakker JM, Vermeulen JT, Moorman AF, Loh P, Thibault B, Vermeulen JL, Becker AE, Janse MJ. Atrioventricular junctional tissue. Discrepancy between histological and electrophysiological characteristics. *Circulation.* 1996; 94:571-577.
- 11) Chandler N, Aslanidi O, Buckley D, Inada S, Birchall S, Atkinson A, Kirk D, Monfredi O, Molenaar P, Anderson R, Sharma V, Sigg D, Zhang H, Boyett M, Dobrzynski H. Computer three-dimensional

- anatomical reconstruction of the human sinus node and a novel paranodal area. *Anat Rec (Hoboken)*. 2011; 294:970-9.
- 12) Dobrzynski H, Li J, Tellez J, Greener ID, Nikolski VP, Wright SE, Parson SH, Jones SA, Lancaster MK, Yamamoto M, Honjo H, Takagishi Y, Kodama I, Efimov IR, Billeter R, Boyett MR. Computer three-dimensional reconstruction of the sinoatrial node. *Circulation*. 2005; 111:846–854.
 - 13) Bou-Abboud E, Nerbonne JM. Molecular correlates of the calcium-independent, depolarization-activated K^+ currents in rat atrial myocytes. *J Physiol*. 1999; 517:407-420.
 - 14) Tawara S. Das Reizleitungssystem des Säugetierherzens. Eine anatomisch histologische Studie über das Atrioventrikularbündel und die Purkinjeschen Fäden. 1906; Jena: Gustav Fischer.
 - 15) Anderson RH, Becker AE, Arnold R, Wilkinson JL. The conduction tissues in congenitally corrected transposition. *Circulation*. 1974; 50:911–923.
 - 16) Blom NA, Gittenberger-de Groot AC, DeRuiter MC, Poelmann RE, Mentink MM, Ottenkamp J. Development of the cardiac conduction tissue in human embryos using HNK-1 antigen expression: possible relevance for understanding of abnormal atrial automaticity. *Circulation*. 1999; 99:800-6.
 - 17) Lamers WH, Wessels A, Verbeek FJ, Moorman AF, Virágh S, Wenink AC, Gittenberger-de Groot AC, Anderson RH. New findings concerning ventricular septation in the human heart. Implication for maldevelopment. *Circulation*. 1992; 86:1194 –1205.
 - 18) Anderson RH, Ho SY. The architecture of the sinus node, the atrioventricular conduction axis, and the internodal atrial myocardium. *J Cardiovasc Electrophysiol*. 1998; 9:1233-48.
 - 19) Iaizzo PA, editor. Handbook of Cardiac Anatomy, Physiology, and Devices. 2nd edition. Totowa, NJ: Humana Press; 2009.
 - 20) Rentschler S, Vaidya DM, Tamaddon H, Degenhardt K, Sassoon D, Morley GE, Jalife J, Fishman GI. Visualization and functional characterization of the developing murine cardiac conduction system. *Development*. 2001; 128:1785–1792.
 - 21) Moorman AF, Christoffels VM, Anderson RH. Anatomic substrates for cardiac conduction. *Heart Rhythm*. 2005; 2:875-86.
 - 22) James TN. The connecting pathways between the sinus node and A-V node and between the right and the left atrium in the human heart. *Am Heart J*. 1963; 66:498 –508.

- 23) Janse MJ, Anderson RH. Specialized internodal atrial pathways: fact or fiction? *Eur J Cardiol.* 1974; 2:117–136.
- 24) Spach MS, Kootsey JM. The nature of electrical propagation in cardiac muscle. *Am J Physiol.* 1983 ; 244:H3-22.
- 25) Dobrzynski H, Boyett MR, Anderson RH. New insights into pacemaker activity. Promoting understanding of sick sinus syndrome. *Circulation.* 2007; 115:1921-1932.
- 26) Hatcher CJ, Basson CT. Specification of the cardiac conduction system by transcription factors. *Circ Res.* 2009; 105:620-30.
- 27) Mommersteeg MT, Hoogaars WM, Prall OW, de Gier-de Vries C, Wiese C, Clout DE, Papaioannou VE, Brown NA, Harvey RP, Moorman AF, Christoffels VM. Molecular pathway for the localized formation of the sinoatrial node. *Circ Res.* 2007; 100:354-62.
- 28) Sizarov A, Devalla HD, Anderson RH, Passier R, Christoffels VM, Moorman AF. Molecular analysis of patterning of conduction tissues in the developing human heart. *Circ Arrhythm Electrophysiol.* 2011; 4:532-42.
- 29) Boogerd CJ, Moorman AF, Barnett P. Expression of muscle segment homeobox genes in the developing myocardium. *Anat Rec (Hoboken).* 2010; 293:998-1001.
- 30) Boogerd CJ, Moorman AF, Barnett P. Protein interactions at the heart of cardiac chamber formation. *Ann Anat.* 2009; 191:505-17.
- 31) Pikkarainen S, Tokola H, Kerkelä R, Ruskoaho H. GATA transcription factors in the developing and adult heart. *Cardiovasc Res.* 2004; 63:196-207.
- 32) Lim JY, Kim WH, Kim J, Park SI. Induction of Id2 expression by cardiac transcription factors GATA4 and Nkx2.5. *J Cell Biochem.* 2008; 103:182-94.
- 33) Moskowitz IP, Kim JB, Moore ML, Wolf CM, Peterson MA, Shendure J, Nobrega MA, Yokota Y, Berul C, Izumo S, Seidman JG, Seidman CE. A molecular pathway including Id2, Tbx5, and Nkx2-5 required for cardiac conduction system development. *Cell.* 2007; 129:1365-76.
- 34) Brewer A, Pizzey J. GATA factors in vertebrate heart development and disease. *Expert Rev Mol Med.* 2006; 8:1-20.
- 35) Noma A, Nakayama T, Kurachi Y, Irisawa H. Resting K⁺ conductances in pacemaker and non-pacemaker heart cells of the rabbit. *Jpn J Physiol.* 1984; 34:245-54.

- 36) deCarvalho AP, deMello WC, Hoffman BF. Electrophysiological evidence for specialized fiber types in rabbit atrium. *Am J Physiol.* 1959; 196:483-8.
- 37) Rozanski GJ, Jalife J. Automaticity in atrioventricular valve leaflets of rabbit heart. *Am J Physiol.* 1986; 250:H397-H406.
- 38) DiFrancesco D, Ducouret P, Robinson RB. Muscarinic modulation of cardiac rate at low acetylcholine concentrations. *Science.* 1989; 243:669-71.
- 39) Mangoni ME, Couette B, Bourinet E, Platzer J, Reimer D, Striessnig J, Nargeot J. Functional role of L-type Cav1.3 Ca²⁺ channels in cardiac pacemaker activity. *Proc Natl Acad Sci U S A.* 2003; 100:5543-8.
- 40) Lakatta EG, Maltsev VA, Vinogradova TM. A coupled SYSTEM of intracellular Ca²⁺ clocks and surface membrane voltage clocks controls the timekeeping mechanism of the heart's pacemaker. *Circ Res.* 2010; 106:659-73.
- 41) Schram G, Pourrier M, Melnyk P, Nattel S. Differential distribution of cardiac ion channel expression as a basis for regional specialization in electrical function. *Circ Res.* 2002; 90:939-50.
- 42) Xu Y, Tuteja D, Zhang Z, Xu D, Zhang Y, Rodriguez J, Nie L, Tuxson HR, Young JN, Glatzer KA, Vázquez AE, Yamoah EN, Chiamvimonvat N. Molecular identification and functional roles of a Ca²⁺-activated K⁺ channel in human and mouse hearts. *J Biol Chem.* 2003; 278:49085-94.
- 43) Zhang Q, Timofeyev V, Lu L, Li N, Singapuri A, Long MK, Bond CT, Adelman JP, Chiamvimonvat N. Functional roles of a Ca²⁺-activated K⁺ channel in atrioventricular nodes. *Circ Res.* 2008; 102:465-71.
- 44) Diness JG, Sørensen US, Nissen JD, Al-Shahib B, Jespersen T, Grønnet M, Hansen RS. Inhibition of small-conductance Ca²⁺-activated K⁺ channels terminates and protects against atrial fibrillation. *Circ Arrhythm Electrophysiol.* 2010; 3:380-90.
- 45) Morton JB, Sanders P, Das A, Vohra JK, Sparks PB, Kalman JM. Focal atrial tachycardia arising from the tricuspid annulus: electrophysiologic and electrocardiographic characteristics. *J Cardiovasc Electrophysiol.* 2001; 12:653-9.
- 46) Coppin SR, Severs NJ, Gourdie RG. Connexin45 (alpha 6) expression delineates an extended conduction system in the embryonic and mature rodent heart. *Dev Genet.* 1999; 24:82-90.

Figure legends

Fig. 1. Immunohistochemical detection of AV rings and retroaortic node (and also principal tissues making up CCS). A and B, long axis tissue sections immunolabelled for HCN4 (green signal) and Cx43 (red signal). Sections taken at level of AV node (A) and penetrating bundle (B). C, high magnification image of HCN4 labelling in right ring. Abbreviations in this and other figures: AM, atrial muscle; AVN, atrioventricular node; IVS, interventricular septum; His, penetrating or His bundle; LBB, left bundle branch; RAN, retroaortic node; RR, right ring; SN, sinus node; VM, ventricular muscle.

Fig. 2. 3D model of extended CCS. A, 3D model of heart (with opaque myocardium) viewed from dorsal surface. B, 3D model of heart (with transparent myocardium) viewed from dorsal surface. C, 3D model of extended CCS only (myocardium removed) viewed from dorsal surface. D, 3D model of heart (with transparent myocardium) viewed from ventral surface. E, 3D model of extended CCS only (myocardium removed) viewed from ventral surface. F and G, top (F) and bottom (G) views of 3D model of AV rings, retroaortic node and AV conduction axis.

Fig. 3. Pacemaker activity in right ring. A, preparation of rear wall of right atrium containing SN, right ring and AV node. Box shows position of mapping array (8x8 extracellular electrodes) and arrow shows direction of action potential conduction from SN to rest of preparation. To isolate right ring (as shown in C), tissue was cut along dashed line. B, activation map of area in A, showing leading pacemaker site (identified as site of earliest activation) in SN and anterograde conduction in right atrial free wall. Colours correspond to activation times shown in colour bar. C, preparation containing right ring only. Box shows position of mapping array (6x10 extracellular electrodes). Stars denote pacemaker sites in right ring and arrows show retrograde conduction from three different pacemaker sites to remainder of right atrium. D, activation map of area in C. E, typical intracellular action potentials recorded from pacemaker site in right ring and SN. Additional abbreviations: AS, atrial septum; CT, crista terminalis; IVC, inferior vena cava; RAA, right atrial appendage; RV, right ventricle; SVC, superior vena cava.

Fig. 4. Relative abundance of mRNA for Tbx3 and ion channels underlying cardiac action potential. Means of $2^{-\Delta Ct}$ (+SEM) shown (AM, n=4; VM, n=4; SN, n=5; AVN, n=4; RAN, n=5; RR, n=4). a-f, significant difference ($P<0.05$, FDR<0.2) from corresponding bar.

Fig. 5. Relative abundance of mRNA for Na⁺-K⁺ pump, exchangers, Ca²⁺-handling proteins and connexins. Same format as Fig. 4.

Fig. 6. Hierarchical clustering. A, two-way hierarchical cluster analysis applied to 79 genes and to samples of right ring (n=4), retroaortic node (n=5), SN (n=5), AV node (n=4), atrial muscle (n=4) and ventricular muscle (n=4). B, plot of ΔCt values of all transcripts for ventricular muscle versus those for right ring and plot of ΔCt values of all transcripts for retroaortic node versus those for right ring. Line represents $y=x$. C, Spearman rank order correlation data for same samples used for cluster analysis.

Fig. 7. Expression of Na_v1.5 and SK1 proteins in AV junctional area. A, immunolabelling of Na_v1.5 (bright green signal) in right ring and AV node in AV junctional area. Long axis section. B, immunolabelling of SK1 (bright red signal) in penetrating bundle. C, high magnification image of immunolabelling of SK1 in right ring. D, high magnification image of immunolabelling of SK1 in right ventricle.

Fig. 8. Expression of K_{ir}2.1, K_{ir}3.4 and RYR2 proteins in right ring and right ventricle. High magnification images of immunolabelling (bright green signal) shown.

Table 1. Characteristics of action potentials. Frequency, maximum diastolic potential (MDP), action potential amplitude (APA), overshoot, maximum upstroke velocity (dV/dt_{\max}), time taken for 50% repolarization (T_{50}), time taken for 90% repolarization (T_{90}) and action potential duration at -30 mV (APD_{30}) in right ring (RR), SN and atrial muscle of terminal crest in right atrium (RA) are tabled. Means \pm SEM shown. Total of 13, 6 and 13 impalements were made from right ring, SN and atrial muscle, respectively, from four preparations. * P <0.05 versus atrial muscle; $^{\dagger}P$ <0.05 versus SN; $^{\ddagger}P$ <0.05 versus right ring.

	Frequency (Hz)	MDP (mV)	APA (mV)	Overshoot (mV)	dV/dt (mV/ms)	T_{50} (ms)	T_{90} (ms)	APD_{30} (ms)
RR (n=4)	2.1 \pm 0.3 *†	-50 \pm 2.5 *	48.8 \pm 2.9 *	-1.21 \pm 0.6 *	7 \pm 0.7 *	45.9 \pm 4.8 *	86.8 \pm 7.5 *	78.4 \pm 11.3 *
SN (n=4)	4.5 \pm 0.2 ‡	-46.4 \pm 2.9 *	49.3 \pm 4.3 *	2.9 \pm 2.7 *	12.8 \pm 4.6 *	47.4 \pm 2.7 *	74.8 \pm 3.6 *	74.5 \pm 3 *
RA (n=4)	4.7 \pm 0.1 ‡	-78.1 \pm 0.8 †‡	94.3 \pm 2 †‡	16.2 \pm 2.4 †‡	180 \pm 21.1 †‡	13.3 \pm 1.2 †‡	45.2 \pm 3.4 †‡	13.2 \pm 0.8 †‡

Table 2. Comparison of expression of transcription factors, ion channels, Na⁺-K⁺ pump, exchangers, Ca²⁺-handling proteins and connexins between regions of interest. ↑*, significantly upregulated; ↓*, significantly downregulated; ↑, trend to upregulation; ↓, trend to downregulation; =, no difference.

Transcript	Retroaortic node versus ventricular muscle	Right AV ring versus ventricular muscle	Retroaortic node versus atrial muscle	Right AV ring versus atrial muscle	Retroaortic node versus SN	Right AV ring versus SN	Retroaortic node versus AV node	Right AV ring versus AV node	Retroaortic node versus right AV ring
Transcription factors									
Id2	↑*	↑*	=	=	=	=	=	=	=
Msx1	=	=	=	=	=	=	=	=	=
Msx2	↑*	↑*	↑*	↑*	↑*	↑*	=	=	=
Tbx3	↑*	↑*	↑*	↑*	=	=	=	=	=
Tbx5	↑*	↑*	=	=	=	=	=	↑*	=
Nkx2.5	=	↑*	=	=	=	=	=	=	=
GATA4	=	↑*	=	=	=	=	=	=	=
GATA6	↑*	=	=	=	=	=	=	=	↑
Inward current carrying ion channels									
Na _v 1.1	↑*	=	=	=	=	=	=	=	=
Na _v 1.5	=	=	↓*	↓	↓*	=	=	=	=
Na _v β1	↑*	↑*	=	=	↑	=	=	=	=
Na _v β4	↓*	=	=	=	=	=	=	=	=
Ca _v 1.2	=	=	=	=	=	=	=	=	=
Ca _v 1.3	=	=	=	=	=	=	=	↓*	=
Ca _v 3.1	↑*	↑*	=	=	=	=	=	=	=
Ca _v 3.2	↑*	↑*	=	=	=	=	=	=	=
HCN1	↑*	↑*	↑*	↑*	↓*	=	=	=	=
HCN2	↓*	↓*	=	=	=	=	=	=	=
HCN4	↑*	↑*	↑*	↑*	↓*	=	=	=	=
Outward current carrying K⁺ channels									
K _v 1.2	=	=	↓*	=	=	=	=	=	=
K _v 1.4	=	=	=	=	=	=	=	=	=
K _v 1.5	↑*	↑*	↑*	↑*	=	=	=	=	=
K _v 2.1	=	=	=	=	=	=	=	=	=
K _v 4.2	=	=	=	=	=	=	↑*	=	=
K _v 4.3	=	=	=	=	=	=	=	↑*	=
KvLQT1 (K _v 7.1)	=	=	=	=	=	=	=	=	=
ERG (K _v 11.1)	=	↑*	=	=	=	=	=	=	=
KChIP2	=	=	=	=	=	=	=	↑*	=
K _v β1	=	↑*	↑	↑*	=	=	↑*	↑*	=
SK1 (K _{Ca} 2.1)	↑*	↑*	=	↑*	=	↑	=	=	↓
SK2 (K _{Ca} 2.2)	=	=	=	=	=	=	=	=	=

Continued over page

Table 2 (continued).

Transcript	Retroaortic node versus ventricular muscle	Right AV ring versus ventricular muscle	Retroaortic node versus atrial muscle	Right AV ring versus atrial muscle	Retroaortic node versus SN	Right AV ring versus SN	Retroaortic node versus AV node	Right AV ring versus AV node	Retroaortic node versus right AV ring
Outward current carrying K⁺ channels (continued)									
SK3 (K _{Ca} 2.3)	=	↑*	↑	↑*	=	=	=	=	=
K _{ir} 2.1	↓*	↓*	=	=	=	=	=	=	=
K _{ir} 2.2	↑*	↑*	=	=	=	=	=	=	=
K _{ir} 3.1	↑*	↑*	↓*	↓*	=	=	=	=	=
K _{ir} 3.4	↑*	↑*	=	=	=	=	=	=	=
K _{ir} 6.1	=	=	=	=	=	=	=	=	=
K _{ir} 6.2	=	=	=	=	=	=	=	↑	=
SUR1	=	↑*	=	=	=	=	=	↑*	=
SUR2	↓*	=	↓*	=	=	=	=	=	=
TREK1 (K _{2P} 2.1)	=	=	=	=	=	=	=	=	=
TASK1 (K _{2P} 3.1)	=	=	↓	↓*	=	=	=	=	=
TASK2 (K _{2P} 5.1)	↑*	↑*	=	=	↑	↑	=	=	=
TWIK2 (K _{2P} 6.1)	↑*	↑*	=	=	=	=	=	=	=
Na⁺-K⁺ pump and exchangers									
Na ⁺ -K ⁺ pump α3	↑*	↑*	↑*	↑*	=	↑	=	=	=
Na ⁺ -H ⁺ exchanger	↑*	↑*	=	=	=	=	=	=	=
NCX1	↑*	↑*	=	=	=	=	↓	↓	=
Ca²⁺-handling proteins									
SERCA2a	=	↑*	=	=	=	=	=	↑	=
Phospholamban	=	=	=	=	=	=	=	=	=
Sarcoplipin	↑*	↑*	=	=	=	=	=	↑*	=
RYR2	=	=	=	=	=	=	=	=	=
RYR3	=	↑*	=	=	=	=	=	=	=
Gap junction channels									
Gja5 / Cx40	=	↑*	=	=	=	=	=	=	=
Gja1 / Cx43	=	=	↓*	↓	=	=	=	=	=
Gja7 / Cx45	↑*	↑*	=	=	=	=	=	=	=

Figure 1.

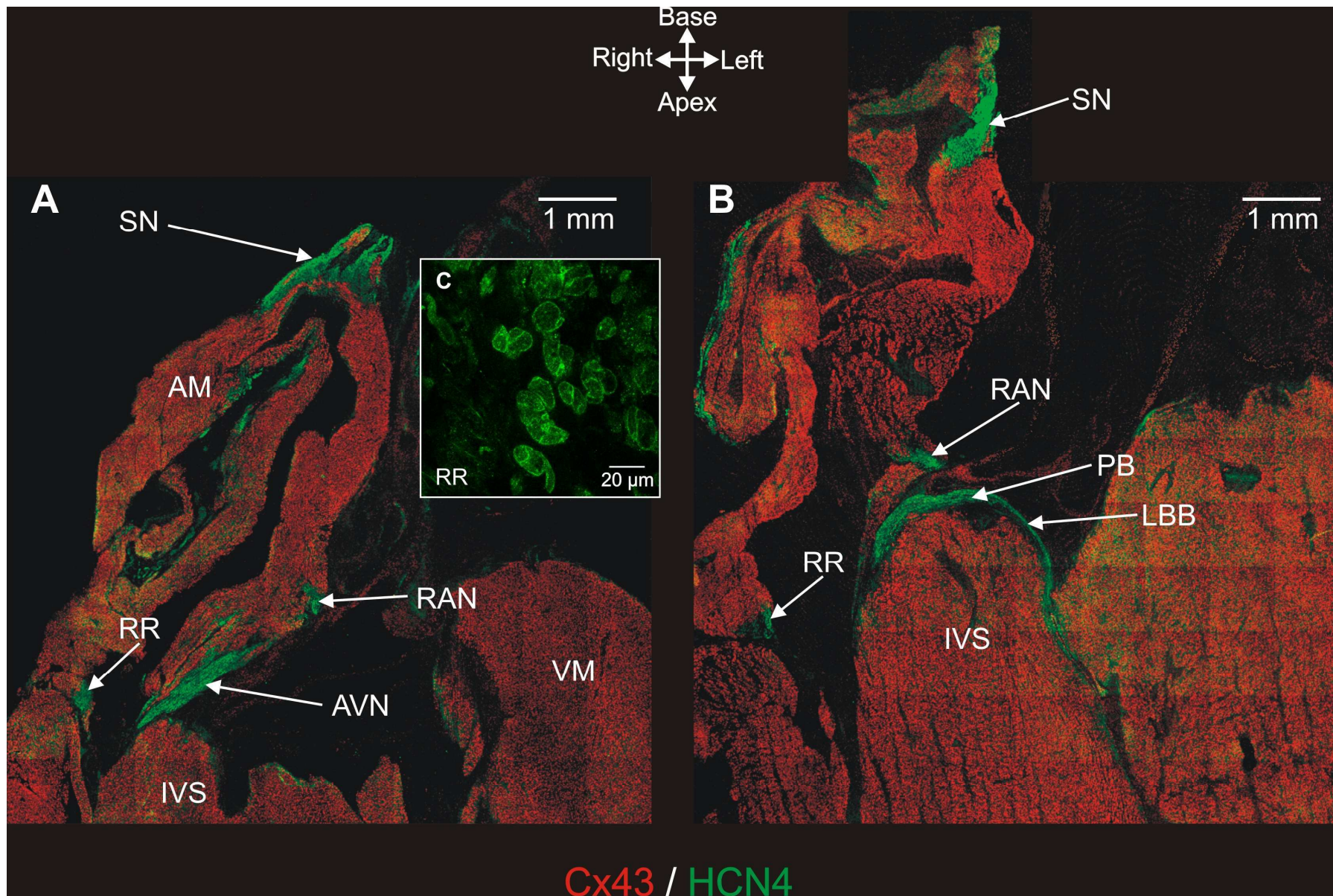


Figure 2.

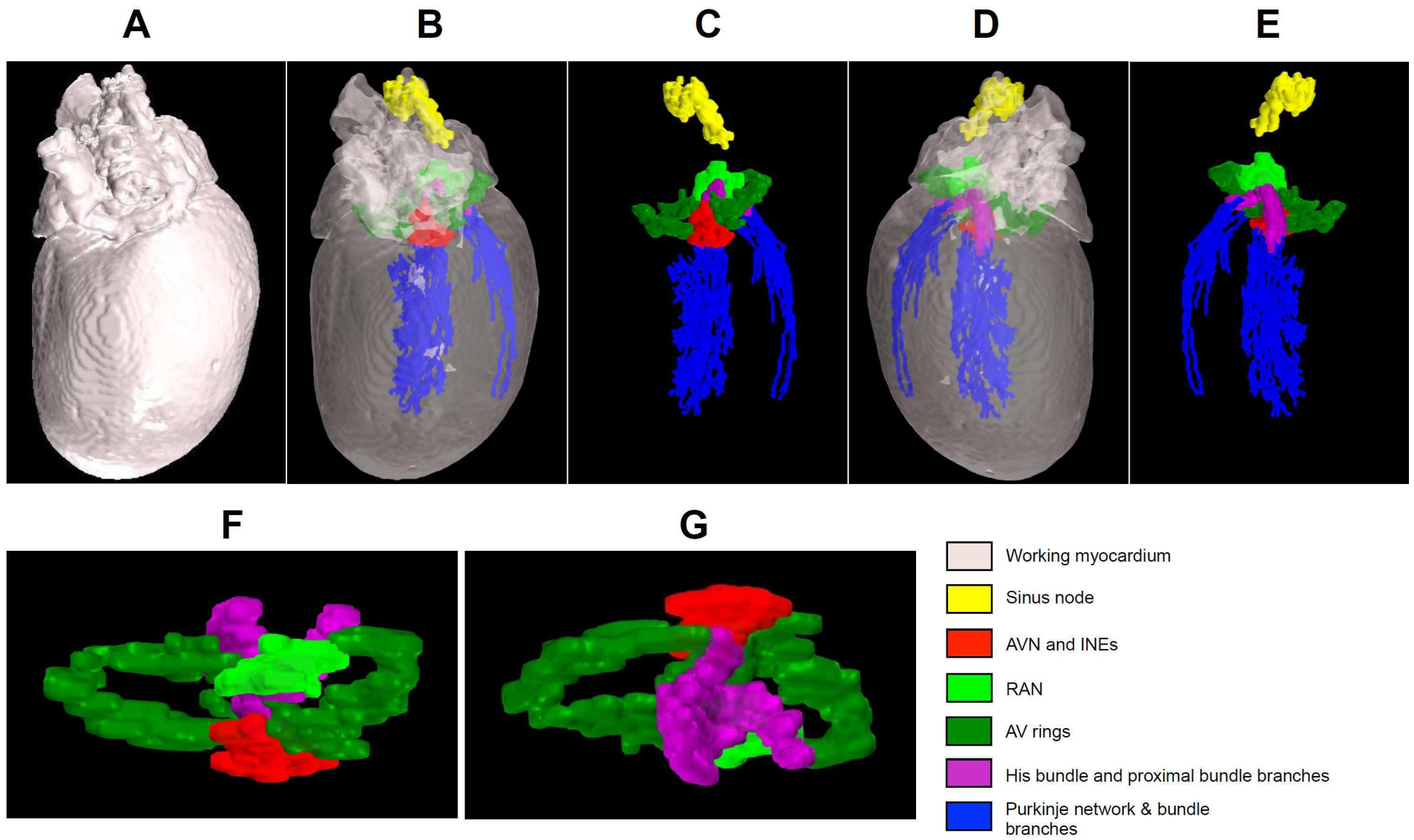


Figure 3.

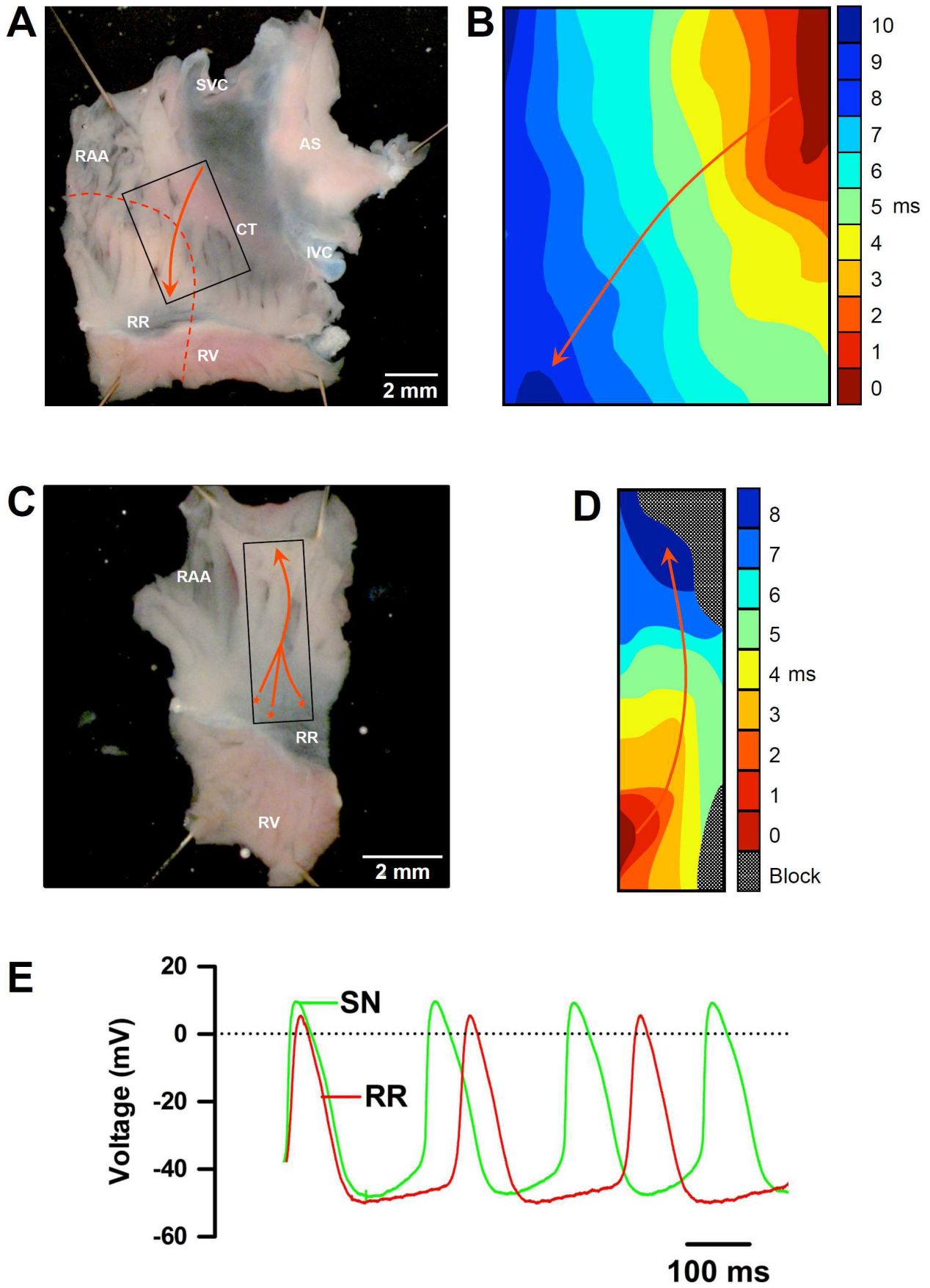


Figure 4.

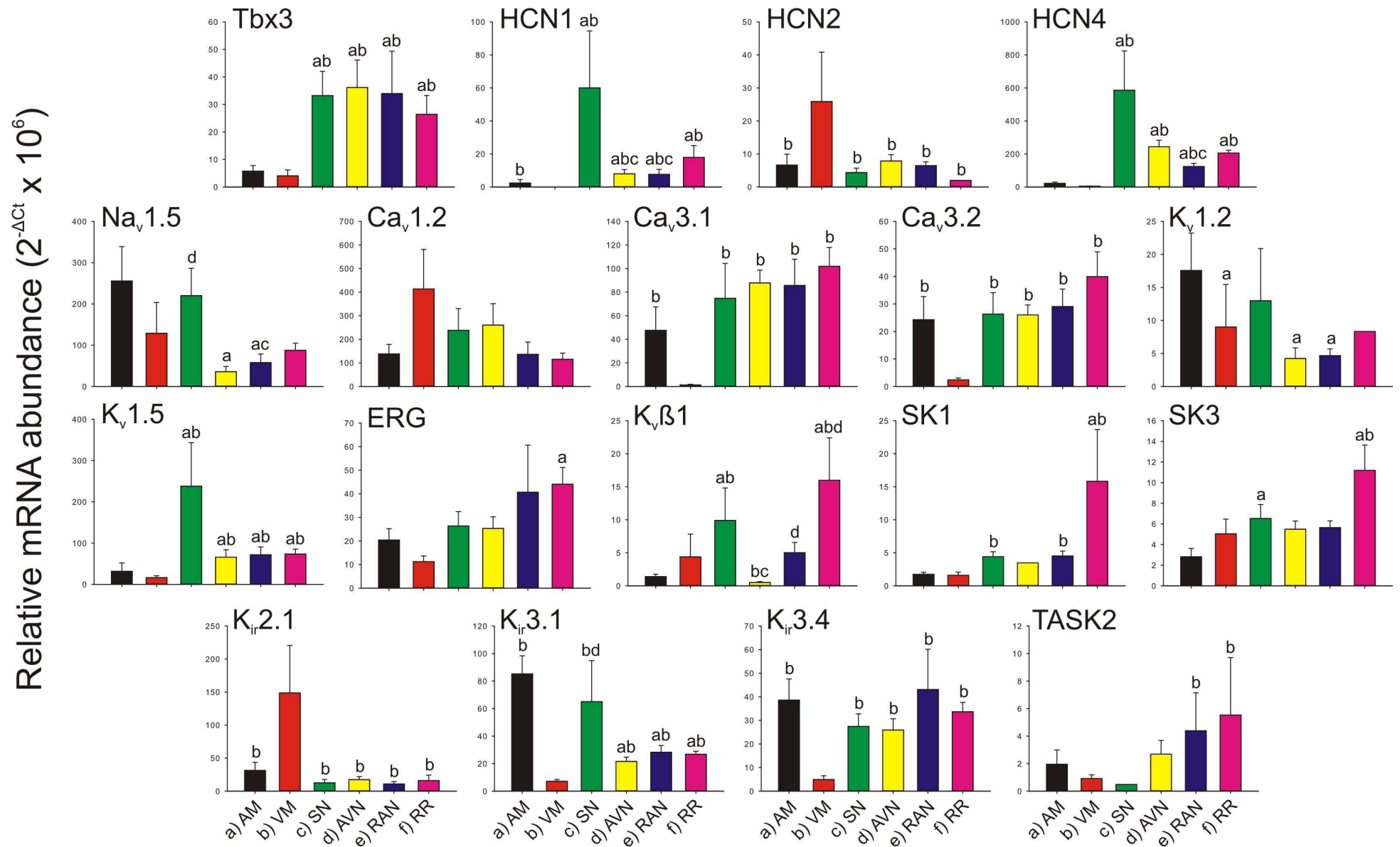


Figure 5.

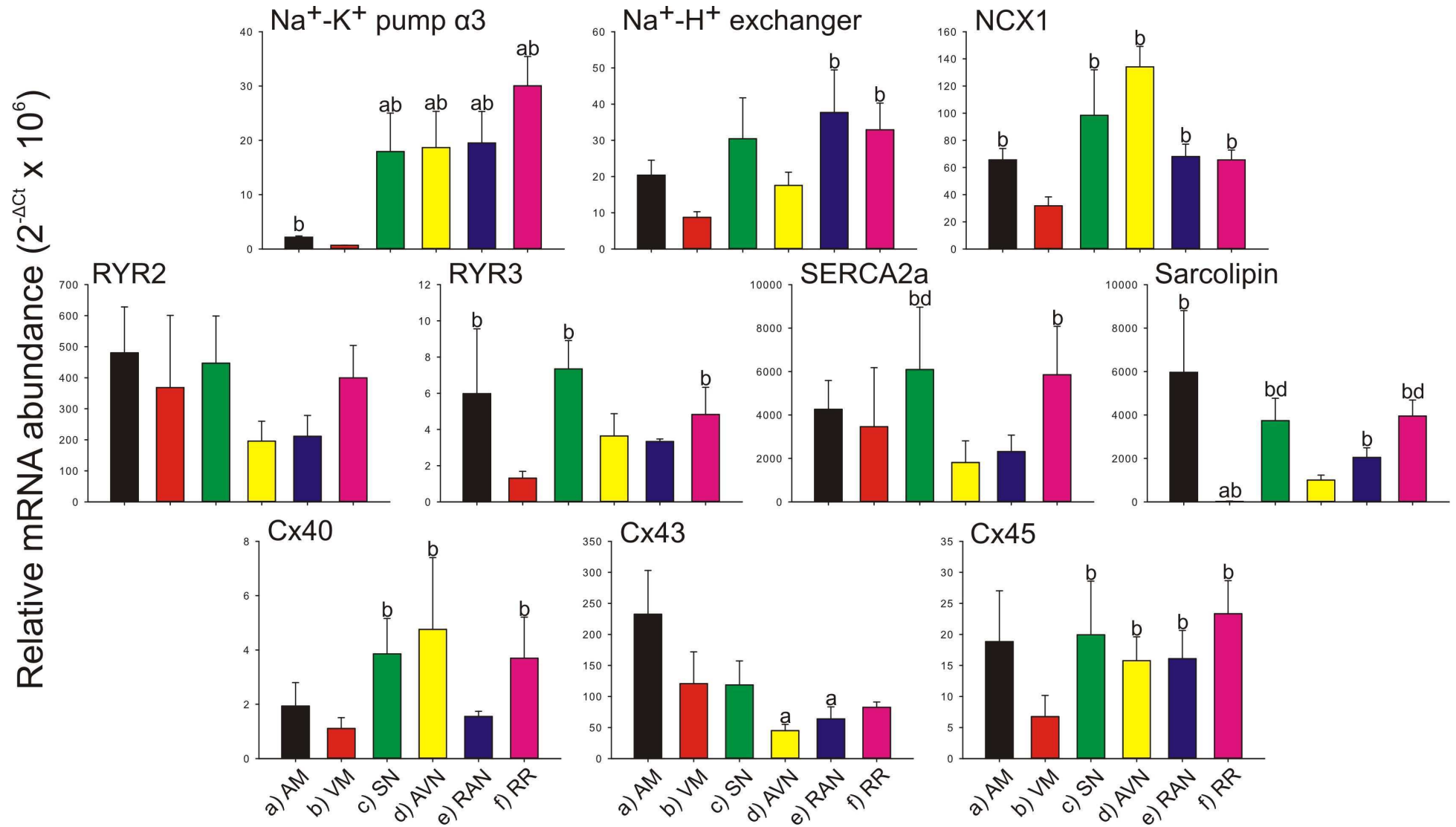
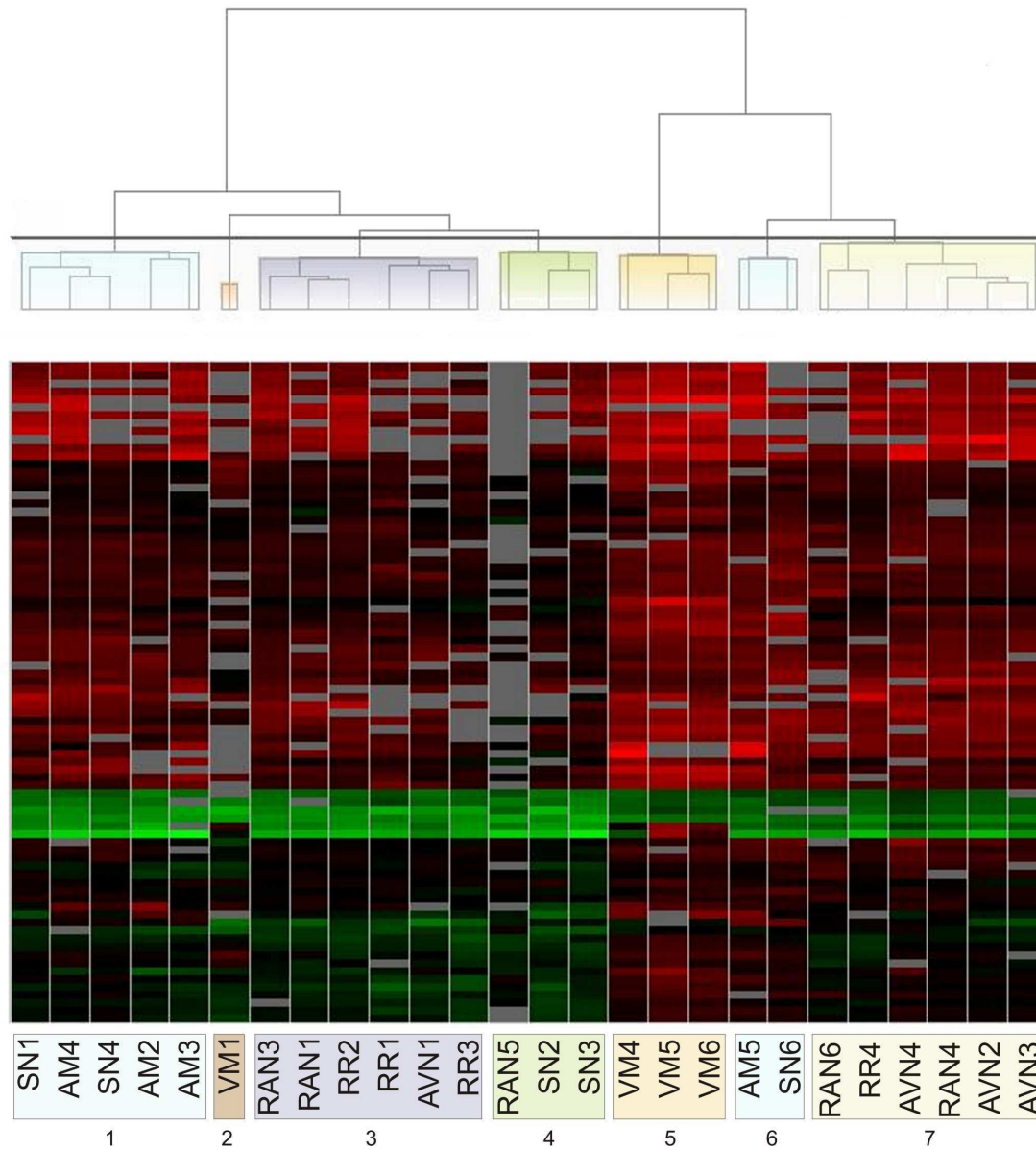
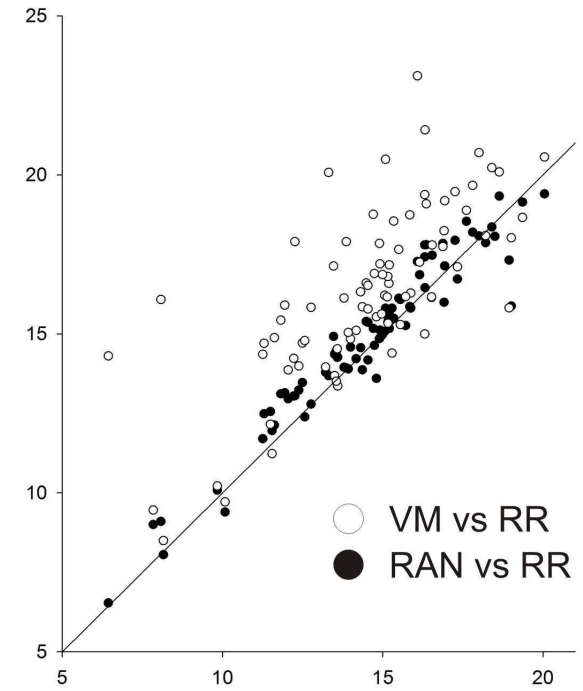


Figure 6.

A



B



C

	AVN	RAN	RR	SN	VM
AM	84.9	87.9	85.8	90.2	83.3
AVN		96.9	94.0	92.5	72.1
RAN			96.6	92.6	74.8
RR				92.1	73.6
SN					74.8

Figure 7.

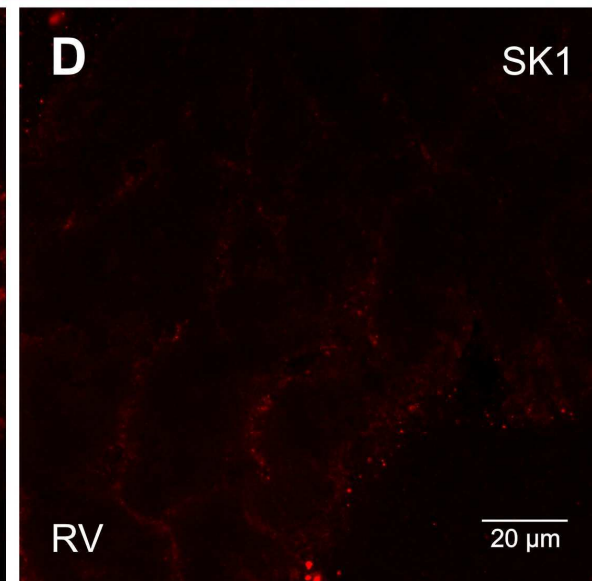
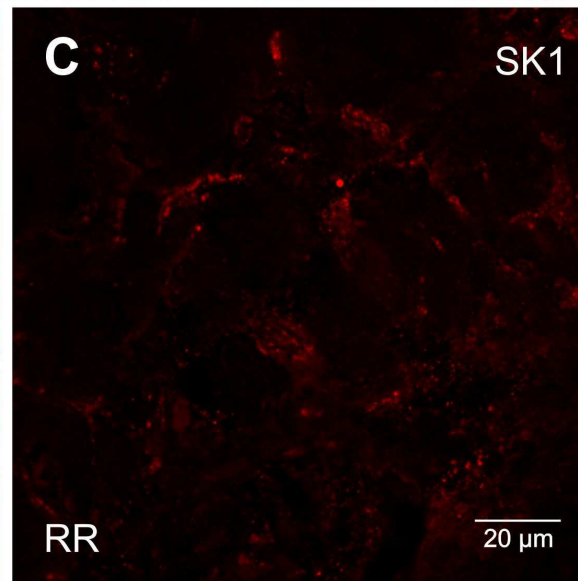
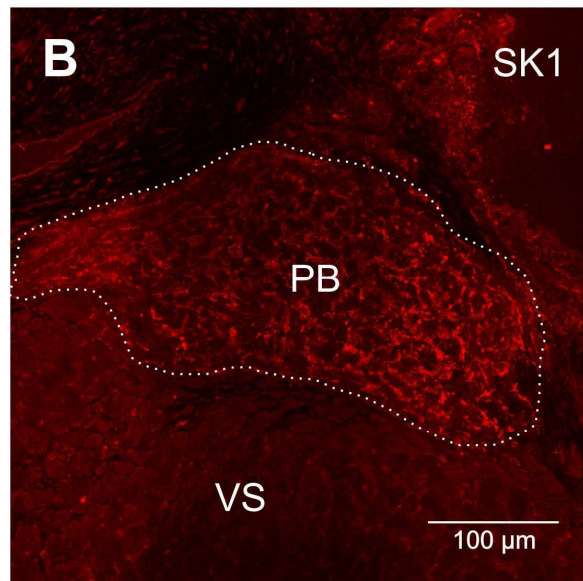
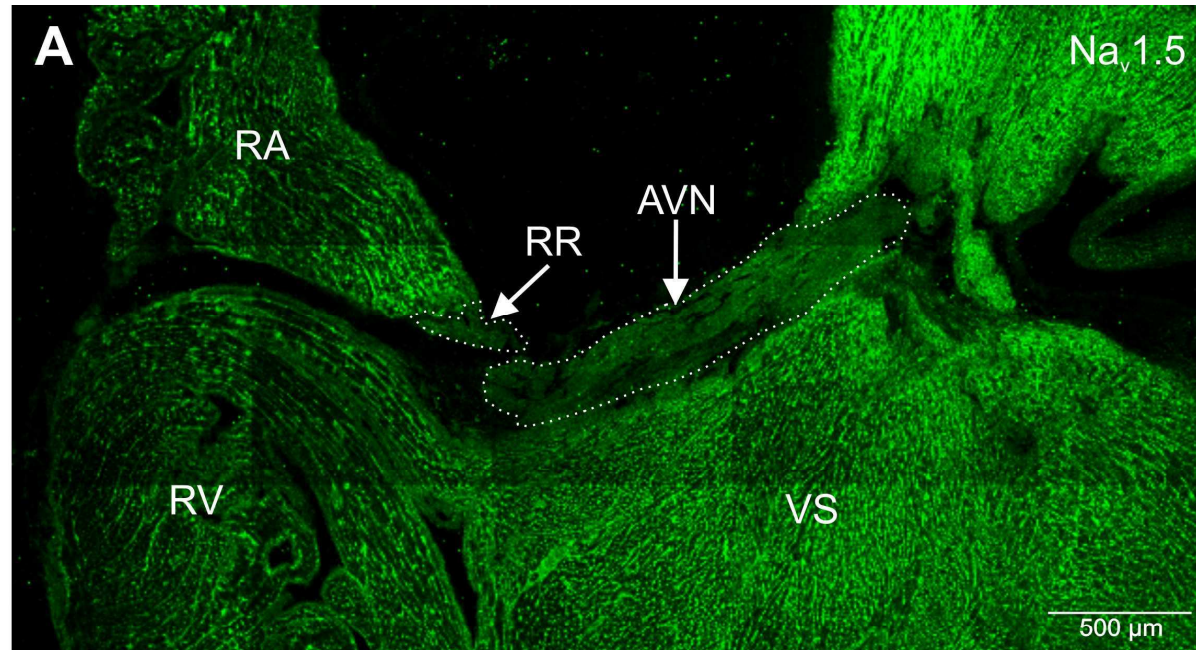
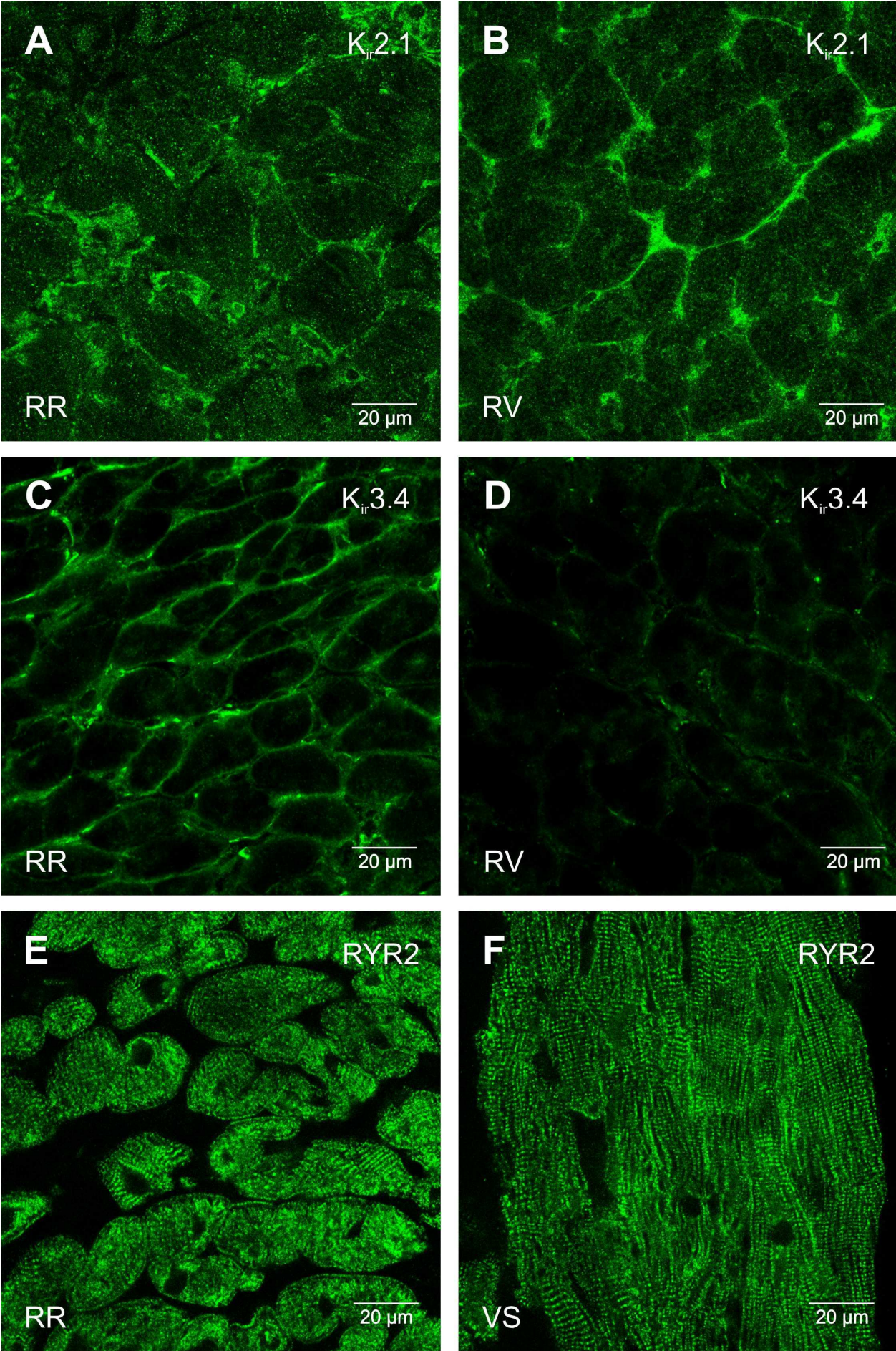


Figure 8.



**Appendix III: Mitogen-activated protein kinase
kinase 4 deficiency in cardiomyocytes causes
connexin 43 reduction and couples hypertrophic
signals to ventricular arrhythmogenesis**

Mitogen-activated Protein Kinase Kinase 4 Deficiency in Cardiomyocytes Causes Connexin 43 Reduction and Couples Hypertrophic Signals to Ventricular Arrhythmogenesis^{*[5]}

Received for publication, February 7, 2011, and in revised form, March 23, 2011. Published, JBC Papers in Press, March 28, 2011, DOI 10.1074/jbc.M111.228791

Min Zi^{‡1}, Tomomi E. Kimura^{§1}, Wei Liu[§], Jiawei Jin[§], Jonathan Higham[¶], Sanjay Kharche[¶], Guoliang Hao[‡], Ying Shi[‡], Weijian Shen[¶], Sukhpal Prehar[‡], Aleksandr Mironov[§], Ludwig Neyses[‡], Marti F. A. Bierhuizen^{||}, Mark R. Boyett[‡], Henggui Zhang[¶], Ming Lei[‡], Elizabeth J. Cartwright[‡], and Xin Wang^{§2}

From the [§]Faculty of Life Sciences, [‡]Manchester Academic Health Sciences Centre, and [¶]School of Physics and Astronomy, The University of Manchester, Manchester M13 9NT, United Kingdom and the ^{||}Department of Medical Physiology, Division Heart & Lungs, University Medical Center Utrecht Yalelaan 50, 3584 CM Utrecht, The Netherlands

Connexin 43 (Cx43)³ is the predominant isoform of gap junction proteins in the working myocardium. In the heart, MAPKs are implicated in regulating Cx43 remodeling; however, their precise roles remain obscure. Mitogen-activated protein kinase 4 (MKK4) is a critical component of the stress-activated MAPK signaling pathway. We have demonstrated previously that MKK4 antagonizes cardiomyocyte hypertrophy. Herein, we investigate the role of MKK4 in regulating Cx43 expression in cardiomyocytes. We found that knockdown of MKK4 expression or inhibition of its kinase activity in neonatal rat cardiomyocytes (NRCMs) significantly reduced phenylephrine-induced Cx43 expression. Furthermore, two activator protein-1 (AP-1) binding elements in the Cx43 promoter region were identified as being responsible for the MKK4-regulated Cx43 expression. Consistently, we also detected heterogeneously reduced Cx43 expression and attenuated zonula occludens-1 (ZO-1) content in the hearts of MKK4 cardiomyocyte-specific knock-out mice (MKK4^{cko}) following pressure overload. To test whether heterogeneously reduced Cx43 expression contributes to ventricular arrhythmic vulnerability, MKK4^{cko} and control mice were subjected to pressure overload followed by programmed electrical stimulation (PES). Six of 13 MKK4^{cko} mice, but none of the controls, developed ventricular tachycardia. Epicardial activation mapping recorded from the MKK4^{cko} hypertrophied heart showed ventricular activation delay. Mathematical models have simulated that the spatially heterogeneous decrease in Cx43 causes slowed ventricular con-

duction and fragmented wave propagations leading to re-entrant excitations. Collectively, these data reveal a novel role for MKK4 in regulating Cx43 expression and preventing hypertrophy-associated arrhythmogenesis.

Cx43 is the predominant isoform of gap junction proteins in the working myocardium. It forms low resistance cell-to-cell channels, allowing ions and small molecules to move between adjacent cells and facilitating the orderly spread of the excitation wave responsible for synchronous contraction of the heart (1). Alterations in Cx43 expression may contribute directly to the arrhythmic substrate, as evidenced by studies in mice with a cardiomyocyte-specific deletion of Cx43. Loss of Cx43 expression in the heart results in sudden arrhythmic death due to increased gap junctional resistance and slowed conduction velocity, which form a substrate for re-entrant arrhythmias (2–4). Cx43 has a fast turnover rate with a half-life in the range of 1–5 h, implying a highly regulated process for its synthesis, trafficking, and degradation (1, 5). In the heart, MAPKs are implicated in regulating Cx43 remodeling by either phosphorylation- or transcription-dependent mechanisms (6–11); however, their precise roles are ambiguous. For example, activation of JNK in cardiomyocytes was correlated with the up-regulation of Cx43 after amphetamine treatment (6), whereas Petrich *et al.* (7, 8) reported that in the hearts of transgenic mice overexpressing constitutive active MKK7 increased JNK activity was accompanied by a substantial reduction in Cx43 expression.

MKK4 is a critical component of the stress-activated MAPK kinase signaling pathway, which activates JNKs to regulate diverse physiological processes (12). It was observed *in vitro* that MKK7 and MKK4 preferentially phosphorylate JNK on threonine 183 and tyrosine 185, respectively (13, 14). The targeted deletion of the *mkk4* or *mkk7* gene leads to embryonic lethality, providing genetic evidence that MKK4 and MKK7 have nonredundant roles *in vivo* (12). This concept is underscored by the observation in mice with brain-specific ablation of *mkk4* that decreased JNK activity caused a defect in neuronal migration and premature death (15). Furthermore, we have provided substantial evidence demonstrating the functional importance of MKK4 in the heart, where it is required in protecting the heart from maladaptive pathological hypertrophy (16).

* This work was supported by British Heart Foundation Grants PG/07/055/23144 (to X. W. and E. J. C.) and PG/09/052/27833 (to X. W., E. J. C. and M. L.).

[5] The on-line version of this article (available at <http://www.jbc.org>) contains supplemental "Materials and Methods," Figs. 1 and 2, and additional references.

¹ Both authors contributed equally to this work.

² To whom correspondence should be addressed: Faculty of Life Sciences, University of Manchester, CTF Bldg., 46 Grafton St., Manchester M13 9NT, United Kingdom. Tel.: 44-161-275-5616; Fax: 44-161-275-5600; E-mail: xin.wang@manchester.ac.uk.

³ The abbreviations used are: Cx43, connexin 43; MKK4, mitogen-activated protein kinase 4; NRCM, neonatal rat cardiomyocyte; PE, phenylephrine; AP-1, activator protein-1; ZO-1, zonula occludens-1; PES, programmed electrical stimulation; Luc, luciferase; TAC, transverse aortic constriction; ECG, electrocardiography; CV, conduction velocity; SP-1, specific protein-1; QTc, corrected QT; rCx43, rat Cx43; Ad, adenovirus; caMKK4, constitutively active MKK4; dnMKK4, dominant negative MKK4.

MKK4 Regulates Cx43 Expression in Cardiomyocytes

In the current study, we investigated the role of MKK4 in regulating Cx43 expression in cardiomyocytes in response to hypertrophic stress. We found in NRCMs that knockdown of endogenous MKK4 expression by siMKK4 or inhibition of its kinase activity by infection of an adenovirus encoding a dominant-negative form of MKK4 (Ad-dnMKK4) caused a substantial reduction in Cx43 expression together with inactivation of the JNK/c-Jun pathway after phenylephrine (PE) stimulation. To gain insight into the mechanism responsible for the decreased Cx43 transcript level, luciferase reporter assays were performed in siMKK4- or Ad-dnMKK4-NRCMs in which blunted Cx43 promoter reporter activity was detected after PE treatment. We also have demonstrated that MKK4 regulates Cx43 transcription most likely by virtue of two AP-1 binding sites in the Cx43 proximal promoter region.

Consistent with these data, we observed decreased transcript and protein levels of Cx43 in the MKK4-deficient myocardium after 1 week of transverse aortic constriction (TAC). Furthermore, the remaining Cx43 was found to be distributed heterogeneously in the MKK4^{cko}-TAC hearts. In addition, we discovered a reduction in ZO-1 protein expression in the MKK4^{cko}-TAC myocardium. To assess whether heterogeneously reduced Cx43 in the MKK4-deficient myocardium contributes to ventricular arrhythmic vulnerability, PES was applied to TAC-treated MKK4^{cko} and MKK4^{fl/fl} (littermate controls) mice, almost half of the MKK4^{cko} mice (six of 13) compared with none of the controls (0/11) exhibited multiple episodes of ventricular tachycardia. Epicardial activation mapping was recorded in the isolated Langendorff-perfused hearts showing ventricular activation delay in the MKK4^{cko}-TAC heart. Accordingly, mathematical simulation models have demonstrated that the spatially heterogeneous decrease in Cx43 in MKK4^{cko}-TAC mice causes slowed ventricular conduction and fragmented excitation wave fronts leading to re-entry, which may account for the increased susceptibility in ventricular arrhythmias.

Overall, in the present work, we provide new information revealing the role of MKK4 in regulating Cx43 gene expression in cardiomyocytes, implying MKK4 is a critical cardiac protector preventing hypertrophy-associated ventricular arrhythmias through restriction of Cx43 remodeling.

EXPERIMENTAL PROCEDURES

Animal Models—MKK4^{fl/fl} and their littermates MKK4^{cko} mice were generated previously (16) and used in the present study. All mice were maintained in a pathogen-free facility at the University of Manchester. The animal studies were performed in accordance with the UK Home Office and institutional guidelines.

Quantitative Real-time PCR—Total RNA was prepared from NRCMs or ventricular tissues. Real-time quantitative PCRs were performed using the SYBR Green I Core kit (Eurogentec). The primers used for detection of Cx43 and GAPDH expression were obtained from Qiagen.

Immunoblot Analysis—Protein extracts (50 μ g) were subjected to immunoblot analysis with antibodies against Cx43, N-cadherin, β -catenin, plakoglobin, and tubulin (Sigma);

ZO-1 (Zymed Laboratories Inc.); MKK7, JNK, c-Jun, phospho-JNK, and phospho-cJun (Cell Signaling); and MKK4 (BD Pharmingen).

Immunohistochemical Analyses—Fresh cryosections of ventricular tissues were used to analyze Cx43, N-cadherin, β -catenin, and plakoglobin by indirect immunofluorescence. As secondary antibodies, goat anti-mouse or goat anti-rabbit antibodies, conjugated to Alexa Fluoro 488 (Invitrogen) or Alexa Fluoro 568 (Invitrogen), respectively, were used.

Adenovirus Vector Construction—Using the vector containing the rat Cx43 (rCx43) promoter region (−148, +280) as a template, we created a single mutation at either the AP-1 (−47, −39) site, or the AP-1 (−122, −112) site, or double mutations at both AP-1 sites using the QuikChange site-directed mutagenesis kit (Stratagene). Adenovirus expressing wild type Cx43 promoter-Luc or various mutations was generated using ViraPower Adenoviral Expression System (Invitrogen).

Luciferase Reporter Assay—48 h post-transfection of siRNA, NRCMs were infected with Ad-Cx43APwt-Luc for 24 h. Following PE treatment (100 μ M for 24 h), aliquots of NRCM lysates were assayed for luciferase activity using a luciferase assay kit (Promega). To measure rCx43 promoter-luciferase activity after blocking MKK4 activation, NRCMs were infected with Ad-dnMKK4 for 24 h prior to the infection of Ad-Cx43APwt-Luc for a further 24 h. Then, NRCMs were treated with 100 μ M PE for 24 h followed by the luciferase assay. To determine whether MKK4-regulated Cx43 transcription was dependent on AP-1 transcriptional activity, NRCMs were first infected with either Ad-GFP or Ad-caMKK4 for 24 h, Ad-Cx43APwt-Luc, or Ad-Cx43APma-Luc, or Ad-Cx43APmb-Luc, or Ad-Cx43APdm-Luc was added to either Ad-GFP-NRCMs or Ad-caMKK4-NRCMs for a further 24 h. Luciferase activity in each experimental group was then measured described as above.

ECG—8–10 week old male MKK4^{fl/fl} and MKK4^{cko} mice were subjected to either sham or TAC operation for 1 week as described previously (16). To monitor cardiac rhythms at baseline and in hypertrophic conditions, we carried out *in vivo* ECG analysis on anesthetized mice. RR interval, P wave duration, PR interval, QRS, JT and QT durations were recorded.

PES—To assess propensity to ventricular arrhythmias, 1 week TAC-treated mice were subjected to PES. A pacing train of eight stimuli (S1) was delivered at a basic cycle length of 100 ms, with a single (S2) premature extrastimulus introduced at progressively shorter intervals until an arrhythmia was induced or the ventricular refractory period was reached.

Epicardial Activation Mapping—Epicardial activation mapping of the left ventricular free wall was recorded in isolated Langendorff-perfused hearts using custom-made 64 separated electrodes (8 \times 8 grids, 0.55-mm spacing) at a basic cycle length of 100 ms. The activation time was determined as the point of maximal negative slope and displayed in a grid representing the layout of the original recording

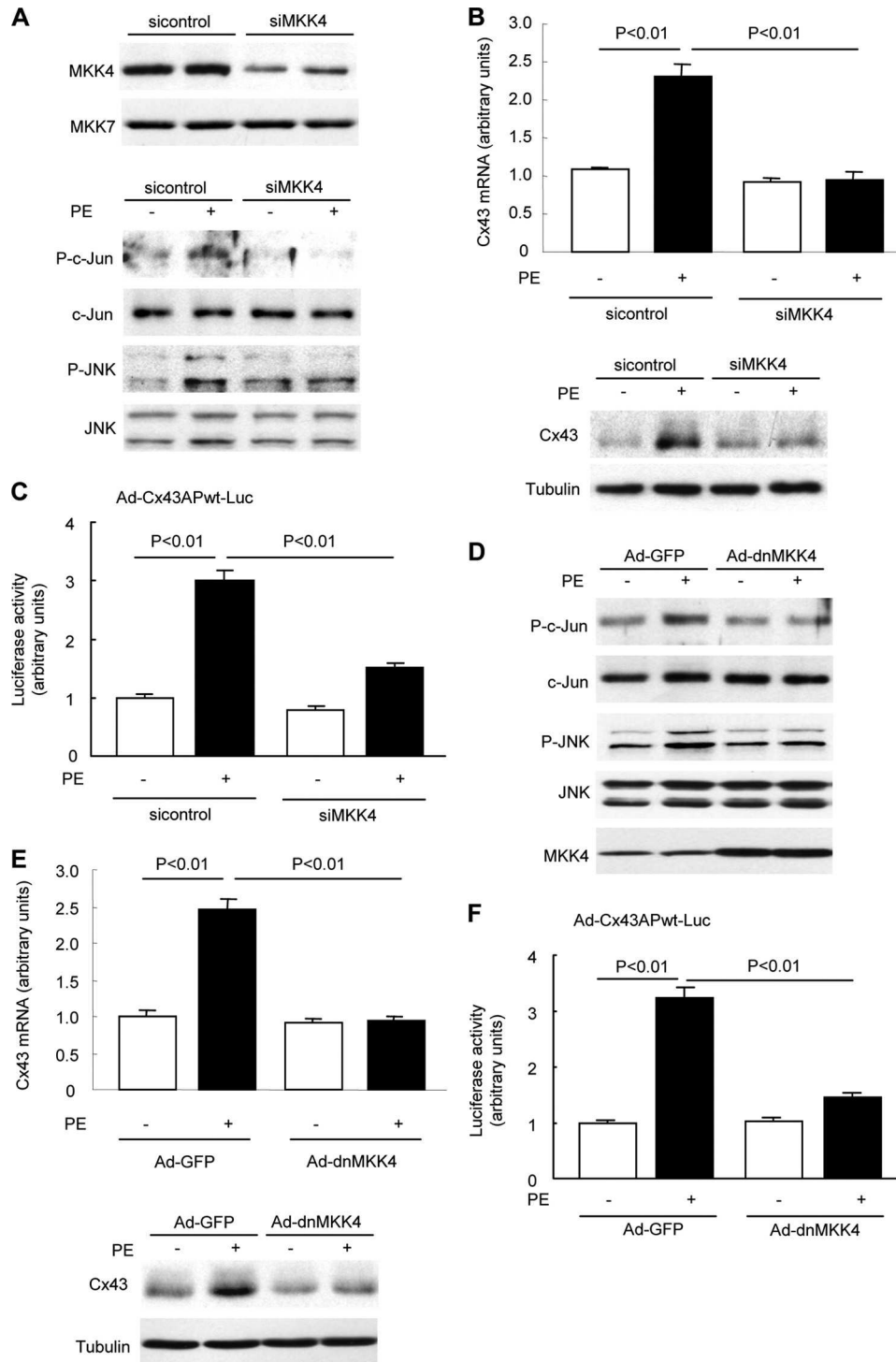


FIGURE 1. MKK4 regulates Cx43 expression via JNK/c-Jun activation in cardiomyocytes. *A*, NRCMs were transfected with MKK4 siRNA or control siRNA for 72 h prior to immunoblotting for MKK4 expression. MKK7 protein expression was examined to determine the specificity of MKK4 knockdown. siMKK4-NRCMs were treated with PE (100 μ M) for 30 min before detecting phosphorylation of JNK and c-Jun by immunoblotting. *B*, quantitative real-time PCR analyses of Cx43 transcript levels (*upper panel*) and immunoblot analysis of Cx43 protein expression (*lower panel*) in siMKK4-NRCMs following PE treatment (100 μ M, 48 h). Tubulin expression is the protein loading control. *C*, siRNA-transfected NRCMs were infected with AdCx43APwt-Luc (multiplicity of infection, 25) for 24 h followed by PE treatment (100 μ M, 24 h). The Cx43 promoter-dependent luciferase activity was measured by the luciferase reporter assay system. Data are mean \pm S.E. ($n = 3$ per group). *D*, Ad-dnMKK4-NRCMs were treated with PE (100 μ M) for 30 min before detecting activation of c-Jun and JNK by immunoblotting. Immunoblot analysis shows MKK4 expression in Ad-dnMKK4-NRCMs. *E*, quantitative real-time PCR analyses of Cx43 transcript levels (*upper panel*) and immunoblot analysis of Cx43 protein expression (*lower panel*) in Ad-dnMKK4-NRCMs. Ad-GFP is a control virus. Tubulin expression is the protein loading control. *F*, infection of Ad-dnMKK4 in cardiomyocytes decreased the PE-induced Cx43 promoter-dependent luciferase activity. Data are mean \pm S.E. ($n = 3$ per group).

array. All activation times were related to the timing of the first detected waveform. Isochrones were drawn manually around areas activated in steps of 1 ms.

Statistical Analysis—Data are expressed as mean \pm S.E. and analyzed using two-way analysis of variance followed by Bonferroni's post test where appropriate. Comparisons between

MKK4 Regulates Cx43 Expression in Cardiomyocytes

two groups were performed using Student's *t* test. *p* values <0.05 are considered statistically significant. An expanded "Materials and Methods" section is available in the [supplemental data](#).

RESULTS

MKK4 Regulates Cx43 Gene Expression via AP-1 Binding Sites—Transcriptional regulation is a key mechanism dictating Cx43 expression. The down-regulation of Cx43 ascribable to altered transcriptional regulation has been reported in many forms of heart disease (17, 18). To investigate whether MKK4 regulates Cx43 expression in response to hypertrophic stress, we first examined Cx43 mRNA level and protein expression in NRCMs in which endogenous MKK4 protein was knocked down by 70% using siMKK4 (Fig. 1A). Blunted phosphorylation of JNK and c-Jun after PE stimulation was observed when MKK4 expression was deficient (Fig. 1A). In response to PE stimulation (100 μ M, 48 h), siMKK4-NRCMs showed a significant reduction in Cx43 mRNA level, and a corresponding substantial decrease in its protein expression also was detected (Fig. 1B). We performed a systematic promoter-reporter study in NRCMs to determine the regulation of the rCx43 proximal promoter by MKK4. NRCMs were pretreated with siMKK4 prior to infection with a recombinant adenovirus encoding the rCx43 promoter region extending 148 nucleotides upstream to 281 nucleotides downstream relative to the transcription initiation site (−148 to +281, containing two AP-1 binding sites, Ad-Cx43APwt-Luc). Following PE stimulation (100 μ M, 24 h), a significant decline in rCx43 promoter-luciferase activity was detected in siMKK4-NRCMs *versus* that in the control siRNA-NRCMs (Fig. 1C). To corroborate these data, we then infected NRCMs with a recombinant adenovirus expressing a dominant-negative form of MKK4 (Ad-dnMKK4) to block activation of the JNK/c-Jun pathway (Fig. 1D). Similarly, significantly reduced Cx43 mRNA and protein levels were observed in Ad-dnMKK4-NRCMs (Fig. 1E). Moreover, PE stimulation failed to induce a similar extent of rCx43 promoter-luciferase activity in Ad-dnMKK4-NRCMs, compared with that in Ad-GFP-NRCMs (Fig. 1F). To determine whether MKK4-regulated Cx43 transcription is dependent on AP-1 transcriptional activity, we generated various recombinant adenoviruses containing either a single mutation at the AP-1 (−47 to −39) site, referred to as Ad-Cx43APma-Luc; or mutation at the AP-1 (−122 to −112) site, referred to as Ad-Cx43APmb-Luc, or double mutations at both AP-1 binding sites (Ad-Cx43APdm-Luc) (Fig. 2A). As shown in Fig. 2B, infection of adenovirus encoding constitutively active MKK4 (Ad-caMKK4) significantly increased the Ad-Cx43APwt-Luc activity in NRCMs. Conversely, Ad-Cx43APdm-Luc activity proved to be considerably decreased even at basal level, co-infection of Ad-caMKK4 into NRCMs failed to restore its luciferase activity. Co-infection of Ad-caMKK4 with either Ad-Cx43APma-Luc or Ad-Cx43APmb-Luc could not render a similar level of luciferase activity as Ad-Cx43APwt-Luc. Together, these results indicate that MKK4 is required for Cx43 transcription, acting through two AP-1 binding sites in the Cx43 proximal promoter via JNK/c-Jun activation. Decreased Cx43 protein expression is likely attributable to reduced its mRNA level.

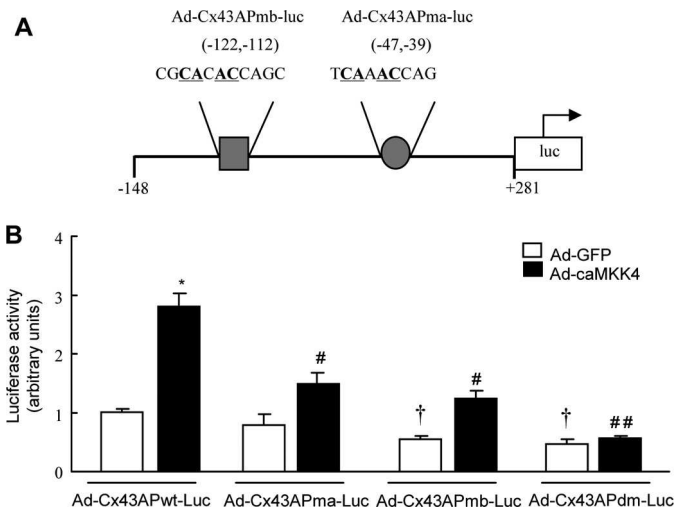


FIGURE 2. MKK4-regulated Cx43 transcription is dependent on AP-1 transcriptional activity. A, schematic diagram of mutated rCx43 promoter-luciferase constructs (mutated nucleotides are *underlined* and in *boldface*). B, the infection of Ad-caMKK4 significantly increased the Ad-Cx43APwt-Luc activity. *, *p* < 0.01 *versus* Ad-GFP + Ad-Cx43APwt-Luc. Ad-Cx43APdm-Luc activity was decreased even at the basal level. †, *p* < 0.05 compared with Ad-GFP + Ad-Cx43APwt-Luc. Co-infection of Ad-caMKK4 and Ad-Cx43APdm-Luc could not ameliorate the reduction. ##, *p* < 0.001 *versus* Ad-caMKK4 + Ad-Cx43APwt-Luc. Moreover, co-infection of Ad-caMKK4 failed to restore the reduced luciferase level induced by Ad-Cx43APma-Luc or Ad-Cx43APmb-Luc. #, *p* < 0.01 *versus* Ad-caMKK4 + Ad-Cx43APwt-Luc (*n* = 6 per group). Data are mean \pm S.E.

Heterogeneous Reduction of Cx43 in MKK4^{cko}-TAC Mice—Prompted by the above findings, we then analyzed Cx43 mRNA levels, protein content, and distribution in the MKK4-deficient myocardium. As shown in Fig. 3A, a down-regulation of the Cx43 transcript was detected in the MKK4^{cko} hearts 1 week after TAC, which was applied to induce a pressure overload and subsequent hypertrophy on the heart. Accordingly, we observed a decreased Cx43 protein level (~50% of controls) in the MKK4^{cko} heart following 1 week TAC (Fig. 3B) and heterogeneity in Cx43 distribution shown by the absence of Cx43 labeling in some patches of the MKK4^{cko} ventricular free wall, whereas in some patches of the myocardium, Cx43 labeling was scattered in the cytoplasm (Fig. 3C). Quantification of the Cx43 immunofluorescence revealed reduced aggregate number by 42% and intensity by 49% in the MKK4^{cko}-TAC hearts compared with the littermate controls (MKK4^{ef/ef}-TAC), thus confirming heterogeneous Cx43 expression (Fig. 3C). In addition to Cx43, we also examined Cx40 and Cx45 expression in the MKK4^{cko} ventricles. Cx40 and Cx45 are important connexins in the heart. Cx40 is expressed predominantly in atrium, whereas Cx45 is the major gap junction isoform expressing in myocytes of the sinoatrial and atrioventricular nodes. By immunoblotting and immunohistochemistry, no detectable levels of Cx40 and Cx45 expression were observed in the ventricles of either MKK4^{cko} or MKK4^{ef/ef} mice (data not shown). Together, these data show that under hypertrophic stress MKK4 deficiency causes reduced and heterogeneous Cx43 expression.

ZO-1 Reduction in MKK4^{cko}-TAC Mice—Cx43 is localized primarily at the intercalated disc where gap junctions are in close proximity to zonula adherens junctions and desmosomes (19). ZO-1, a component of tight junctions, is known to be an

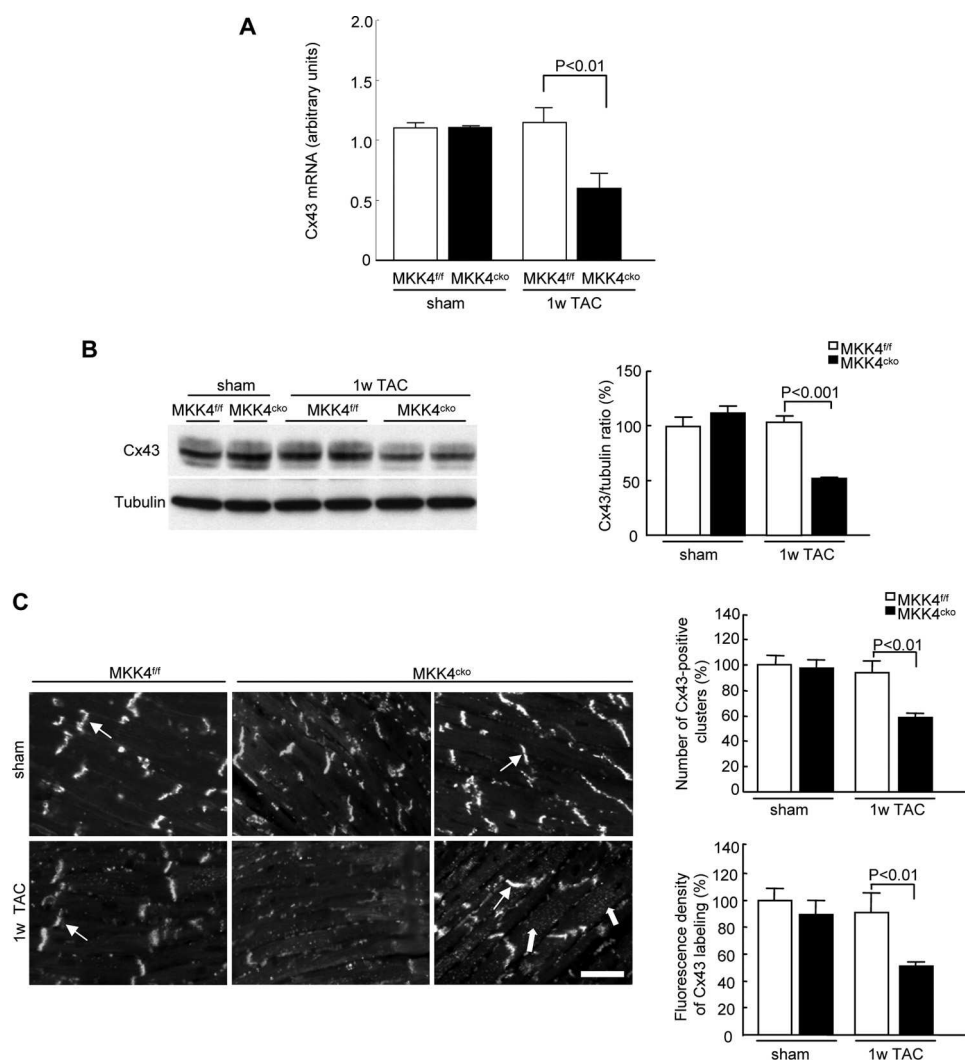


FIGURE 3. Reduced and spatially heterogeneous distribution of Cx43 in MKK4^{cko}-TAC mice. *A*, quantitative real-time PCR analyses of Cx43 transcript levels. The data are derived from three independent experiments performed in triplicate and are normalized to the GAPDH content ($n = 5$ per group). *B*, immunoblot analyses demonstrate significantly decreased Cx43 content. Tubulin expression is the protein loading control. The ratios of Cx43/tubulin are represented by the bar graphs ($n = 6$ per group). *C*, immunohistochemical staining of Cx43 in MKK4^{cko} mice. *Thick arrows* point to diffuse Cx43 labeling in the cytoplasm, whereas *thin arrows* show Cx43 distributed in intercalated discs. *Scale bar*, 5 μm . The number of Cx43-positive clusters and fluorescence intensity of Cx43 labeling are quantified and expressed by the bar graphs ($n = 6$ per group). Data are mean \pm S.E. 1w TAC, 1-week TAC.

important adaptor protein for Cx43 (20). Because we found diffused Cx43 labeling in the MKK4^{cko}-TAC cardiomyocytes, we then analyzed whether changes in ZO-1 expression or localization occurred in MKK4-deprived myocardium after pressure overload. Indeed, immunoblot analysis showed a $\sim 30\%$ diminution in ZO-1 protein expression in the MKK4^{cko}-TAC heart (Fig. 4A); this result was further confirmed by immunohistochemistry (Fig. 4B). In addition, we analyzed N-cadherin, β -catenin, and plakoglobin expression, all of which are important for the assembly and maintenance of Cx43 at the plasma membrane (1, 21). Expression and localization of these junctional proteins were not different visibly between the controls and MKK4^{cko}-TAC mice as shown by immunoblotting and immunohistochemistry (supplemental Fig. 1). Examination of the structure of MKK4-deficient cardiomyocytes by transmission electron microscopy surprisingly showed that the structure of myofibrils, sarcomeres, and Z-lines appeared normal in the MKK4^{cko}-TAC cardiomyocytes relative to the controls (supplemental Fig. II). Adherens junctions and desmosomes

characterized as submembranous electron dense zones in the vicinity of intercellular spaces were visible in both genotypes (supplemental Fig. II). Combined, these results suggest that overall cytoarchitecture of the MKK4^{cko} cardiomyocytes appears normal and intact compared with the controls. As such, the patchy reduction in Cx43 expression is due most likely to loss of MKK4 and is not caused by any disruption in the intercalated disc. Moreover, a reduction in ZO-1 expression might play a role in the diffused positioning of cellular Cx43.

Disruption of MKK4 in Cardiomyocytes Sensitizes Mice to Ventricular Arrhythmias—Previous studies suggest that patchy Cx43 reduction likely forms a proarrhythmic substrate (2–4). Herein, we first examined surface ECG on anesthetized mice. The ECG recordings revealed marked abnormalities in ventricular conduction in MKK4^{cko}-TAC mice, reflected by wider QRS durations (16.02 ± 0.62 ms) compared with 10.37 ± 0.46 ms (QRS) in the controls (Table 1). QRS/QTc ratio also was significantly greater in the MKK4^{cko}-TAC heart compared with that in the control heart. However, no significant differences in

MKK4 Regulates Cx43 Expression in Cardiomyocytes

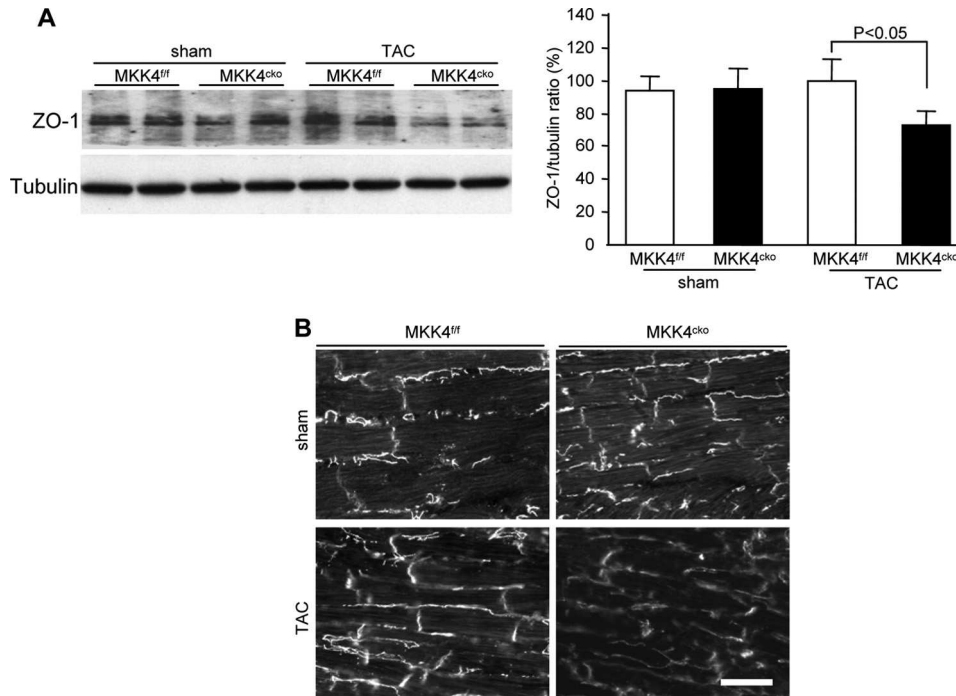


FIGURE 4. Decreased ZO-1 content in MKK4^{cko}-TAC mice. *A*, immunoblot analyses of ZO-1 expression show a moderate but significant decrease in the MKK4^{cko}-TAC heart. The ratios of ZO-1/tubulin are expressed in the bar graphs. *B*, immunohistochemical staining for ZO-1 confirmed decreased ZO-1 in the mutants (scale bar, 5 μ m). Data are mean \pm S.E ($n = 6$ per group).

TABLE 1

Electrocardiographic assessment of MKK4^{fl/fl} and MKK4^{cko} mice one week after TAC

P-wave duration, QRS complex duration, and intervals of RR, PR, JT, and QT were recorded from anesthetized mice. QTc was obtained by correction for the heart rate. Data are presented as mean \pm S.E. *, $p < 0.01$ versus MKK4^{fl/fl}-TAC mice.

ECG parameters	Sham		TAC	
	MKK4 ^{fl/fl} ($n = 7$)	MKK4 ^{cko} ($n = 6$)	MKK4 ^{fl/fl} ($n = 11$)	MKK4 ^{cko} ($n = 13$)
Heart rate (bpm)	376 \pm 12	403 \pm 13	391 \pm 17	398 \pm 15
P duration (ms)	10.2 \pm 0.9	10.1 \pm 1.0	11.3 \pm 1.1	10.5 \pm 0.7
RR interval (ms)	161.36 \pm 6.1	150.15 \pm 5.4	157.00 \pm 6.07	158.20 \pm 10.15
PR interval (ms)	39.99 \pm 1.90	38.38 \pm 1.70	37.92 \pm 1.99	37.36 \pm 2.28
QRS duration (ms)	10.27 \pm 0.75	10.50 \pm 0.51	10.37 \pm 0.46	16.02 \pm 0.62*
QTc (ms)	69.47 \pm 4.34	76.59 \pm 3.30	69.95 \pm 3.64	90.69 \pm 2.54*
JT (ms)	17.63 \pm 1.28	19.10 \pm 1.60	17.19 \pm 1.33	19.44 \pm 0.71
QRS/QTc	0.15	0.14	0.15	0.18*

JT intervals were observed in the two TAC groups (Table 1). These ECG parameters indicate slowed ventricular conduction in the MKK4^{cko}-TAC heart. Next, we performed PES to evaluate whether the heterogeneous decrease in Cx43 and slowed ventricular conduction sensitized MKK4^{cko} mice to ventricular arrhythmias. A train of eight stimuli (S1) was delivered at a basic cycle length of 100 ms, with a single extrastimulus (S2) added at progressively shorter intervals to induce ventricular arrhythmias. This S1-S2 pacing protocol induced multiple (more than six) episodes of ventricular tachycardia in six of 13 MKK4^{cko}-TAC mice, which lasted 1333 ± 182 ms (Fig. 5A). The ventricular effective refractory period also was determined by the same S1-S2 protocol. Consistent with the wider QRS duration, we noted a prolonged the ventricular effective refractory period in the MKK4^{cko}-TAC heart (Fig. 5B). To examine whether heterogeneously reduced Cx43 expression in MKK4-deficient myocardium affects ventricular electrical propagation, epicardial mapping of electrical activity of the left ventricular free wall was performed on the isolated Langendorff-perfused hearts. As illustrated in Fig. 5C, ventricular activation was significantly

delayed in the MKK4^{cko}-TAC heart, as shown by slowed conduction velocity (CV) at both longitudinal and transverse directions in the MKK4^{cko}-TAC heart, compared with that in the control heart (Fig. 5D).

Computational Simulations of Cx43 Remodeling—To substantiate the data from epicardial activation mapping, computer simulations were performed to address whether or not patched Cx43 reduction is proarrhythmic as suggested in this and previous studies (3, 21–23). First, we implemented a mathematical model of mouse ventricular myocytes to study CV in homogeneous tissue consisting of 100 cells. In this model, the changes in CV and wavelengths were studied based on an equivalent percentage of intercellular electrical coupling reduction uniformly across the strand to the reduced level of Cx43 expression observed in the MKK4^{cko}-TAC heart. As expected, the control CV of solitary wave in strands of myocytes was 0.603 mm/ms at an S1-S2 interval of 100 ms; however, a diminution in intercellular electrical coupling by 50% reduced the solitary wave CV to 0.415 mm/ms. Accordingly, the control wavelength (wavelength = CV \times averaged action potential duration at 90%

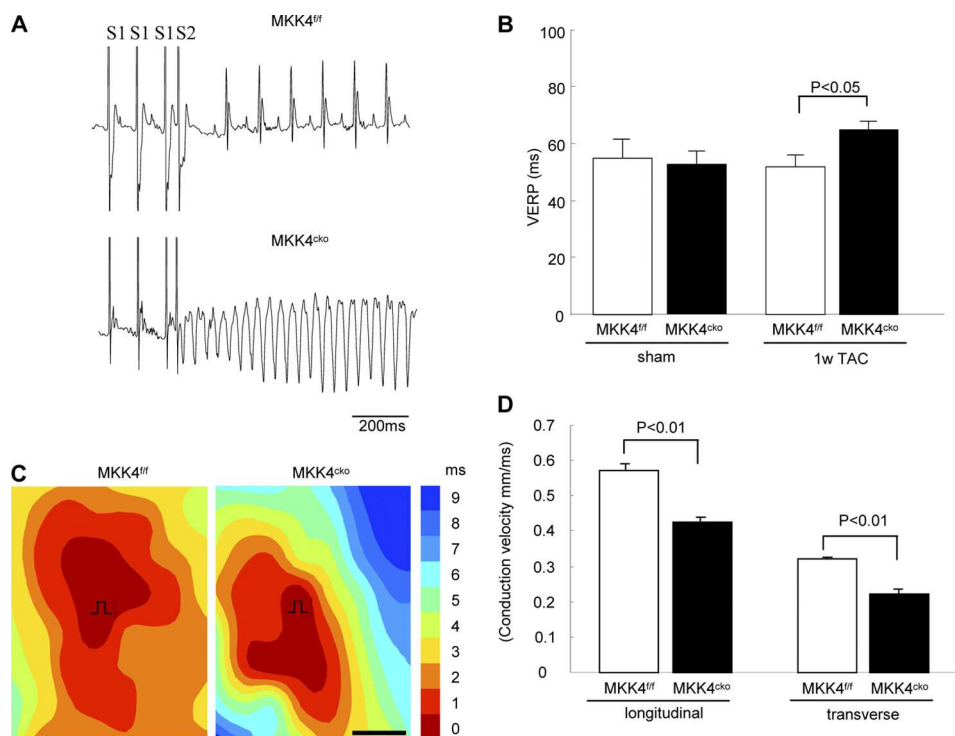


FIGURE 5. MKK4^{cko}-TAC mice are more susceptible to ventricular arrhythmias and slowed conduction velocity. *A*, subjected to a train of eight stimuli (S1 at 100 ms) with a premature stimulus at 90 ms (S2). No episodes of arrhythmias were induced in the MKK4^{fl/fl}-TAC heart (upper panel); however, ventricular tachycardia was induced in the MKK4^{cko}-TAC heart (lower panel) (scale bar: 200 ms). *B*, the ventricular effective refractory period was measured using the same S1-S2 protocol, showing a prolonged ventricular effective refractory period in the MKK4^{cko}-TAC heart ($n = 6-13$ per group). *C*, representative epicardial activation maps recorded from the MKK4^{fl/fl} and MKK4^{cko} hearts of TAC-treated mice. Earliest activation is found in red, the latest activation is shown in blue, and numbers indicate activation time (ms). The slowing of conduction and propagation of excitation was seen in the MKK4^{cko}-TAC heart. *D*, summary data illustrate that both longitudinal CV and transverse CV were significantly slower in the MKK4^{cko} heart ($n = 3$ per group). Data are presented as mean \pm S.E.

repolarization across the strand) of the solitary wave was 11.6 mm, and when intercellular electrical coupling was reduced by 50%, the wavelength was reduced to 8.8 mm, which is attributable to the decreased CV (Fig. 6, A–C). Further simulations were performed in a two-dimensional model of homogeneous ventricular tissue (ventricular tissue has a size of 10 mm \times 10 mm with 200 \times 200 cells) to study the effects of an arbitrarily and randomly distributed pattern of patched reduction in the intercellular electrical coupling on CV of planar and circular waves. With patched reduction of gap junctional coupling, break-up of the wavefronts was observed in all cases (Fig. 6D). These patches gave distorted wavefronts of the planar and circular waves, leading to fragmented wavefronts forming multiple re-entrant excitation wavelets. Together, the simulations show that heterogeneously reduced intercellular electrical coupling due to heterogeneously reduced expression of Cx43 most likely contributes to slowed conduction velocity, fragmented wavefronts of excitation waves, which increased propensity for arrhythmias.

DISCUSSION

In the present study, we provide several lines of evidence demonstrating that MKK4 regulates Cx43 expression in cardiomyocytes. Knockdown of MKK4 or blocking its kinase activity in primary rat neonatal cardiomyocytes resulted in a reduction in Cx43 expression. By promoter-reporter assays, we have shown that MKK4 modulates Cx43 expression through AP-1 activity. Study of the MKK4^{cko} heart provided *in vivo* evidence

demonstrating functional effects of MKK4 deficiency-induced Cx43 alteration. A deficiency of MKK4 in cardiomyocytes caused patchy Cx43 reduction in response to pressure overload. This alteration in Cx43 expression/distribution may constitute an arrhythmogenic substrate in MKK4^{cko}-TAC mice.

Regulation of Cx43 Expression by MKK4—Assembly of gap junctions is a multiphase process, including connexin synthesis, trafficking, and formation of intercellular channels, of which connexin synthesis is the rudimentary step. It has been shown that the Cx43 promoter region contains several putative transcription factor binding sites for AP-1, cAMP response element, and specific protein-1 (SP-1), all of which are thought to be involved in up-regulation of Cx43 transcription (24, 25). On the other hand, muscle segment homeobox genes *Msx1/2* can function in concert with T-box factors *Tbx2/3* to repress Cx43 expression (26). Despite this progress in understanding the transcriptional regulation of Cx43, the genetic control mechanisms underlying the spatial and temporal expression pattern of Cx43 remain elusive. In the current study, we have provided several lines of evidence to demonstrate MKK4 regulation of Cx43 gene expression: 1) knockdown of endogenous MKK4 expression by siMKK4 or inhibition of its kinase activity by infection of Ad-dnMKK4 caused a substantial reduction in Cx43 expression; 2) luciferase reporter assays showed blunted Cx43-promoter reporter activity in siMKK4- or Ad-dnMKK4-NRCMs after PE treatment; 3) increased MKK4 activation in NRCMs resulted in elevated Cx43 promoter-reporter activity;

MKK4 Regulates Cx43 Expression in Cardiomyocytes

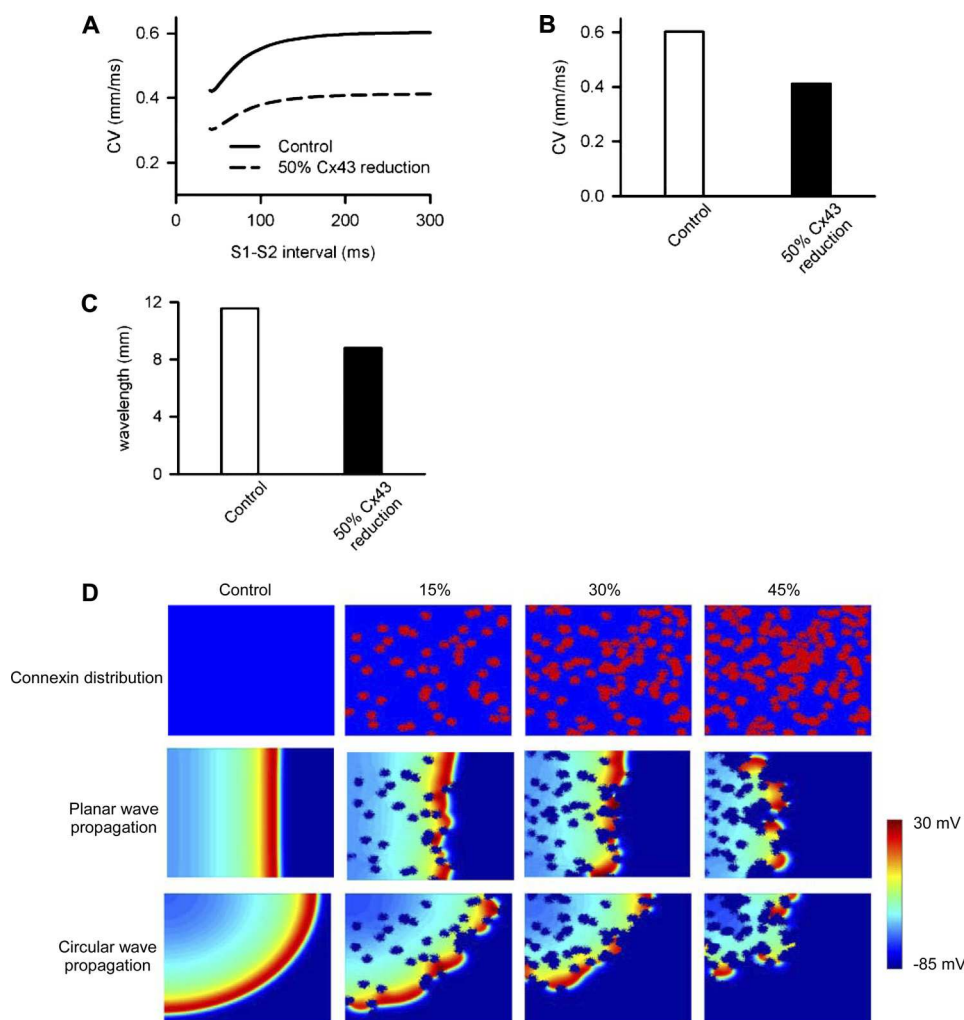


FIGURE 6. Computational simulations of the effects of Cx43 remodeling on increased propensity for arrhythmias. A, CV under control (solid line) and 50% homogeneous reduction of Cx43 (dashed line). B, conduction velocity when the S1-S2 interval is equal to 100 ms. C, the effect of reduced Cx43 coupling on wavelength of a solitary wave. D, effects heterogeneous reduction of gap junctional coupling on the propagation of ventricular excitation waves in a two-dimensional model of the ventricular sheet. The top rows show a color-coded distribution of gap junctional coupling (blue, $D = 0.011 \text{ mm}^2/\text{ms}$; red, $D = 0$), the middle and bottom rows show snapshots of planer wave conduction and circular wave conduction, respectively. Snapshots of ventricular excitation wave conduction were shown for the control conduction (first columns), a 15% reduction of the gap junctional coupling (second columns), a 30% reduction (third columns), and a 45% reduction (fourth columns).

and 4) luciferase assays using mutations in the Cx43 promoter region demonstrated that MKK4-regulated Cx43 transcription is dependent on AP-1 transcriptional activity. Consistent with these data, decreased Cx43 expression was also detected in the MKK4^{cko}-TAC heart. Of note, there was a similar reduction of Cx43 at both the mRNA and protein level. We thus believe that the MKK4/JNK/c-Jun pathway regulates Cx43 transcription via AP-1 activity in cardiomyocytes under hypertrophic stress and that decreased Cx43 protein expression is likely attributable to its reduced mRNA level.

Cx43 is a highly phosphorylated and regulated protein. It has been proposed that phosphorylation of Cx43 is related to its internalization (5); however, previous studies have also demonstrated that dephosphorylated Cx43 is associated with trafficking/endocytosis in the cytoplasm, whereas those gap junctions remaining in the intercalated disc contain phosphorylated Cx43 (27, 28). In our experimental setting, we presently cannot rule out that (de)phosphorylation of Cx43 contributes to its reduction and heterogeneous expression in MKK4^{cko}-TAC

cardiomyocytes. However, the migratory pattern of Cx43 on SDS-PAGE gel electrophoresis appeared similar in both controls and MKK4^{cko}-TAC hearts. Alterations in Cx43 phosphorylation status may not always be reflected in its mobility on polyacrylamide gels, and, therefore, additional studies employing antibodies specific for different phosphorylated isoforms of Cx43 are necessary to resolve this issue.

Roles of Junctional Proteins in MKK4^{cko}-TAC Mice—It has become apparent that molecular “cross-talk” exists between gap junctions and adherens junctions or desmosomes. For example, cardiac-specific perturbation of N-cadherin leads to the formation of an arrhythmogenic substrate by an alteration in Cx43 (29, 30). β -Catenin, in addition to scaffolding N-cadherin to actin, also contributes to transcriptional regulation of Cx43 (31). Mutations in plakoglobin are linked to a rare recessive disorder, Naxos disease (32). Interestingly, Cx43 levels are decreased remarkably in the hearts of Naxos disease patients, who present with right ventricular cardiomyopathy accompanied by a high incidence of arrhythmias and sudden cardiac

death (32). ZO-1, in fact, physically associates with Cx43 acting as an adaptor, which anchors gap junctions to the cytoskeleton (20, 33). Abolition of the association of ZO-1 and Cx43 results in a reduction in the number of gap junction plaques and an increase in mean plaque size (33). In the present study, we did not observe visible abnormalities in the expression and distribution of N-cadherin, β -catenin, and plakoglobin in the MKK4^{cko} heart. However, ZO-1 expression proved to be significantly decreased in the MKK4^{cko} hypertrophic heart. This reduction of ZO-1 expression may underlie the observed diffused expression of Cx43, part of which was detected in the cytoplasm. It is presently unclear whether MKK4 deficiency is directly responsible for the decreased ZO-1 expression or whether it is secondary to the reduction of Cx43 expression.

Loss of MKK4 Couples Hypertrophic Signals to Arrhythmogenesis—Cell-to-cell coupling and myocardial tissue architecture are thought to be major factors dictating normal impulse propagation through the heart (34). QRS duration is determined by impulse conduction velocity and cardiomyocyte size (35). One week after TAC, MKK4^{cko} mice displayed increased cardiac hypertrophy as indicated by enlarged cross-sectional area ($346.5 \pm 3.26 \mu\text{m}^2$) compared with $252.4 \pm 6.88 \mu\text{m}^2$ cross-sectional area in the MKK4^{fl/fl} cardiomyocyte (16). In the present study, ECG recordings showed prolonged QRS duration and greater QRS/QTc ratio in the MKK4^{cko}-TAC heart, whereas JT intervals did not appear significantly different between the two TAC groups. Epicardial activation mapping demonstrated delayed ventricular electrical propagation in the MKK4^{cko}-TAC heart. Together, these results indicate that the MKK4^{cko}-TAC heart had slowed ventricular conduction, which is likely attributed to patchy Cx43 reduction together with increased cardiomyocyte size. Furthermore, in the hypertrophied MKK4^{cko} heart, heterogeneity in Cx43 expression is thought to result in cardiomyocyte uncoupling, which creates the nonuniformities required for initiating breaks in a propagating wavefront. The mathematical models in this study have simulated this phenomenon. Computational simulations demonstrate that this spatially heterogeneous decrease in Cx43 accounts for slowed ventricular conduction and fragmented wave propagations, a critical factor for arrhythmogenesis. Previous studies have shown that ventricular myocardium is not homogeneous; it has electrophysiologically distinct cell types, which give rise to transmural voltage gradients and a dispersion of repolarization (36). Heterogeneity in Cx43 distribution has been correlated with increased transmural dispersion in refractoriness (37), and the hypertrophic response of enlarged myocardium mass, is believed to add additional factors to transmural dispersion of repolarization, augmenting electrical heterogeneities intrinsic to the ventricular myocardium. As such, it is plausible that heterogeneously reduced Cx43 expression together with increased hypertrophy predispose MKK4^{cko} mice to ventricular arrhythmias.

We have noticed that although a significant decrease was seen in Cx43 expression at both the mRNA and protein level in all MKK4^{cko}-TAC hearts; however, six of 13 mutant mice developed ventricular tachycardia when *in vivo* ventricular programmed pacing was introduced. The possible reasons for such individual discrepancy in occurrence of ventricular tachycardia

could be due to the heterogeneous reduction and distribution of Cx43 in MKK4^{cko}-TAC mice, or due to individual difference in the extent of hypertrophy induced by TAC hence leads to a nonuniform reduction and/or distribution of Cx43 in MKK4^{cko}-TAC mice, or due to the nature of the different response (changes in Cx43 expression) of individual mouse to TAC stress and genetic modification of MKK4.

Of note, apart from cardiomyocytes, interstitial collagen deposition is also responsible for cardiac tissue architecture. Increased interstitial fibrosis, especially reparative fibrosis, which replaces zones of dead cardiomyocytes with collagen within muscle bundles, can disrupt impulse propagation. This type of fibrotic change is expected to amplify the effect of conduction slowing and electrical uncoupling in the areas of Cx43 remodeling. Interestingly, 1 week of TAC treatment did not cause apparent apoptosis and fibrosis in MKK4^{cko} mice (16); thus, involvement by interstitial fibrosis in ventricular tachycardia occurrence in MKK4^{cko} mice can be excluded.

Conclusions—In summary, we have identified a new role for MKK4 in regulating Cx43 expression in cardiomyocytes. MKK4 is a critical regulator in the heart for maintaining Cx43 expression/distribution, which are important for preservation of normal cardiac electrical function. The recognition of the functional significance of MKK4 in preventing arrhythmogenesis, together with our previous findings that MKK4 antagonizes pathological hypertrophy, may lead to the development of better therapies for treating hypertrophy-associated ventricular arrhythmias.

REFERENCES

- Saffitz, J. E., and Kléber, A. G. (2004) *Circ. Res.* **94**, 585–591
- Gutstein, D. E., Morley, G. E., Tamaddon, H., Vaidya, D., Schneider, M. D., Chen, J., Chien, K. R., Stuhlmann, H., and Fishman, G. I. (2001) *Circ. Res.* **88**, 333–339
- Gutstein, D. E., Danik, S. B., Sereysky, J. B., Morley, G. E., and Fishman, G. I. (2003) *Am. J. Physiol. Heart. Circ. Physiol.* **285**, H1091–H1096
- van Rijen, H. V., Eckardt, D., Degen, J., Theis, M., Ott, T., Willecke, K., Jongsma, H. J., Opthof, T., and de Bakker, J. M. (2004) *Circulation* **109**, 1048–1055
- Laird, D. W. (2005) *Biochimica. et Biophysica. Acta* **1711**, 172–182
- Shyu, K. G., Wang, B. W., Yang, Y. H., Tsai, S. C., Lin, S., and Lee, C. C. (2004) *Cardiovasc. Res.* **63**, 98–108
- Petrich, B. G., Eloff, B. C., Lerner, D. L., Kovacs, A., Saffitz, J. E., Rosenbaum, D. S., and Wang, Y. (2004) *J. Biol. Chem.* **279**, 15330–15338
- Petrich, B. G., Gong, X., Lerner, D. L., Wang, X., Brown, J. H., Saffitz, J. E., and Wang, Y. (2002) *Circ. Res.* **91**, 640–647
- Cameron, S. J., Malik, S., Akaike, M., Lerner-Marmarosh, N., Yan, C., Lee, J. D., Abe, J., and Yang, J. (2003) *J. Biol. Chem.* **278**, 18682–18688
- Ogawa, T., Hayashi, T., Kyoizumi, S., Kusunoki, Y., Nakachi, K., MacPhee, D. G., Trosko, J. E., Kataoka, K., and Yorioka, N. (2004) *J. Cell Sci.* **117**, 2087–2096
- Salameh, A., Schneider, P., Mühlberg, K., Hagendorff, A., Dhein, S., and Pfeiffer, D. (2004) *Eur. J. Pharmacol.* **503**, 9–16
- Wang, X., Destrumont, A., and Tournier, C. (2007) *Biochim. Biophys. Acta* **1773**, 1349–1357
- Brancho, D., Tanaka, N., Jaeschke, A., Ventura, J. J., Kelkar, N., Tanaka, Y., Kyuuma, M., Takeshita, T., Flavell, R. A., and Davis, R. J. (2003) *Genes Dev.* **17**, 1969–1978
- Tournier, C., Whitmarsh, A. J., Cavanagh, J., Barrett, T., and Davis, R. J. (1997) *Proc. Natl. Acad. Sci. U.S.A.* **94**, 7337–7342
- Wang, X., Nadarajah, B., Robinson, A. C., McColl, B. W., Jin, J. W., Dajas-Bailador, F., Boot-Handford, R. P., and Tournier, C. (2007) *Mol. Cell Biol.* **27**, 7935–7946

MKK4 Regulates Cx43 Expression in Cardiomyocytes

16. Liu, W., Zi, M., Jin, J., Prehar, S., Oceandy, D., Kimura, T. E., Lei, M., Neyses, L., Weston, A. H., Cartwright, E. J., and Wang, X. (2009) *Circ. Res.* **104**, 905–914
17. Peters, N. S., Green, C. R., Poole-Wilson, P. A., and Severs, N. J. (1993) *Circulation* **88**, 864–875
18. Dupont, E., Matsushita, T., Kaba, R. A., Vozzi, C., Coppen, S. R., Khan, N., Kaprielian, R., Yacoub, M. H., and Severs, N. J. (2001) *J. Mol. Cell Cardiol.* **33**, 359–371
19. Saffitz, J. E. (2005) *Ann. N.Y. Acad. Sci.* **1047**, 336–344
20. Toyofuku, T., Yabuki, M., Otsu, K., Kuzuya, T., Hori, M., and Tada, M. (1998) *J. Biol. Chem.* **273**, 12725–12731
21. Severs, N. J., Bruce, A. F., Dupont, E., and Rothery, S. (2008) *Cardiovasc. Res.* **80**, 9–19
22. Danik, S. B., Liu, F., Zhang, J., Suk, H. J., Morley, G. E., Fishman, G. I., and Gutstein, D. E. (2004) *Circ. Res.* **95**, 1035–1041
23. Gutstein, D. E., Morley, G. E., Vaidya, D., Liu, F., Chen, F. L., Stuhlmann, H., and Fishman, G. I. (2001) *Circulation* **104**, 1194–1199
24. Teunissen, B. E., Jansen, A. T., van Amersfoort, S. C., O'Brien, T. X., Jongsma, H. J., and Bierhuizen, M. F. (2003) *Gene* **322**, 123–136
25. Mitchell, J. A., and Lye, S. J. (2005) *Endocrinology* **146**, 2048–2054
26. Boogerd, K. J., Wong, L. Y., Christoffels, V. M., Klarenbeek, M., Ruijter, J. M., Moorman, A. F., and Barnett, P. (2008) *Cardiovasc. Res.* **78**, 485–493
27. Matsushita, T., Oyamada, M., Fujimoto, K., Yasuda, Y., Masuda, S., Wada, Y., Oka, T., and Takamatsu, T. (1999) *Circ. Res.* **85**, 1046–1055
28. Lampe, P. D., Cooper, C. D., King, T. J., and Burt, J. M. (2006) *J. Cell Sci.* **119**, 3435–3442
29. Kostetskii, I., Li, J., Xiong, Y., Zhou, R., Ferrari, V. A., Patel, V. V., Molkentin, J. D., and Radice, G. L. (2005) *Circ. Res.* **96**, 346–354
30. Li, J., Patel, V. V., Kostetskii, I., Xiong, Y., Chu, A. F., Jacobson, J. T., Yu, C., Morley, G. E., Molkentin, J. D., and Radice, G. L. (2005) *Circ. Res.* **97**, 474–481
31. Ai, Z., Fischer, A., Spray, D. C., Brown, A. M., and Fishman, G. I. (2000) *J. Clin. Invest.* **105**, 161–171
32. McKoy, G., Protonotarios, N., Crosby, A., Tsatsopoulou, A., Anastasakis, A., Coonar, A., Norman, M., Baboonian, C., Jeffery, S., and McKenna, W. J. (2000) *Lancet* **355**, 2119–2124
33. Maass, K., Shibayama, J., Chase, S. E., Willecke, K., and Delmar, M. (2007) *Circ. Res.* **101**, 1283–1291
34. Kléber, A. G., and Rudy, Y. (2004) *Physiol. Rev.* **84**, 431–488
35. Wiegerinck, R. F., Verkerk, A. O., Belterman, C. N., van Veen, T. A., Baartscheer, A., Opthof, T., Wilders, R., de Bakker, J. M., and Coronel, R. (2006) *Circulation* **113**, 806–813
36. Antzelevitch, C. (2001) *Cardiovasc. Res.* **50**, 426–431
37. Wiegerinck, R. F., van Veen, T. A., Belterman, C. N., Schumacher, C. A., Noorman, M., de Bakker, J. M., and Coronel, R. (2008) *Heart Rhythm.* **5**, 1178–1185